



**University of
Sheffield**

**Fabrication and Optical Characterization of Laser-Patterned III-V
Quantum Dot Arrays**

Yaoxun Wang

A thesis submitted in partial fulfilment of the requirements for the degree
of
Doctor of Philosophy

The University of Sheffield
Faculty of Engineering
School of Electrical and Electronic Engineering

March 2025

Abstract

This thesis investigates the fabrication and optical behavior of ordered III-V quantum dot (QD) arrays using a novel in-situ direct laser interference patterning (DLIP) technique integrated with molecular beam epitaxy (MBE). By merging the precision of MBE with the spatial control of DLIP, the research demonstrates a scalable, contamination-free approach to deterministic quantum dot array formation—a key requirement for quantum information processing applications.

The study explores two QD systems: InGaAs/AlGaAs/GaAs QDs fabricated via droplet epitaxy and InAs/GaAs QDs grown through both Stranski–Krastanov and droplet epitaxy modes. An automated photoluminescence (PL) mapping system was developed to conduct spatially resolved optical characterization across millimetre-scale regions with high throughput.

Key achievements of the study include the successful integration of a four-beam DLIP system within an MBE chamber, controlled nucleation of ordered QD arrays with tunable morphology via laser energy and material coverage, and the attainment of narrow photoluminescence linewidths down to approximately 17 meV, signifying high optical quality. A quantitative correlation was established between DLIP parameters and resulting QD properties such as size, density, and emission spectra. Furthermore, the work demonstrates highly ordered and optically active QDs without the need for complex ex-situ lithographic steps.

These findings advance the field of site-controlled quantum dot growth by offering a repeatable and contamination-free fabrication method. The developed approach holds significant promise for photonic quantum computing circuits, where spatial precision and emission purity are critical. Future outlooks include integrating these arrays in single-photon sources and exploring their applications in quantum plasmonic and telecom technologies. This work paves the way toward scalable quantum photonic devices through hybrid epitaxial-lithographic strategies

Acknowledgements

Pursuing a PhD in the School of Electronic and Electrical Engineering at the University of Sheffield over the past four years has been an unforgettable experience. Despite the challenges brought by the pandemic, I've made lasting memories and am deeply grateful for the opportunity to meet and work with so many outstanding people who supported me both academically and personally.

First and foremost, I want to express my sincere gratitude to my supervisor, Prof. Mark Hopkinson. His guidance and support have been essential in completing this work. Mark has not only provided expert supervision throughout my research but has also supported me during difficult moments in both my academic journey and personal life. I am especially thankful for the insightful discussions and ideas he shared with me. His passion for research and expertise in MBE, epitaxy of III-V semiconductor nanostructures, photoluminescence spectroscopy, and lab techniques have been incredibly valuable to my growth.

I am also thankful to my colleagues, Dr. Im Sik Han and Dr. Yunran Wang. Dr. Han's dedication and enthusiasm were vital—he grew all the samples used in this research. Dr. Wang guided me through understanding the DLIP technique during MBE growth. Their teamwork and support made this thesis possible.

Lastly, I would like to dedicate this thesis to my grandfather, Shizuo Wang, in his memory. Words cannot fully express my gratitude to my family for not seeing each other for four years due to the pandemic. My beloved parents, fiancée, and along with my dear friends Dr Zhiheng Lin, Dr Yuan Rui and Dr Lei Wei have shown me unwavering support, care, and love throughout these years.

List of contents

Abstract	2
Acknowledgements	3
List of contents	4
List of Tables	7
List of Figures	8
Declaration	13
List of Publications	14
1. INTRODUCTION	15
1.1. THE SEMICONDUCTOR QUANTUM CONFINEMENT SYSTEM	18
1.1.1. PRINCIPLE OF QUANTUM CONFINEMENT SYSTEM	18
1.1.2. ENERGY LEVELS AND DENSITY OF STATES IN DIFFERENT SEMICONDUCTOR NANOSTRUCTURES	20
1.1.3. THEORETICAL MODEL OF QUANTUM DOT ARRAYS	23
1.2. THE DEVELOPMENT III-V COMPOUND SEMICONDUCTOR MATERIAL SYSTEM	28
1.2.1. III-V COMPOUND SEMICONDUCTORS FOR QUANTUM STRUCTURES ...	28
1.2.2. GROWTH AND INTEGRATION CHALLENGES	30
1.3. HISTORICAL CONTEXT OF III-V SEMICONDUCTOR NANOSTRUCTURE ARRAY FABRICATION	32
1.3.1. MULTILAYER VERTICAL STACKING	33
1.3.2. SELF-ORGANIZED ANISOTROPIC STRAIN ENGINEERING	34
1.3.3. SITE-CONTROLLED GROWTH	35
1.3.4. DIRECT LASER INTERFERENCE PATTERNING (DLIP)	36
1.4. PROJECT MOTIVATION AND OBJECTIVES	38
1.5. THESIS OUTLINES	40
2. EPITAXY OF III-V SEMICONDUCTOR NANOSTRUCTURE ARRAY VIA MOLECULAR BEAM EPITAXY	42
2.1. THE SEMICONDUCTOR QUANTUM CONFINEMENT SYSTEM	42
2.1.1. SURFACE KINETIC PROCESS	44
2.1.2. EPITAXIAL GROWTH TOWARDS HETEROGENEOUS STRUCTURE	47
2.2. DEPOSITION METHOD OF III-V COMPOUND SEMICONDUCTOR NANOSTRUCTURE ARRAY USING MBE	50

2.2.1.	STRANSKI-KRASTANOV MODE	51
2.2.2.	DROPLET EPITAXY	55
2.2.3.	DIRECT LASER INTERFERENCE PATTERNING	58
2.3.	SUMMARY	66
3.	EXPERIMENTAL AND CHARACTERISTICS METHODS	68
3.1.	Molecular Beam Epitaxy System	68
3.1.1.	FUNDAMENTALS OF MBE SYSTEMS	69
3.1.2.	THE MBE SYSTEM WITH DIRECT LASER INTERFERENCE PATTERNING SET-UP	72
3.2.	Atomic Force Spectroscopy	78
3.3.	Photoluminescence Spectroscopy	80
3.3.1.	PRINCIPLE OF PHOTOLUMINESCENCE SPECTROSCOPY	80
3.3.2.	Mirco-Photoluminescence Spectroscopy (μ -PL)	84
3.3.3.	Time-Resolved PL	89
3.4.	SUMMARY	90
4.	AUTO-MAPPER SYSTEM FOR AUTOMATED SPATIAL PHOTOLUMINESCENCE SPECTROSCOPY	92
4.1.	OBJECTIVES AND AIM OF THE AUTOMAPPER SYSTEM	92
4.2.	DEVELOPMENT OF THE AUTOMAPPER SYSTEM	94
4.2.1.	TECHNICAL ROUTE	94
4.2.2.	INITIALISATION	96
4.2.3.	DATA ACQUISITION	98
4.2.4.	POST DATA PROCESSING	103
4.3.	SYSTEM ACHIEVEMENTS	104
4.4.	SUMMARY	105
5.	EPITAXY AND CHARACTERIZATION OF ORDERED InGaAs/AlGaAs/GaAs QDs ARRAY VIA DROPLET EPITAXY	106
5.1.	INTRODUCTION	106
5.2.	EPITAXY OF PATTERNED In _x Ga _{1-x} As QUANTUM DOT ARRAYS	110
5.2.1.	PRINCIPLE OF THE EPITAXIAL PROCESS	110
5.2.2.	SAMPLE STRUCTURE	112
5.2.3.	SAMPLE GROWTH	113

5.3.	RESULT AND DISCUSSION.....	114
5.3.1.	INFLUENCE FACTORS OF THE GROWTH PROCESS.....	115
5.3.2.	OPTICAL PROPERTIES OF PATTERNED INGAAS QUANTUM DOTS.....	126
5.4.	SUMMARY.....	135
6.	EPITAXY AND CHARACTERIZATION OF ORDERED InAs/GaAs QDS ARRAY VIA DLIP-MBE.....	137
6.1.	INTRODUCTION.....	137
6.2.	GROWTH OF ORDERED InAs QUANTUM DOT ARRAYS.....	139
6.2.1.	EPITAXY OF ORDERED InAs/GaAs QUANTUM DOT ARRAYS VIA SK MECHANISM.....	139
6.2.2.	EPITAXY OF ORDERED InAs/GaAs QUANTUM DOT ARRAYS VIA DROPLET EPITAXY.....	140
6.3.	RESULT AND DISCUSSION.....	142
6.3.1.	CHARACTERISATION OF ORDERED InAs/GaAs QUANTUM DOT ARRAYS VIA SK MECHANISM.....	142
6.3.2.	CHARACTERISATION OF ORDERED INAS/GAAS QUANTUM DOT ARRAYS VIA DROPLET EPITAXY.....	153
6.3.3.	DISCUSSION.....	162
6.4.	SUMMARY.....	165
7.	CONCLUSION AND FUTURE WORK.....	169
7.1.	CONCLUSION.....	169
7.2.	OUTLOOK.....	171
7.2.1.	SURFACE PLASMONIC SOLAR CELL.....	171
7.2.2.	SINGLE PHOTON EMITTER TOWARDS QUANTUM TELECOMMUNICATION.....	173
7.2.3.	OTHER APPLICATIONS.....	175
	BIBLIOGRAPHY.....	177

List of Tables

Table 1.1 Comparison of current techniques towards self-assemble semiconductor nanostructure array.....	37
Table 4.1 Overall mapping flowchart of Python-based system	101
Table 5.1 Quantitative comparison of QD morphological parameters as a function of laser energy.....	118
Table 5.2 Quantitative morphological parameters as a function of InGaAs coverage.....	120

List of Figures

Figure 1.1 Timeline of advances in quantum photonic chips for quantum computing and communication [18].	17
Figure 1.2 The illustration of dimension quantum confinement system and their DOS density.	22
Figure 1.3 Schematic illustration diagram of miniband formation in quantum dot arrays.	25
Figure 1.4 Calculated Bandgap energy Vs lattice constant of III-V compound materials and IV group material via SolCore [73].	31
Figure 1.5 (a) TEM image of InAs/GaAs quantum dots with multiple vertical stacking technique [88]. (b) AFM image of InAs/GaAs quantum dots with self-organized anisotropic strain engineering [89].	34
Figure 1.6 (a) AFM image of InAs/GaAs quantum dots with site-controlled growth on pre-patterned substrates [107]. (b) AFM image of InAs/GaAs quantum dots by Direct laser interference patterning [108].	36
Figure 2.1 Schematic representation of the three fundamental growth modes in epitaxial systems.	45
Figure 2.2 Schematic diagram of (a) epitaxial growth of lattice match structure, (b) epitaxial growth of minor lattice mismatch, (c) non- epitaxial growth of major lattice mismatch and (d) epitaxial growth despite of large lattice mismatch with strong strain relaxation.	48
Figure 2.3 Schematic process diagram of different growth mode (1) Frank-Van der Merwe (F-M) mode. (2) Volmer-Weber mode. (3) Stanski-Krastanov mode	51
Figure 2.4 Schematic diagram of S-K mode conditions with growth time and strain energy.	52

Figure 2.5 $2 \times 2 \mu\text{m}^2$ AFM images showing evolution of the surface morphology of GaAs quantum dots with increasing GaAs deposition amount: (a) 1 ML. (b) 2.5 ML. and (c) 4.5 ML [146].	54
Figure 2.6 Schematic process diagram for DE and SK via MBE a) Droplet epitaxy b) SK mode	56
Figure 2.7 Simulated 500nm waist radius Gaussian beam intensity distribution profile of (a) 2-D view. (b) 3-D view.	60
Figure 2.8 Illumination of four-beam interference configuration at an incident angle of θ and equivalent azimuth angle with an example of simulated intensity distribution map shown on the right.	64
Figure 2.9 Simulated interference laser intensity distribution of 58° incident angle and 0° polarization angle with (a) 1 beam. (b) 2 beams. (c) 3 beams. (d) 4 beams. (e) 5 beams. (f) 6 beams. (g) 7 beams. (h) 8 beams.	65
Figure 2.10 Simulation of four-beam interference intensity patterns using various combinations of incidence and polarization angles.	66
Figure 3.1 Illustration of a typical solid-source MBE growth chamber.	70
Figure 3.2 Photograph of the modified MBE system which provided by Dr. Eberl MBE-Komponenten [®] GmbH (Germany).	72
Figure 3.3 (a–c) Photos showing parts of the DLIP setup surrounding the MBE chamber. (d) Camera image of four laser beams focused at the center of an InGaN wafer.	75
Figure 3.4 Photographs of (a) the Nd: YAG laser with a seeder. (b) The attenuator.	76
Figure 3.5 General layout of the four-beam DLIP configuration for MBE growth. BS1- BS3: 50:50 beam splitters, M1-M7: high reflective UV mirrors and S for the substrate holder.	77

Figure 3.6 (a) Diagrammatic illustration of the principle of AFM. (b) Photograph of an AFM instrument. 80

Figure 3.7 Schematic band diagram of interband transitions in bulk semiconductors. (a) Band edge recombination in a direct bandgap semiconductor. (b) Indirect, phonon assisted recombination in an indirect bandgap semiconductor. 81

Figure 3.8 Schematic band diagram via different size InGaAs/GaAs QDs..... 82

Figure 3.9 Schematic diagram of a typical μ -PL setup the excitation path (green), collection path (red), and cryogenic sample stage with nanopositioning capabilities. Essential components include the excitation laser, beam conditioning optics, high-NA objective, spectrometer, and detector array..... 85

Figure 3.10 Photo of the key components of the μ -PL system used in this thesis. 88

Figure 4.1 Flow chart of Automapper System. 95

Figure 4.2 Example of scanning route of the preset grid. 97

Figure 4.3 The running LabVIEW-based system. 102

Figure 4.4 Example of automapping results of an InAs QDs sample of a 1X1 mm region by (a) wavelength distribution. (b) Intensity distribution. 104

Figure 5.1 Cross-section transmission electron microscopy photos: (a) 100 nm scale. (b) 20 nm scale for the $\text{In}_{0.6}\text{Ga}_{0.4}\text{As}/\text{GaAs}$ QDIP[216]. 109

Figure 5.2 Schematic diagram of (a) Demonstration of Four-beams laser interference patterning with same incident angle. (b) Formation process of InGaAs DE quantum dot array..... 112

Figure 5.3 Comprehensive schematic cross-sectional structure diagram of the InGaAs/AlGaAs/GaAs quantum dots array sample. 113

Figure 5.4 Effects of laser energy on quantum dot morphology. (a) AFM micrographs of InGaAs QD arrays fabricated using laser energy of 55 mJ/cm². (b) QD arrays fabricated using 40 mJ/cm². (c)-(d) Cross-sectional height profiles along the direction. (e) Statistical distribution of dot height and diameter for both energy regimes.117

Figure 5.5 Evolution of quantum dot morphology with increasing In/Ga coverage for In_{0.15}Ga_{0.85}As. Three-dimensional AFM images showing QD formation at coverage values of: (a) 1.78 ML. (b) 2.0 ML. (c) 2.07 ML. (d) 2.17 ML. and (e) 2.27 ML. Lower panels (f-j) show corresponding cross-sectional profiles along the [001] direction...119

Figure 5.6 AFM image of In_{0.26}Ga_{0.73}As quantum dot array with In/Ga coverage of (a) 2ML. (b) 2.15ML. (c) 2.5ML. (d)-(f) presents the 3-D view of the sample (a)-(c). (g)-(i) illustrate the x-y direction profile of sample (a)-(c).121

Figure 5.7 AFM image of Al_{0.3}Ga_{0.7}As layer grown under (a) 200°C. (b) 200°C with additional 30mins annealing at 750°C. (c) 50°C with additional 30mins annealing at 750°C. (d) 600°C with 50 periods superlattice growth and 30mins annealing at 750°C.124

Figure 5.8 (a)- (c) Result of an In_{0.3}Ga_{0.7}As quantum dot sample with 1.78 ML coverage (a) Temperature dependent spectroscopy under 5uW excitation power. (b) Excitation power dependent spectroscopy at 10K. (c) Normalized PL intensity versus inverse temperature. (d) Normalise PL intensity depending upon the excitation power density at 10 K of different InGaAs coverage with same In/Ga ratio. The linear fitting indicated the slope of different InGaAs127

Figure 5.9 The PL spectrum of patterned In_{0.3}Ga_{0.7}As quantum dot at 10K under 2 μW excitation power130

Figure 5.10 The PL spectrum of patterned In_{0.15}Ga_{0.85}As quantum dot at 10K under 2 μW excitation power 错误!未定义书签。

Figure 6.1 Schematic growth structure of InAs/GaAs DE QDs.139

Figure 6.2 Schematic growth structure of InAs/GaAs DE QDs.....	141
Figure 6.3 Evolution of SK quantum dot morphology with increasing InAs coverage. Three-dimensional AFM images showing QD formation at coverage values of: (a) 2.5 ML. (b) 1.6 ML. (c) 1.4 ML. (d) 1.3 ML. and (e) 1.2 ML.	144
Figure 6.4 AFM images of capping layer with (a) 200nm GaAs capping layer under 515°C. (b) 200nm GaAs capping layer under 530°C. (c) 200nm GaAs capping layer under 550°C. (d) 200nm GaAs capping layer under 560°C.	147
Figure 6.5 PL spectroscopy of a 1.8 ML coverage InAs quantum dots inside the pattern region (a) Excitation power dependent spectroscopy at 10K. (b) Normalise PL intensity depending upon the excitation power density at 10 K. The linear fitting indicated the slope of different InGaAs is around 1.01. (c) The PL spectrum of InAs quantum dot at 10K under 1 μ W excitation power with Gaussian peak (FWHM=24meV)	149
Figure 6.6 AFM image of (a) Indium droplet without crystallization. (b) Indium droplet with crystallization to form InAs DE QDs. (c) Indium droplet without crystallization with 0.6 III-V ratio at 200°C. (d) Indium droplet with crystallization to form InAs DE QDs under 0.8 III-V ratio at 200°C.....	155
Figure 6.7 AFM image of InAs droplet epitaxy quantum dots sample of (a) 20 nm GaAs layer at 400°C + 10mins annealing at 400°C + 80 nm GaAs layer at 600°C. (b) 20 nm GaAs layer at 400°C + 10mins annealing at 400°C + 80 nm GaAs layer at 600°C + 30 mins annealing at 750°C. (c) 20 nm GaAs layer at 200°C + 80 nm GaAs layer at 600°C + 30 mins annealing at 750°C.	158
Figure 6.8 STEM image of the InAs Droplet epitaxy quantum dots sample with Annular Dark-Field view image, EDS view of Arsenic and Indium mass distribution image,	160

Declaration

Please ensure that the following is included in your declaration:

I, Yaoxun Wang, confirm that the Thesis is my own work. I am aware of the University's Guidance on the Use of Unfair Means (www.sheffield.ac.uk/ssid/unfair-means). This work has not previously been presented for an award at this, or any other, university.

List of Publications

Journals:

1. Lin, Z., Wang, Y.R., Wang, Y. and Hopkinson, M., 2025. Design and fabrication of photonic crystal structures by single pulse laser interference lithography. *Optics & Laser Technology*, 181, p.111951. (Data acquisition. Graph plotting, FDTD simulation, Writing)
2. Lin, Z., Wang, Y., Wang, Y.R., Han, I.S. and Hopkinson, M., 2024. Photonic crystal enhanced light emitting diodes fabricated by single pulse laser interference lithography. *Journal of Applied Physics*, 136(12). (Data acquisition. Graph plotting, FDTD simulation, Writing)
3. Lin, Z., Wang, Y., Wang, Y.R., Han, I.S. and Hopkinson, M., 2024. Fabrication of Photonic Crystal Structures on GaAs by Single Pulse Laser Interference Lithography. *Journal of Laser Micro Nanoengineering*, 19(2), pp.135-139. (Data acquisition. Graph plotting, Fabrication, Writing)

Poster And oral presentation:

1. Hopkinson, M. Wang, Y.R, Han I.S, Wang Y.X, and Lin, Z.H. "In-situ pulsed laser interference for the site-controlled growth of InGaAs quantum dots". *MBE 2023*.
2. Im Sik Han, Yun-ran Wang, Yaoxun Wang, Ziheng Lin and Mark Hopkinson. "Fabrication of droplet epitaxial III-V nanostructure arrays using in situ direct laser interference patterning". *UK Semiconductor 2023*.
3. Yaoxun Wang, Ziheng Lin, Yunran Wang, Im Sik Han and Mark Hopkinson. "Photoluminescence investigation of laser patterned InGaAs DE quantum dots arrays". *UK Semiconductor 2023*.
4. Ziheng Lin, Yunran Wang, Im Sik Han, Yaoxun Wang, and Mark Hopkinson. "Fabrication of GaAs antireflective nanostructure by single pulse laser interference lithography". *UK Semiconductor 2023*.

1. INTRODUCTION

The approaching limitations of Moore's Law have prompted the exploration of novel technologies to meet the exponentially growing demands of data processing. Among these, quantum computing emerged as a promising frontier following DiVincenzo's establishment of hardware criteria and the fundamental principles of quantum computing in 2000 [1]. The field has since gained attention for its potential to outperform classical computing in specific applications due to the unique properties of qubits, which enable vastly superior computational rates in certain tasks [2]. However, early quantum computing systems were reliant on electrons as information carriers, necessitating superconducting materials and highly complex circuits, which posed significant challenges to scalability and practical implementation [3]. A pivotal shift occurred with the resurgence of photonic chips, following the introduction of the linear optical quantum computing protocol (commonly referred to as the KLM protocol) by E. Knill and colleagues in 2001 [4]. Photons, as information carriers, offer distinct advantages in quantum information processing (QIP) [5], including higher fidelity [6], lower cost, and easier qubit formation compared to solid-state and superconducting circuits [7]. Optical QIP systems require high-quality single-photon sources and detectors, both of which have seen benchmark demonstrations in single-qubit switches [8, 9]. However, the implementation of multi-qubit gates remains constrained by the exponential increase in optical component requirements. A breakthrough came in 2017 when Justin B. Spring and collaborators developed a chip-based array of near-identical, pure, heralded single-photon sources using silicon-based nanostructures [10]. This innovation integrated three independent single-photon sources into a single chip, enabling simultaneous generation of unique photons triggered by laser excitation. This

approach simplified photonic logic circuits and advanced their feasibility in qubit-based computations. The use of highly organized III-V semiconductor nanostructure arrays, such as site-controlled quantum dots (QDs), quantum rings (QRs), or nanowires (NWs), holds significant potential for improving photonic QIP technology. These structures offer advantages such as tunable emission wavelengths [11], wider triggering ranges [12], and superior thermal stability [13]. Additionally, III-V materials exhibit better efficiency in single-photon emission for QIP applications due to their favorable band structures. Their structural integrity and versatility, which allow for defect-free assembly on various substrates, make III-V materials an excellent choice for highly organized photonic layouts [14].

Molecular beam epitaxy (MBE) is a key technique for growing III-V nanostructures, enabling precise size control and deposition ratios at the nanoscale [15]. This method enhances efficiency and controllability, positioning nanostructures as foundational components for integrated photonic logic units [16]. These structures, when optimized as single-photon sources with photoluminescence (PL) spectroscopy, have the potential to drive on-chip photonic circuitry [17]. For further advancement (**Figure 1.1** shows), the performance of nanostructure arrays as sources of entangled photon pairs must be improved by achieving controlled orientation and size stabilization of QDs. Additionally, reducing PL linewidth through precise scaling and minimizing QD density per unit area is crucial.

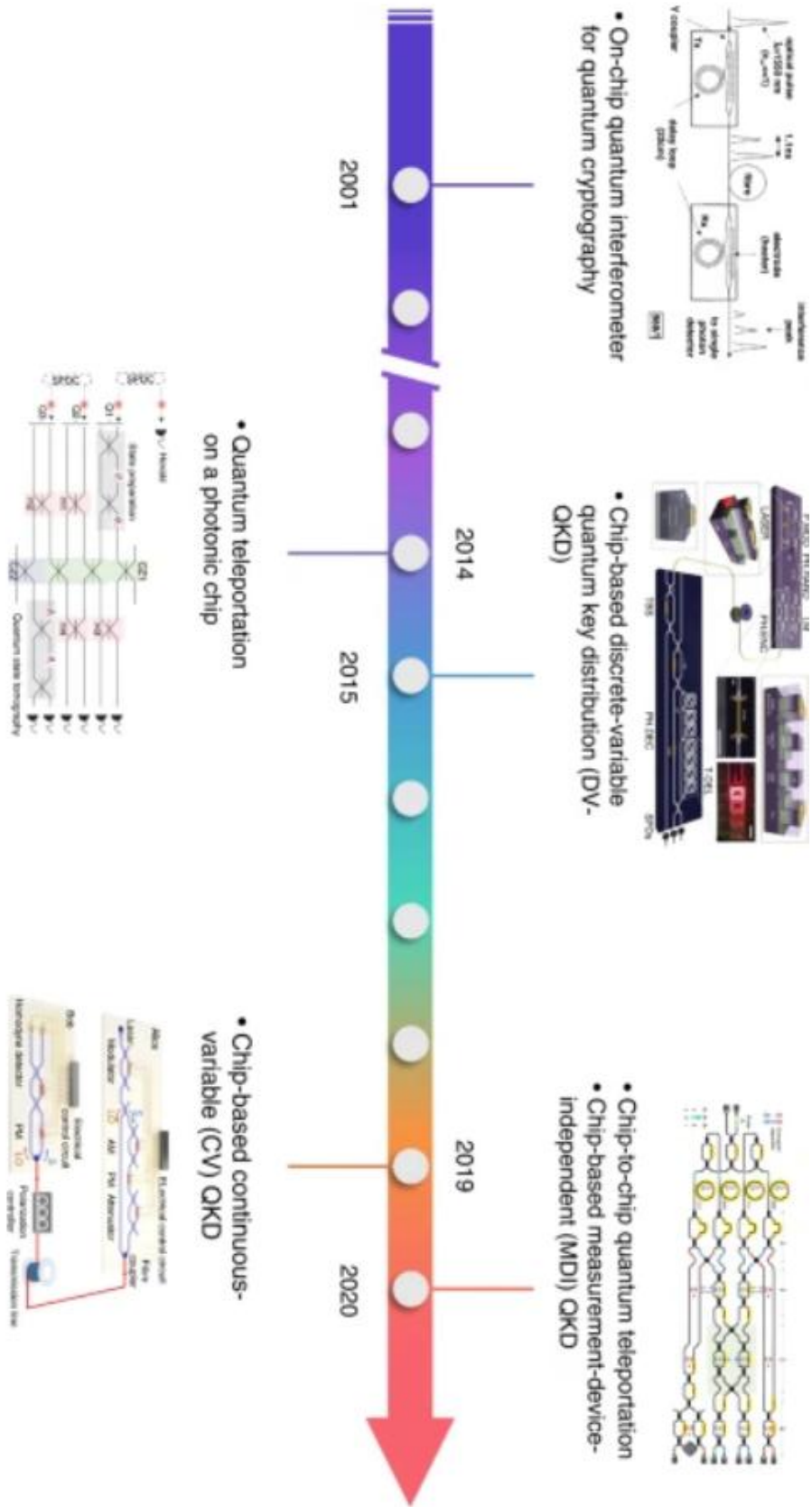


Figure 1.1 Timeline of advances in quantum photonic chips for quantum computing and communication [18].

1.1. THE SEMICONDUCTOR QUANTUM CONFINEMENT SYSTEM

The continuous development of semiconductor technologies has led to significant advancements in modern electronics and optoelectronics. Among these advancements, quantum confinement has become a foundational principle that drives progress in semiconductor nanotechnology [19]. This chapter explores the principles, implications, and applications of quantum confinement in semiconductor nanostructures, emphasizing its significance in the context of III-V compound semiconductor materials.

1.1.1. PRINCIPLE OF QUANTUM CONFINEMENT SYSTEM

Quantum confinement refers to spatial restriction of free electrons motion when the size of a semiconductor material is reduced to the nanoscale, which is comparable or smaller than the de Broglie wavelength of the charge carriers (electrons and holes to one or more dimensions [19]. This effect gives rise to discrete energy levels and unique electronic and optical properties, which are markedly different from those of their bulk counterparts. Specifically, when charge carriers are confined in one or more spatial dimensions at the nanoscale (typically 1-100 nm), the continuous energy bands characteristic of bulk semiconductors transform into discrete energy levels, significantly modifying the material's density of states (DOS) and consequently its optoelectronic properties [20, 21]. Thus, the matter wave theory could be applied to explain the compound semiconductors nanostructure with quantum mechanics theory. In such cases, the continuous energy bands observed in bulk materials are replaced by discrete energy levels owing to spatial restrictions. This effect is most prominent in materials structured as quantum wells (QW), quantum wires (QW), and quantum dots (QDs).

In ideal infinite well model, the electron momentum in the confinement system follows equation below:

$$V(\vec{r}) = \begin{cases} 0, & |x| < \frac{a}{2}, |y| < \frac{b}{2}, |z| < \frac{c}{2}, \\ \infty, & \text{Otherwise} \end{cases} \quad (1-1)$$

here, $V(\vec{r})$ is the potential energy function; a, b , and c represent the spatial boundaries of the confinement along three dimensions to x-y-z axis responsively. Within this framework, when a semiconductor nanostructure forms, it adopts a crystalline structure. The quantum state of an electron in such a confinement system can be described using the Schrödinger equation:

$$\left[-\frac{\hbar^2}{2m_e} \nabla^2 + V(\vec{r}) \right] \Psi(\vec{r}) = E\Psi(\vec{r}) \quad (1-2)$$

where:

\hbar is Planck's reduced constant ($h/2\pi$),

m_e is the effective mass of the electron in semiconductor material

∇^2 is the Laplacian operator

$\Psi(\vec{r})$ is the wavefunction.

E is the energy eigenvalue corresponding to the allowed energy states

This yields discrete energy values that depend inversely on the square of the confinement dimension [20]. The confinement energy can be mathematically expressed as:

$$E_{conf} \propto \frac{\hbar^2 \pi^2 n^2}{2m_e L^2} \quad (1-3)$$

where n is the quantum number and L is the confinement length [21]. This fundamental relationship illustrates the inverse square dependence of confinement energy on size, underpinning the size-tunable properties of quantum confined systems. The dimensionality of confinement profoundly influences both the energy level structure and density of states in semiconductor nanostructures. Depending on how

many dimensions exhibit quantum confinement, nanostructures are classified as quantum wells (QWs, 1D confinement), quantum wires (QWRs, 2D confinement), or quantum dots (QDs, 3D confinement) [22].

1.1.2. ENERGY LEVELS AND DENSITY OF STATES IN DIFFERENT SEMICONDUCTOR NANOSTRUCTURES

The dimensionality of confinement profoundly influences both the energy level structure and density of states in semiconductor nanostructures. Depending on how many dimensions exhibit quantum confinement, nanostructures are classified as quantum wells (QWs, 1D confinement), quantum wires (QWRs, 2D confinement), or quantum dots (QDs, 3D confinement) [23]. For bulk materials with no confinement, the energy-momentum relation derived from Schrödinger equation is:

$$E(k) = \frac{\hbar^2 k^2}{2m_e} \quad (1-4)$$

In 3-D, the number of states in k electrons are free to move in all three dimensions. The DOS varies with the square root of energy which presents the energy level distribution as a function of continuous curve of $E^{\frac{1}{2}}$

$$\rho_{3D}(E) = \frac{1}{2\pi^2} \left(\frac{2m_e}{\hbar^2} \right)^{\frac{3}{2}} E^{\frac{1}{2}} \quad (1-5)$$

Quantum Wells: In quantum wells, confinement occurs in a single dimension (typically along the growth direction). A thin layer of semiconductor material, is sandwiched between two barriers made of materials with a larger bandgap. As a result, charge carriers experience confinement only in the direction perpendicular to the layer plane. The resulting energy spectrum consists of discrete subbands for the confined dimension combined with continuous energy within each subband due to free movement in the plane. For a quantum well with infinite potential barriers and thickness L_z , the energy levels are given by:

$$E_{n_z} = \frac{\hbar^2 \pi^2 n_z^2}{2m_e L_z^2} \quad (1-6)$$

where n_z is the quantum number for the confined direction. The total energy of an electron includes both this quantized component and the continuous in-plane kinetic energy:

$$E_{Total} = E_{n_z} + \frac{\hbar^2 (k_x^2 + k_y^2)}{2m_e} \quad (1-7)$$

The corresponding density of states for a quantum well exhibits a step-like function:

$$\rho_{2D}(E) = \frac{m_e}{\pi \hbar^2} \sum_{n_z} \theta(E - E_{n_z}) \quad (1-8)$$

where θ is the Heaviside step function [24]. This step-like DOS contrasts with the parabolic DOS observed in bulk materials, resulting in enhanced absorption at the step edges, which is leveraged in optoelectronic devices such as quantum well lasers.

In quantum wires, confinement occurs in two dimensions (e.g., y and z directions). These structures allow charge carriers to move freely along a single axis (x direction). For a quantum wire with cross-sectional dimensions L_y , and L_z , the energy levels are:

$$E_{n_y, n_z} = \frac{\hbar^2 \pi^2}{2m_e} \left(\frac{n_y^2}{L_y^2} + \frac{n_z^2}{L_z^2} \right) \quad (1-9)$$

The total energy includes this quantified component plus the kinetic energy in the unconfined direction:

$$E_{Total} = E_{n_y, n_z} + \frac{\hbar^2 k_x^2}{2m_e} \quad (1-10)$$

The density of states for a quantum wire follows an inverse square root dependence on energy:

$$\rho_{1D}(E) = \sum_{n_y, n_z} \frac{1}{\pi} \sqrt{\frac{2m_e}{\hbar^2 (E - E_{n_y, n_z})}} \theta(E - E_{n_y, n_z}) \quad (1-11)$$

This DOS exhibits characteristic singularities at the subband edges (van Hove singularities), leading to enhanced optical transitions at these energies [25].

Quantum Dots (QDs): Quantum dots represent the ultimate confinement case, with carriers restricted in all three spatial dimensions. This complete spatial confinement leads to the formation of discrete energy levels, analogous to those seen in isolated atoms-hence QDs also known as "artificial atoms." For a spherical quantum dot with radius R and infinite potential barriers, the energy levels can be approximated as:

$$E_{n,l} = \frac{\hbar^2 \chi_{n,l}^2}{2m_e R^2} \quad (1-12)$$

where $\chi_{n,l}$ represents the zeros of the spherical Bessel functions, and n and l are the principal and angular momentum quantum numbers, respectively [26]. The density of states for an ideal quantum dot consists of a series of delta functions:

$$\rho_{1D}(E) = 2 \sum_{n,l} (2l + 1) \delta(E - E_{n,l}) \quad (1-13)$$

where the factor $(2l + 1)$ accounts for the degeneracy due to the angular momentum. This fully discrete energy spectrum results in sharp, atom-like optical absorption and emission spectra, with linewidths primarily limited by homogeneous and inhomogeneous broadening mechanisms rather than by intrinsic DOS broadening [27]. As **Figure 1.2** shows, the quantum confinement effect gets stronger along with the decrease of system dimensionality. Consequently, the 0-D confinement system presents the highest quantum confinement effect[28].

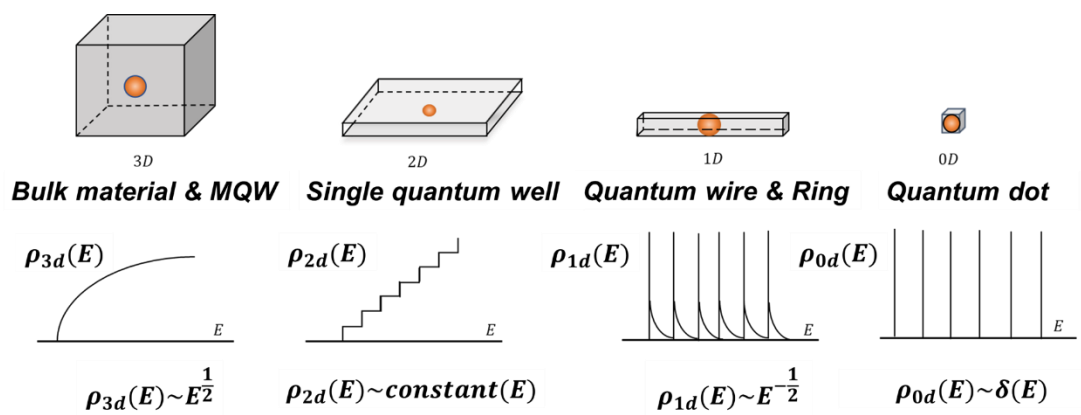


Figure 1.2 The illustration of dimension quantum confinement system and their DOS density.

1.1.3. THEORETICAL MODEL OF QUANTUM DOT ARRAYS

When semiconductor nanostructures formed periodic arrays, specifically for quantum dots, these arrays create a system where individual quantum states can interact through various coupling mechanisms to form collective states with emergent properties [29]. The spatial organization of quantum dots into ordered arrays creates a platform for investigating fundamental quantum mechanical interactions while enabling novel technological applications spanning photonics, electronics, and quantum information processing [30]. Firstly, considering quantum dots are placed in proximity, their electronic states can interact through two primary coupling mechanisms: direct wavefunction overlap and dipole-dipole interactions.

In closely spaced quantum dots, the wave functions extend beyond the physical boundaries of each dot. When these extensions overlap with neighbouring dots, they create direct electronic coupling, allowing electrons to tunnel between them which are known as direct wavefunction overlap. The strength of this coupling decreases exponentially as the distance between dots increases. A useful way to visualize this effect is to imagine each quantum dot as having an electronic cloud that thins out with distance. When two such clouds overlap, tunnelling can occur, facilitating electronic interaction between dots. The rate at which this coupling diminishes depends on how quickly the wavefunction decays outside the dot's boundary.

Even when wavefunction overlaps are negligible, quantum dots can still interact through near-field dipole-dipole coupling. This mechanism is like the way two magnets exert forces on each other without direct contact. The strength of dipole interactions decreases with the cube of the distance between dots—meaning that doubling the distance reduces the interaction strength by a factor of eight. Dipole-dipole interactions play a crucial role in the optical properties of quantum dot arrays, particularly in exciton

transfer, where an excited electron-hole pair in one dot can transfer energy to another without actual charge movement.

As quantum dots couple through these mechanisms, their discrete energy levels broaden into minibands, like the formation of energy bands in atomic crystals. The width of these minibands is approximately four times the coupling energy between nearest clusters. This transition marks a fundamental shift from atom-like behavior in isolated quantum dots to solid-like behavior in arrays. By controlling coupling strength, researchers can engineer quantum dot arrays with tailored electronic and optical properties, paving the way for advancements in quantum computing, photonics, and nanoscale electronics.

Figure 1.3 illustrates the fundamental progression of electronic states in semiconductor quantum dots as they transition from isolated entities to strongly coupled arrays, demonstrating the emergence of collective electronic behavior according to quantum confinement theory. The first panel depicts a single, isolated quantum dot where quantum confinement results in discrete energy levels (E_0, E_1, E_2), analogous to the electronic structure of atoms. These discrete levels arise from the three-dimensional spatial confinement of charge carriers, with energies that scale inversely with the square of the dot radius ($E \propto 1/R^2$). This quantization occurs when the dot dimensions approach the de Broglie wavelength of the charge carriers.

Miniband Formation in Quantum Dot Arrays

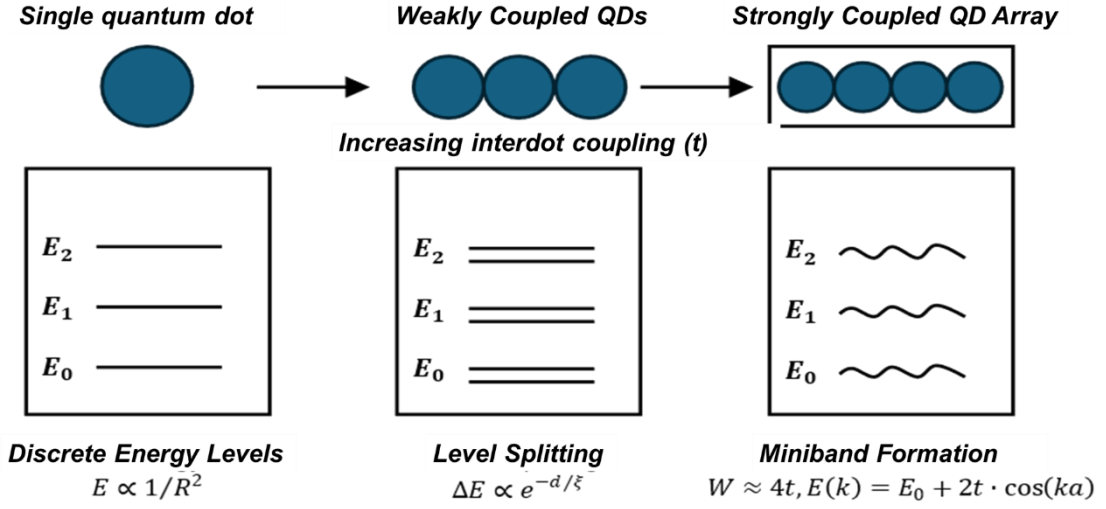


Figure 1.3 Schematic illustration diagram of miniband formation in quantum dot arrays.

For weakly coupled quantum dots, where neighbouring dots are positioned close enough to permit limited electronic interaction. This weak coupling induces level splitting, where each formerly discrete energy level divides into multiple closely spaced levels. The magnitude of this splitting (ΔE) follows an exponential dependence on the inter-dot separation distance (d) and the decay length of the confined wavefunction (ξ), expressed as

$$\Delta E \propto \exp\left(-\frac{d}{\xi}\right) \quad (1-14)$$

This splitting represents the onset of delocalization, where electron wave functions begin to extend beyond individual dots.

As a strongly coupled quantum dot array, where significant electronic overlap transforms the split levels into continuous minibands. These minibands exhibit dispersion relations like those in crystalline solids, with the energy becoming a function of wavevector (k):

$$E(k) = E^0 + 2t \cdot \cos(ka) \quad (1-15)$$

where t represents the coupling strength and a is the inter-dot spacing (lattice constant). The miniband width (W) is approximately $4t$, providing a direct measure of coupling strength in the array.

The electronic properties of quantum dot arrays fundamentally derived from the three-dimensional quantum confinement of charge carriers within individual dots, modified by interdot coupling. In isolated quantum dots, confinement produces discrete energy levels with wave functions that are spatially localized. The electronic properties are favoured to a strongly coupled quantum dot array scenario. When quantum dots are arranged in periodic arrays with controlled interdot spacing d , the overlap of electronic wavefunctions between neighboring dots creates coupling. This coupling strength decays exponentially with distance according to $t \propto \exp(-\beta d)$, where β depends on the barrier height and effective mass [31]. As this coupling increases, the discrete energy levels broaden into minibands with dispersion relations that can be described through tight-binding formalism [32]

$$E(k) = E^0 + 2t[\cos(k_x a) + \cos(k_y a) + \cos(k_z a)] \quad (1-16)$$

where a is a three-dimensional cubic array with lattice constant. The electronic transport in quantum dot arrays exhibits a complex interplay between quantum tunnelling and Coulomb blockade effects. The charging energy $EC = e^2/2C$, where C is the dot capacitance creates an energy barrier for electron transfer between dots. When the interdot coupling t exceeds a critical fraction of EC , a transition from insulating to conducting behavior occurs, enabling coherent charge transport across the array [33].

The optical properties of quantum dot arrays derive from both single dot excitonic transitions and collective interactions among dots. The absorption and emission spectra

of individual quantum dots are characterized by size-dependent transitions, with the bandgap energy scaling as $E_g \propto 1/R^2$ due to quantum confinement [21]

In arrays, however, these optical properties are substantially modified by interdot interactions. Dipole-dipole coupling, which scales as $V_{dd} \propto 1/d^3$, enables excitonic energy transfer between dots, leading to phenomena such as exciton diffusion and delocalization. When the interdot spacing becomes comparable to or smaller than the wavelength of emitted light, coherent coupling can produce superradiant states with enhanced radiative decay rates:

$$\Gamma_{collective} = N \cdot \Gamma_{individual} \quad (1-17)$$

where N represents the number of coherently coupled quantum dots [34]. The collective optical response of quantum dot arrays also manifests in modified absorption cross-sections and enhanced nonlinear optical susceptibilities. The third-order nonlinear susceptibility $\chi^{(3)}$ scales approximately with the fourth power of the transition dipole moment, making quantum dot arrays particularly promising for nonlinear optical applications [35].

Recent theoretical and experimental work has demonstrated that quantum dot arrays can exhibit topological band structures, supporting edge states with robust transport properties against disorder [36]. Additionally, the controlled arrangement of quantum dots enables the engineering of photonic band structures, creating photonic crystals with customizable spectral responses and photon localization capabilities [37].

The quantum confinement effects in arrays also manifest in enhanced carrier multiplication, where a single high-energy photon generates multiple electron-hole pairs through impact ionization processes. This phenomenon, particularly efficient in quantum dot solids due to relaxed momentum conservation requirements, has significant implications for photonic related applications [27].

1.2. THE DEVELOPMENT III-V COMPOUND SEMICONDUCTOR MATERIAL SYSTEM

The development of III-V compound semiconductor materials has profoundly shaped the fields of electronics and optoelectronics, offering superior properties such as direct bandgaps, high electron mobility, and versatile alloying capabilities for bandgap engineering [38]. These materials have become central to the evolution of advanced technologies, including high-speed transistors [39], photodetectors [40], and light-emitting devices [41], due to their exceptional physical and electronic characteristics. Over the decades, advances in synthesis methods, precise characterization, and application-driven research have accelerated their adoption and performance optimization. This review traces the historical milestones, key fabrication techniques, material advancements, and emerging trends that have defined the trajectory of III-V semiconductors.

1.2.1. III-V COMPOUND SEMICONDUCTORS FOR QUANTUM STRUCTURES

The origins of III-V semiconductor research can be traced back to the mid-20th century, as the need for materials with better optoelectronic performance than silicon became evident [42]. Early studies on gallium arsenide (GaAs) and indium phosphide (InP) highlighted their suitability for high-frequency and optical applications, attributed to their direct bandgaps and high electron mobility [42]. Notable milestones include the successful synthesis of GaAs in the 1950s and the introduction of liquid-phase epitaxy (LPE) in the 1960s, which facilitated the controlled growth of thin semiconductor layers [43]. Foundational work by researchers such as Kroemer (1963) demonstrated the transformative potential of heterojunctions in enhancing carrier confinement [44],

leading to their adoption in devices such as light-emitting diodes and microwave amplifiers [45].

Epitaxial growth techniques have been instrumental in the advancement of III-V materials. The advent of molecular beam epitaxy (MBE) in the 1970s marked a paradigm shift, enabling atomic-scale control over material composition and thickness [46]. R. Dingle (1974) demonstrated MBE's ability to produce defect-free, ultra-thin layers [47], catalyzing innovations such as quantum wells, superlattices[48], and high-electron-mobility transistors (HEMTs)[49]. Concurrently, metal-organic chemical vapor deposition (MOCVD) emerged as a scalable and industry-friendly technique[50], with Manasevit et al. (1971) highlighting its capability to grow complex heterostructures and alloy systems like AlGaAs and InGaAs[51]. These alloys became foundational for applications in photonics and high-speed electronics. The development of selective-area growth (SAG) techniques in the 1980s further enhanced the versatility of III-V semiconductors [52], enabling site-specific deposition for integrated optoelectronic devices, as demonstrated by Dapkus (1982) [53].

One of the defining strengths of III-V semiconductors lies in their ability to customize electronic and optical properties through alloying. The introduction of ternary and quaternary alloys, such as InGaAs, AlGaAs, and InAlGaP, allowed precise tuning of bandgap energy[54], enabling tailored solutions for specific applications. Stringfellow (1975) offered critical insights into the thermodynamics and phase stability of these alloys[55], laying the groundwork for their controlled synthesis and characterization[56]. The advent of quaternary compounds like InGaAsP expanded the material palette, particularly for telecommunications [57] and multi-junction solar cells[58], achieving unprecedented efficiency and bandwidth [59]. Strain-induced effects in pseudomorphic growth, theorized by Matthews and Blakeslee (1974) [60],

unlocked new possibilities for bandgap engineering, leading to the development of strained-layer superlattices with enhanced carrier mobility and modified electronic properties.

1.2.2. GROWTH AND INTEGRATION CHALLENGES

The characterization of III-V materials has been critical to their development. Techniques like transmission electron microscopy (TEM), x-ray diffraction (XRD), and photoluminescence spectroscopy are commonly used to evaluate material quality, interface properties, and optical behavior. Pioneering studies, such as those by Brantley W.A (1975) [61], highlighted the impact of defects like dislocations on device performance. Advances in defect engineering, including strategies like dislocation filtering [62] and substrate patterning [63], have significantly improved material quality. Innovations in substrate technology, including the introduction of semi-insulating GaAs substrates in the 1970s and lattice-matched substrates like GaSb [64], further enhanced the integration of III-V semiconductors into high-frequency devices [65]. The demonstration of III-V growth on silicon platforms by Fitzgerald et al. (1991) [66, 67] heralded a new era of heterogeneous integration, paving the way for III-V materials in CMOS-compatible systems [68].

The recent emergence of novel III-V materials and nanoscale device architectures has opened exciting opportunities in nanophotonics, quantum computing, and renewable energy. As the III-nitride materials, such as GaN and AlN, have expanded the III-V family to include wide-bandgap semiconductors, essential for high-power electronics and deep ultraviolet (UV) applications [69]. The revolutionary work on GaN-based blue LEDs by Nakamura et al. (1994) [70], which won the Nobel Prize in Physics in 2014, transformed solid-state lighting and energy efficiency standards. In parallel, nanoscale structures such as nanowires, quantum dots, and two-dimensional

materials have appeared as critical components for next-generation devices. Samuelson et al. (2004) demonstrated the utility of III-V nanowires in multi-junction solar cells [71], achieving superior conversion efficiencies with reduced material usage. Quantum dots, made possible by advanced epitaxial techniques, have become key to quantum information processing, as Michler et al. (2000) established their reliability as single-photon sources [72].

From **Figure 1.4**, the intrinsic relationship between lattice constants and bandgap energies further underscores the versatility of III-V materials. For example, materials with larger lattice constants, such as InSb, exhibit lower bandgaps, making them ideal for infrared detectors and low-voltage applications. The ability to finely tune these properties through alloying highlights the dominance of III-V semiconductors in advanced technologies, including multi-junction solar cells, which leverage their properties to maximize light absorption across the solar spectrum.

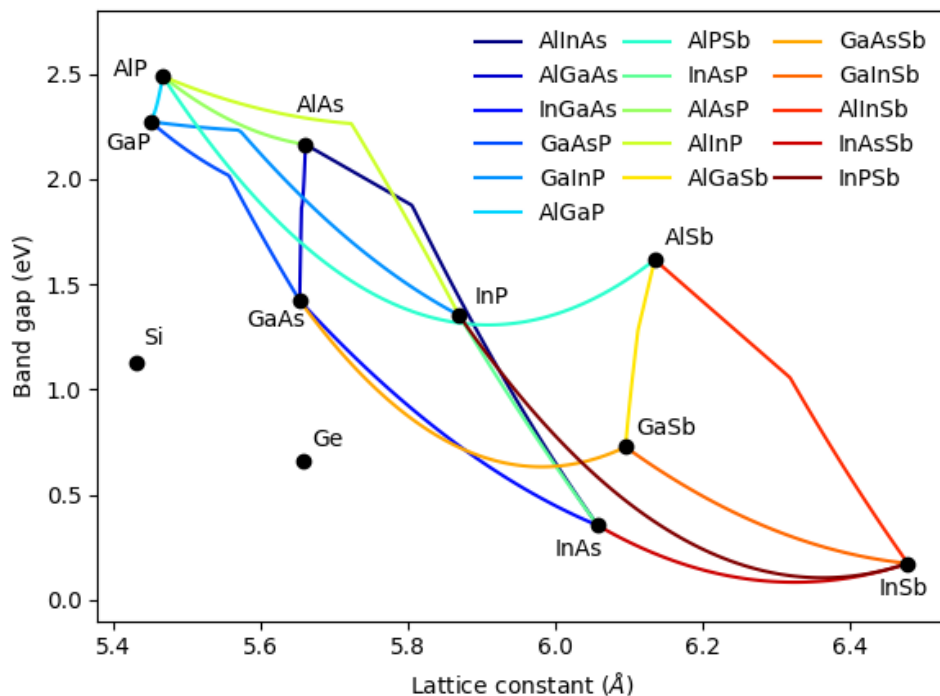


Figure 1.4 Calculated Bandgap energy Vs lattice constant of III-V compound materials and IV group material via SolCore [73].

Despite these advancements, challenges persist in the development and deployment of III-V semiconductors. High material costs [74], the complexity of epitaxial processes, and integration hurdles with silicon remain significant barriers [75]. Innovative solutions, such as epitaxial lift-off[76], wafer bonding [77], and alternative precursors [78], aim to address these issues. As III-V research advances, the focus is likely to shift toward energy-efficient devices, spintronics, and neuromorphic computing. The exploration of III-V nanostructures and their integration with emerging materials will continue to drive the next generation of semiconductor innovation.

1.3.HISTORICAL CONTEXT OF III-V SEMICONDUCTOR NANOSTRUCTURE ARRAY FABRICATION

This chapter examines the various approaches developed for the fabrication of ordered semiconductor QD arrays, with particular emphasis on III-V semiconductor materials. The strengths and limitations of different techniques, comparison of their performance metrics, and discussion current challenges and potential solutions for future development are being analysed.

The field of semiconductor nanostructure has experienced tremendous growth over the past three decades, offering remarkable potential for quantum information processing, quantum communication, and next-generation optoelectronic devices. QDs as the most unique potential in tunable electronic and optical properties among other semiconductor nanostructure that can be engineered through control of their size, shape and composition.

1.3.1. MULTILAYER VERTICAL STACKING

Multilayer vertical stacking represents the initial breakthrough in QD ordering, exploiting the propagation of strain fields from buried QDs through thin spacer layers to create preferential nucleation sites for subsequent QD layers. Xie et al. (1995) first demonstrated this phenomenon in the InAs/GaAs system, observing a vertical correlation between QDs in successive layers with spacer thicknesses below 30 nm [79]. This method was further refined by Tersoff [80], who developed a quantitative model describing the vertical alignment based on strain minimization principles. Subsequent work by Grigoriev et al. (2005) [81] and Wang et al. (2007) [82] extended this approach to create three-dimensional QD superlattices with improved uniformity. The methodology has evolved through progressive refinement of growth parameters, including optimized growth temperature profiles [83], precisely controlled spacer layer thickness gradients [84], and composition modulation [85] as the **Figure 1.5** (a) shows. While offering simplicity and scalability, this approach inherently suffers from limited lateral positional control and potential degradation of optical properties in lower QD layers due to accumulated strain effects and defect propagation. Recent advancements have focused on minimizing these limitations through strain-compensating layers [86] and growth interruption techniques [87] to improve structural perfection.

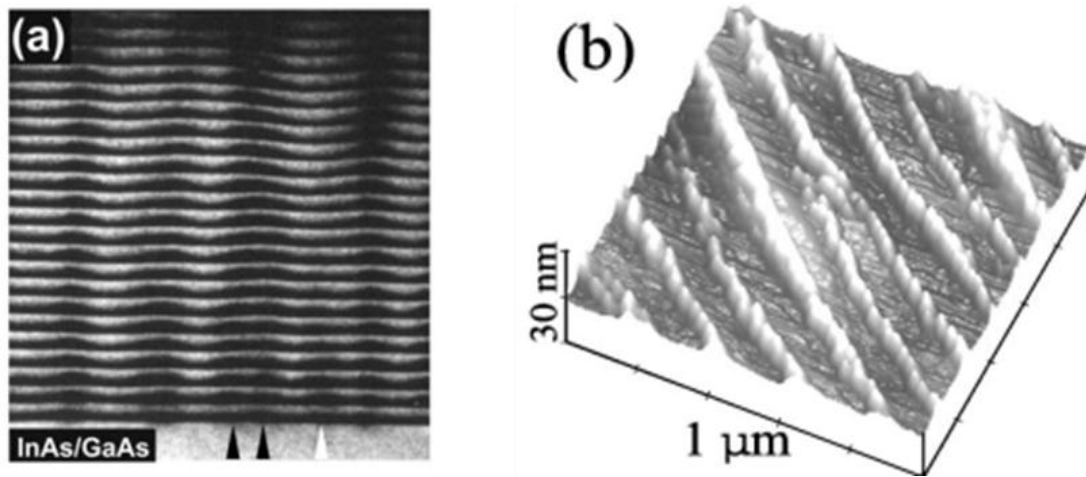


Figure 1.5 (a) TEM image of InAs/GaAs quantum dots with multiple vertical stacking technique [88]. (b) AFM image of InAs/GaAs quantum dots with self-organized anisotropic strain engineering [89].

1.3.2. SELF-ORGANIZED ANISOTROPIC STRAIN ENGINEERING

Self-organized anisotropic strain engineering represents a significant advancement, providing greater control over QD positioning by leveraging anisotropic strain fields generated by superlattice templates. Mano et al. (2002) [90] pioneered this approach by creating one-dimensional arrays of InAs QDs on GaAs using anisotropically strained (In, Ga) As superlattice templates. The methodology evolved through Wang et al.'s (2004) [91] demonstration of (In, Ga)As quantum dot chains on GaAs(100) and Nötzel et al.'s (2006) [92] work on quantum dot molecules. The developmental progression included refinements in superlattice design [93], with particular attention to balancing strain accumulation against crystalline quality, and optimization of growth interruption protocols to enhance surface diffusion anisotropy [94]. This approach offers high structural quality and maintenance of excellent optical properties since the growth occurs without ex-situ processing steps that might introduce contaminants as **Figure 1.5** (b) shows. However, significant limitations persist in pattern flexibility and the complexity of growth optimization, particularly in achieving uniform QD properties

across large areas. Recent work by Kim et al. (2021) [95] and Rodriguez et al. (2023) [96] has focused on combining anisotropic strain templates with minimal surface patterning to enhance positional control while maintaining structural integrity.

1.3.3. SITE-CONTROLLED GROWTH

Site-controlled growth on pre-patterned substrates marks a paradigm shift toward deterministic QD positioning through direct manipulation of the growth substrate as the **Figure 1.6** (a) shows. Within this category, electron beam lithography (EBL) emerged as a powerful technique capable of nanometer-scale resolution. Pioneered by Schmidt et al. (2000) [97] and subsequently refined by Ishikawa et al. (2000) [98], EBL-based approaches evolved through significant improvements in pattern transfer processes [99] and surface preparation techniques [100]. The developmental trajectory continued with Yakes et al.'s (2013) [101] breakthrough demonstration of deterministic growth of InAs QDs with extremely narrow optical linewidths (19 μeV) through crystal anisotropy exploitation. Parallel advances in nanoimprint lithography (NIL) by Heidemeyer et al. (2003) [102] and advanced by Tommila et al. (2011) [103] offered higher throughput alternatives, while AFM-assisted local oxidation nanolithography (LON) developed by Martín-Sánchez et al. (2009) [101] and refined by Herranz et al. (2015) [104] provided an alternative route for contamination-free patterning. Despite impressive progress, challenges remain in balancing positional accuracy with optical quality and in developing processes amenable to large-scale production. Recent innovations by Skiba-Szymanska et al. (2017) [105] and Albert et al. (2020) [106] have focused on

sophisticated in-situ cleaning processes and optimized buffer layer strategies to preserve optical quality while maintaining positional control.

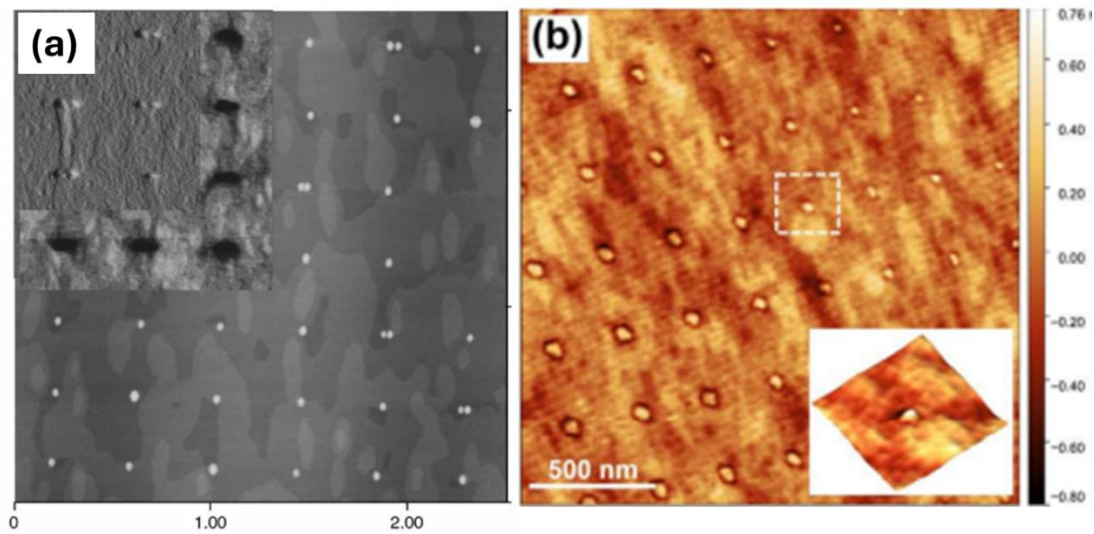


Figure 1.6 (a) AFM image of InAs/GaAs quantum dots with site-controlled growth on pre-patterned substrates [107]. (b) AFM image of InAs/GaAs quantum dots by Direct laser interference patterning [108].

1.3.4. DIRECT LASER INTERFERENCE PATTERNING (DLIP)

Direct laser interference patterning (DLIP) represents the most recent evolutionary stage, combining bottom-up self-assembly with in-situ surface modification. Initially demonstrated for semiconductor patterning by Clegg and Yang (2013) [109], the methodology was refined through Zhang et al.'s (2018) [110] work on in-situ laser nano-patterning for InAs/GaAs QD growth. A significant breakthrough came with Wang et al.'s (2020) [111] demonstration of precise arrays of epitaxial QDs nucleated by in-situ laser interference, achieving excellent optical properties (linewidth of 22 meV) together with precise positional control. The approach was further extended to droplet epitaxy by Han et al. (2021) [112], who demonstrated ordered GaAs QDs with record-narrow PL linewidths (17 meV). The developmental path of DLIP has focused on optimizing laser parameters [108], understanding the underlying photothermal

processes [113], and exploring applications across multiple material systems [114] as the **Figure 1.6** (b) shows.

Table 1.1 Comparison of current techniques towards self-assemble semiconductor nanostructure array.

Technique	Positional Accuracy	Single QD Yield	Optical Quality (FWHM)	Scalability	Implementation Complexity
Multilayer Stacking	Low (<500 nm)	<20%	30-50 meV	High	Low
Anisotropic Strain	Medium (<200 nm)	<30%	25-40 meV	Medium	Medium
EBL-Based	Very High (<10 nm)	>80%	10-30 meV	Low	Very High
NIL-Based	High (<50 nm)	>60%	30-50 meV	High	High
AFM-LON	Very High (<10 nm)	>80%	60-150 meV	Very Low	High
In situ DLIP	Medium (<100 nm)	>60%	16-22 meV	High	Medium

While offering significant advantages in maintaining pristine crystal quality through in-situ processing, challenges remain in optimizing interference pattern uniformity and in developing optical configurations compatible with production-scale MBE systems. As **Table 1.1** shows, current research directions focus on beam-shaping techniques and hybrid approaches combining minimal ex-situ patterning with in-situ laser modification to enhance pattern fidelity while maintaining optical quality.

The evolution of these fabrication methodologies reveals a clear developmental trajectory toward increasing control over QD positioning while maintaining or enhancing optical quality. From the initial exploitation of natural strain-driven processes in vertical stacking, through the deliberate engineering of anisotropic strain

fields, to direct substrate patterning and in-situ surface modification, each approach has contributed valuable insights and technological capabilities. Future development will likely focus on hybrid methodologies that combine the strengths of multiple approaches, advanced in-situ techniques that maintain crystal quality while achieving precise positioning, and integration strategies that address the challenges of incorporating ordered QD arrays into functional quantum photonic circuits and other device architectures.

1.4. PROJECT MOTIVATION AND OBJECTIVES

III-V compound semiconductor quantum dots (QDs) have established themselves as critical components for advanced quantum systems, particularly in quantum communication and computing applications. In quantum communication, III-V QDs excel as single-photon sources with exceptional purity. InAs/GaAs QDs demonstrate near-ideal photon statistics with second-order correlation values approaching zero, confirming their ability to emit exactly one photon per excitation event[115]. Furthermore, these QDs can generate entangled photon pairs through the biexciton-exciton cascade process, enabling quantum teleportation and forming the basis for quantum repeaters essential in long-distance quantum networks[116]. For quantum computing applications, electron spins in III-V QDs present compelling advantages as qubits. With coherence times exceeding microseconds and the capability for ultrafast optical manipulation, these systems offer a promising platform for quantum information processing [116]. These nanoscale structures derive their importance from their unique ability to confine carriers in three dimensions, creating discrete energy states that can be precisely engineered through compositional and dimensional control [117, 118]. Recent advancements in deterministic QD positioning [111, 119] and

demonstrations of fault-tolerant quantum operations [120] have further strengthened their position as leading candidates for scalable quantum technologies.

Despite their promising attributes, several challenges impede the widespread implementation of III-V QDs in practical quantum systems. Foremost among these is the issue of structural inhomogeneity. Conventional growth techniques like Stranski-Krastanov yield QDs with size and composition variations, resulting in spectral inhomogeneities that compromise the fidelity of quantum confinement effect [121]. Conventional growth techniques struggle to achieve precise spatial positioning. This limitation necessitates complicated *ex-situ* (post-growth) treatment processes. These processes are required to enable the scalability of potential integrated photonic applications [122]. Consequently, a new technique is demanded. This technique must be able to satisfy the requirements for high crystalline quality and excellent optical characteristics in III-V quantum dots (QDs). This technique must achieve this via Molecular Beam Epitaxy (MBE). The direct-laser interference patterning (DLIP) as a promising technique that emerges the advantage of high-quality QD growth techniques and equivalent *in-situ* lithography, which fulfil the potential towards most of the challenges. By generating interference patterns with multiple coherent laser beams, DLIP creates precisely defined periodic surface modifications that serve as nucleation sites for subsequent epitaxial growth stage [123]. The *in-situ* implementation of DLIP within molecular beam epitaxy (MBE) chambers represents a significant advancement, allowing surface patterning and epitaxial growth to occur within the same ultra-high vacuum environment. This integrated approach eliminates contamination risks associated with *ex-situ* processing and maintains the pristine material quality essential for quantum coherence [124]. The single-step nature of this process enhances reproducibility and scalability compared to conventional lithographic techniques

1.5. THESIS OUTLINES

This work investigates the impact of growth parameters on III-V self-assembled quantum dot arrays. It also investigates the corresponding characterization of these arrays. The studied arrays include InGaAs/AlGaAs/GaAs droplet epitaxy quantum dots. They also include InAs/GaAs Stranski-Krastanow quantum dots (SKQDs) and InAs/GaAs droplet epitaxy quantum dots (DEQDs). The investigation applies in-situ direct laser interference patterning during MBE growth. The outlines of each chapter are listed as given below::

Chapter 2 firstly explains the keystone theory of the molecular beam epitaxy, including the surface kinetic process and growth mode towards heterogeneous material system. Then the details of deposition methods for heterogeneous self-assembled quantum dot array, including S-K mode growth, droplet epitaxy and direct laser interference patterning.

Chapter 3 introduces the Molecular Beam Epitaxy (MBE) system used to grow all samples in this thesis work. It also introduces the characterization methods employed. The chapter includes an introduction to the MBE system and describes its key features. It covers the use of Atomic Force Microscopy (AFM) for analyzing surface morphology. It also covers the use of photoluminescence (PL) spectroscopy. Furthermore, it provides a detailed explanation of the Micro-photoluminescence (Micro-PL) spectroscopy setup. The chapter explains the principle of Micro-PL spectroscopy. This explanation includes its application for temperature-dependent photoluminescence measurements. It also includes its application for power-dependent photoluminescence measurements. Finally, it includes its application for time-resolved photoluminescence measurements.

Chapter 4 presents the auto-mapper system towards intensity and wavelength mapping for III-V self-assembled quantum dot array. The system objectives are

introduced initially, then the innovation system set-up versus various programming platform for different application, the system flow chart and example of the system.

Chapter 5 outlines the combined use of DLIP and DE within MBE systems to fabricate ordered InGaAs QD arrays. Through systematic analysis of growth conditions, structural features, and optical properties, we seek to bridge the gap between random QD formation and deterministic integration—a key requirement for quantum photonic circuit realization.

Chapter 6 presents the growth and characterization of InAs quantum dots via droplet epitaxy, focusing on the effects of indium coverage and capping temperature. It analyses morphological evolution, emission properties, and thermal stability, establishing optimal conditions for high-quality QD formation and highlighting mechanisms of degradation under non-ideal growth parameters.

Chapter 7 concludes the thesis and lays out the future work based on current study.

2.EPITAXY OF III-V SEMICONDUCTOR NANOSTRUCTURE ARRAY VIA MOLECULAR BEAM EPITAXY

This chapter focuses on the details of the MBE enable precise atomic-layer deposition under ultra-high vacuum for semiconductor growth. Three modes: layer-by-layer, island formation, and layer-plus-island—create nanostructures through controlled surface processes. Key techniques include Stranski-Krastanov growth, Droplet Epitaxy, and Laser Interference Patterning, producing quantum structures with demanded designed properties.

2.1.THE SEMICONDUCTOR QUANTUM CONFINEMENT SYSTEM

Molecular Beam Epitaxy (MBE) has emerged as one of the most precise and versatile method for the growth of high-purity epitaxial layers. Since its development in the late 1960s at Bell Laboratories by Arthur and Cho (1968) [125], MBE has become a fundamental tool for fabricating atomically precise semiconductor heterostructures.

The key advantage of MBE is the capability of abrupt heterojunctions growth with atomic layer precision. This precision, combined with the capability to grow complex layered structures with controlled doping profiles, has made MBE instrumental in the development of advanced optoelectronic devices and for fundamental studies of quantum phenomena in low-dimensional material systems [126].

The principle of MBE involves the deposition of constituent elements onto a heated crystalline substrate under ultra-high vacuum (UHV) conditions (typically 10^{-8} to 10^{-11} mbar). Unlike other epitaxial techniques, MBE relies on the ballistic transport

of molecular or atomic beams from effusion cells to the substrate surface, with minimal gas-phase interactions along the path [127]. The ultra-high vacuum environment not only enables this ballistic transport but also ensures minimal contamination, leading to exceptionally high material purity.

In a standard solid-source MBE system, separate effusion cells containing ultra-pure elemental sources (Ga, In, Al, As, Sb, etc.) are heated to produce controlled fluxes of atoms or molecules. These cells are arranged geometrically to direct their beams toward the substrate mounted on a manipulator that allows rotation and precise temperature control. The molecular beams can be abruptly interrupted by mechanical shutters, enabling sharp interfaces between different compositions and precisely controlled layer thicknesses down to a single atomic layer [128].

The substrate temperature is a critical parameter that significantly influences the kinetics and thermodynamics of growth. It must be controlled with high precision, typically within $\pm 1^\circ\text{C}$, to ensure reproducible growth conditions. For GaAs and related III-V materials, typical growth temperatures range from 480°C to 650°C , depending on the specific material system and desired structure [129].

Mathematically, the growth rate (GR) in MBE can be expressed using the following equation:

$$GR = \varphi \times s \times \left(\frac{M}{\rho NA} \right) \quad (2-1)$$

where φ is the incident flux (atoms/cm²·s), s is the sticking coefficient (typically close to unity for group III elements at standard growth temperatures), M is the molar mass of the grown material, ρ is its density, and NA is Avogadro's number. For typical III-V semiconductor growth, rates are in the range of 0.1-1.0 $\mu\text{m}/\text{hour}$, corresponding to approximately 0.2-2.0 monolayers per second (ML/s) [130].

The in-situ monitoring of growth is commonly performed using Reflection High-Energy Electron Diffraction (RHEED). The RHEED technique provides real-time information about the surface crystallography, growth mode, and growth rate through the observation of intensity oscillations during layer-by-layer growth. Each complete oscillation corresponds to the formation of one monolayer, allowing for precise calibration of growth rates [131].

The growth mechanisms in MBE are governed by complex surface kinetics and thermodynamics, involving multiple atomic processes that determine the final morphology of epitaxial layers. Understanding these mechanisms is crucial for controlling the fabrication of sophisticated nanostructures, particularly self-assembled quantum dots.

2.1.1. SURFACE KINETIC PROCESS

Molecular beam epitaxy (MBE) is a highly precise technique for depositing epitaxial layers and nanoscale structures. The process relies on effusion cells to generate a flux of the chosen material by heating it to an appropriate temperature. This produces a molecular beam of evaporated material that travels toward the substrate in a reaction chamber maintained under ultra-high vacuum (typically around 10^{-10} to 10^{-11}) [125, 132]. The growth mechanisms in MBE are governed by complex surface kinetics and thermodynamics, involving multiple atomic processes that determine the final morphology of epitaxial layers which shows in **Figure 2.1**. Understanding these mechanisms is crucial for controlling the fabrication of sophisticated nanostructures, particularly self-assembled quantum dots.

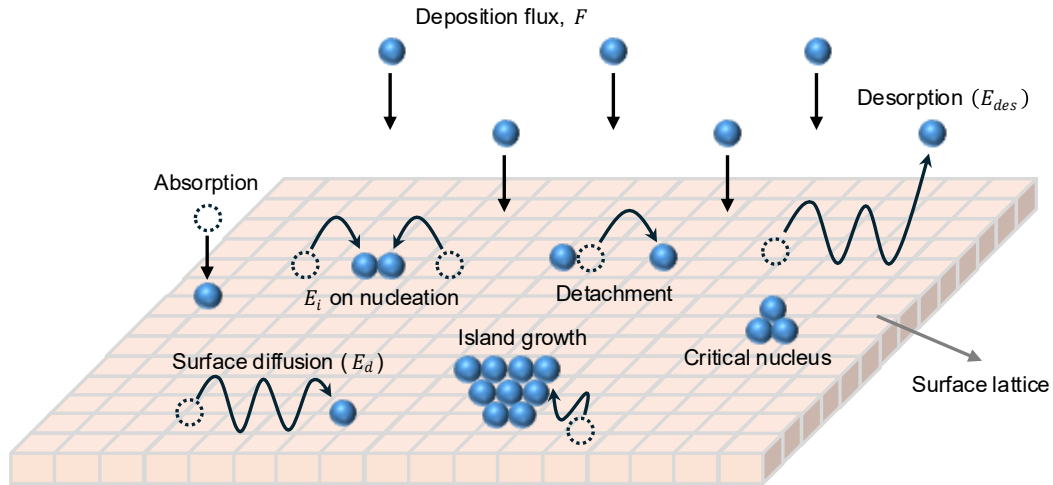


Figure 2.1 Schematic representation of the three fundamental growth modes in epitaxial systems.

2.1.1.1. THE PRE-NUCLEATION STAGE

The adsorption of atoms or molecules from incident molecular beams onto a substrate surface constitutes the initial step in epitaxial growth. This process can be quantitatively described through the sticking coefficient S , which represents the probability that an impinging particle will adsorb onto the surface [133]:

$$S = \frac{N_{\{ads\}}}{N_{\{inc\}}} \quad (2-2)$$

where $N_{\{ads\}}$ is the number of adsorbed particles and $N_{\{inc\}}$ is the number of incident particles. The sticking coefficient is not a constant number but rather depends on substrate temperature, surface coverage, and chemical nature of both adsorbate and substrate. For many III-V semiconductor systems, S approaches unity at conventional growth temperatures for group III elements but exhibits stronger temperature dependence for group V species [134].

Upon adsorption, atoms form a transient mobile phase of adatoms whose surface diffusion is a thermally activated process. The temperature-dependent diffusion coefficient (D) follows an Arrhenius relationship [128]:

$$D = D_0 \exp\left(-\frac{E_d}{k_B T}\right) \quad (2-3)$$

where D_0 is the pre-exponential factor (typically on the order of 10^{-3} to 10^{-4} cm²/s), E_d is the diffusion energy barrier, k_B is Boltzmann's constant, and T is the substrate temperature. The diffusion length λ , representing the average distance an adatom travels before being incorporated or desorbed, can be expressed as:

$$\lambda = \sqrt{D\tau} \quad (2-4)$$

where τ is the residence time of the adatom on the surface. This parameter fundamentally controls the island density and, consequently, the growth mode [135].

2.1.1.2. NUCLEATION STAGE

The nucleation of stable clusters occurs when diffusing adatoms encounter each other with sufficient frequency to overcome the critical cluster size barrier. According to classical nucleation theory for MBE, the density of stable nuclei is given by [133]:

$$n_x \propto \left(\frac{F}{D}\right)^{\frac{i}{i+2}} \exp\left(\frac{E_i}{(i+2)k_B T}\right) \quad (2-5)$$

where F is the deposition flux, i is the critical nucleus size, and E_i is the binding energy of the critical nucleus. This equation demonstrates the crucial dependence of nucleation density on the ratio of deposition rate to diffusion coefficient, a parameter that can be experimentally controlled.

Once stable nuclei form, they serve as preferential attachment sites for subsequent adatoms. The growth of these islands can be modelled through a set of coupled differential equations describing the evolution of island size distributions [136]:

$$\frac{dN_s}{dt} = \sigma_{s-1}DN_{s-1}n_1 - \sigma_sDN_s n_1 - K_s N_s \quad (2-6)$$

where N_s is the density of islands containing s atoms, n_1 is the adatom density, σ_s is the capture number for islands of size s , and K_s is the rate of direct impingement onto islands. For self-assembled nanostructure, the higher K_s would be favoured for

After the nucleation stage with reaching elevated temperatures, adatoms may acquire sufficient thermal energy to overcome the desorption barrier. The desorption rate R_{des} follows an Arrhenius relationship[137].

$$R_{des} = \nu \exp\left(-\frac{E_{des}}{k_B T}\right) \quad (2-7)$$

where ν is the attempt frequency (typically on the order of 10^{13} s⁻¹) and E_{des} is the desorption energy barrier. The competition between desorption and incorporation significantly influences growth efficiency and can be quantified through the incorporation probability P_{inc} which is proportional to incorporation rate [137, 138].

2.1.2. EPITAXIAL GROWTH TOWARDS HETEROGENEOUS STRUCTURE

Heterogeneous structures in MBE consist of multiple layers of different materials, often with varying compositions and lattice constants. These structures enable complex functionalities by combining the unique properties of each material. For example, heterostructures are used to create quantum wells, superlattices, and heterojunctions, which are fundamental in optoelectronics and high-speed devices.

The growth of heterogeneous structures via molecular beam epitaxy (MBE) requires meticulous management of lattice mismatch, interfacial quality, and abrupt compositional changes to ensure high-quality devices. MBE enables atomic-level precision through layer-by-layer deposition, allowing distinct layers with sharp interfaces by alternating source materials, such as Ga and In for GaAs and InAs. Lattice

mismatch, a critical factor, introduces strain at the interface as **Figure 2.2** shows for small mismatches, strain is elastically accommodated (pseudomorphic growth), but for larger mismatches or thicker layers, dislocations form to relieve strain (relaxed growth), potentially degrading performance. The ultrahigh vacuum environment of MBE ensures abrupt interface formation, critical for structures like quantum wells and superlattices where sharp transitions enhance confinement effects. Alloy composition can be finely tuned by co-evaporating materials, enabling precise bandgap engineering and graded layers. Substrate temperature optimization further promotes epitaxial growth while minimizing interdiffusion or segregation. These capabilities allow MBE to create advanced structures such as quantum wells, which confine carriers in two dimensions for use in lasers, LEDs, and photodetectors; superlattices, which stack alternating thin layers to control electronic and optical properties for applications like thermoelectric devices and tunable lasers; and heterojunctions, which interface materials with different bandgaps to enable high-efficiency solar cells and transistors.

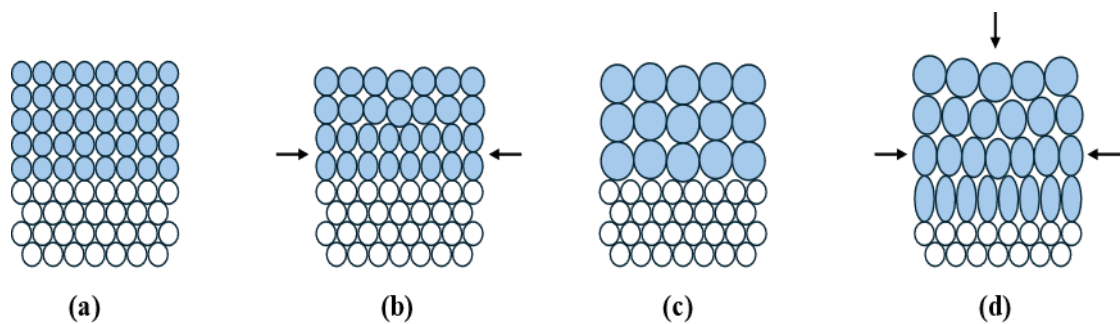


Figure 2.2 Schematic diagram of (a) epitaxial growth of lattice match structure, (b) epitaxial growth of minor lattice mismatch, (c) non- epitaxial growth of major lattice mismatch and (d) epitaxial growth despite of large lattice mismatch with strong strain relaxation.

For heterojunctions, thermally activated intermixing of constituent atoms can compromise interface abruptness. The interdiffusion coefficient D_{int} is given by:

$$D_{int} = D_{int,0} \exp\left(-\frac{E_{int}}{k_B T}\right) \quad (2-8)$$

where E_{int} is the activation energy for interdiffusion. The characteristic interdiffusion length λ_{int} after growth time t can be estimated as:

$$\lambda_{int} = \sqrt{D_{int} t} \quad (2-9)$$

Recent studies employing atom probe tomography have provided direct visualization of these interdiffusion profiles at various heterointerfaces [139].

The relative rates of the kinetic processes determine the prevailing growth mode: Frank-van der Merwe (layer-by-layer), Volmer-Weber (island), or Stranski-Krastanov (layer-plus-island). This can be understood through a dimensionless parameter χ , representing the ratio of characteristic times for diffusion to deposition [130]:

$$\chi = \frac{\tau_{diff}}{\tau_{dep}} = \frac{L^2/D}{1/F} = \frac{FL^2}{D} \quad (2-10)$$

where L is the average terrace width. Layer-by-layer growth is generally favored when $\chi \ll 1$, while island growth dominates when $\chi \gg 1$ [140].

Understanding these kinetic processes enables rational design of growth protocols for advanced heterostructures. For example, modulation of substrate temperature can strategically balance surface diffusion against desorption to optimize morphological evolution. Similarly, growth interruptions can be employed to allow surface reorganization through enhanced diffusion prior to subsequent layer deposition.

The quantitative understanding of surface kinetic processes provides a powerful framework for predicting and controlling the structural and compositional evolution during MBE growth. Recent advances in in-situ characterization techniques, combined with first-principles calculations, continue to refine our understanding of these fundamental processes, enabling ever more precise control over advanced heterostructure growth [141, 142]. Experimental data should be presented showing the

evolution of surface morphology under different growth conditions, illustrating the transition between growth modes as a function of temperature [143] and deposition rate [144].

In summary, Molecular beam epitaxy (MBE) enables the precise fabrication of both homogeneous and heterogeneous semiconductor structures, supporting advanced functionalities in devices like lasers, photodetectors, and high-electron-mobility transistors. However, key challenges persist. Lattice mismatch can induce strain and dislocations, degrading device performance; this is addressed through strategies like buffer layers and graded compositions. Material interdiffusion at interfaces impacts the performance of quantum wells and superlattices, necessitating meticulous control of growth parameters. Additionally, MBE's low throughput and high cost limit its scalability to industrial applications, confining its primary use to research and specialized domains. Despite these challenges, ongoing advancements in strain management, interface precision, and throughput enhancement continue to expand MBE's potential in next-generation electronics and optoelectronics.

2.2. DEPOSITION METHOD OF III-V COMPOUND SEMICONDUCTOR NANOSTRUCTURE ARRAY USING MBE

Among the most widely studied epitaxial growth mechanisms are the Stranski-Krastanov (SK) growth mode, droplet epitaxy (DE), and other techniques that enable the fabrication of nanostructures with specific morphologies, compositions, and dimensions. These approaches are critical for achieving high-quality nanostructures such as quantum dots, nanowires, and quantum rings, which exhibit unique quantum confinement effects. This review examines the principles, advantages, and challenges

of SK growth, droplet epitaxy, and alternative epitaxial techniques, with a focus on their relevance to III-V semiconductor systems.

2.2.1. STRANSKI-KRASTANOV MODE

The Stranski-Krastanov (SK) growth mode as one of the most widely used techniques for self-assembled quantum dot (QD) fabrication, this growth mechanism occurs during the epitaxial deposition of materials with a lattice mismatch, leading to the formation of coherent strained islands after the growth of a wetting layer.

2.2.1.1. PRINCIPLE OF SK-MODE

The epitaxial growth of semiconductor nanostructures is a cornerstone in the development of advanced optoelectronic and quantum devices. The thermodynamic driving forces and kinetic limitations lead to three canonical growth modes as **Figure 2.3** shows[145]:

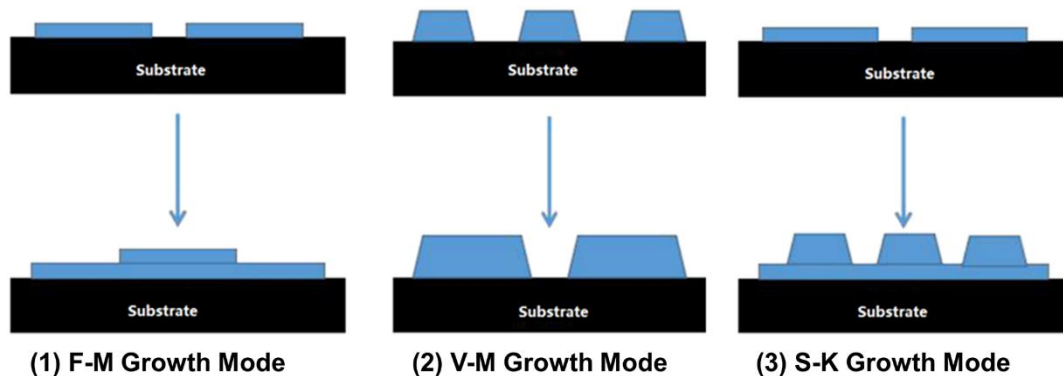


Figure 2.3 Schematic process diagram of different growth mode (1) Frank-Van der Merwe (F-M) mode. (2) Volmer-Weber mode. (3) Stranski-Krastanov mode

- Frank-van der Merwe (layer-by-layer): characterized by complete wetting of the substrate, occurs when adatom-substrate interactions exceed adatom-adatom interactions.
- Volmer-Weber (island): characterized by three-dimensional island formation, occurs when adatom-adatom interactions exceed adatom-substrate interactions.
- Stranski-Krastanov (layer-plus-island): involves initial layer-by-layer growth followed by island formation, typically observed in lattice-mismatched heteroepitaxy once a critical thickness is exceeded.

These growth modes can be quantitatively understood through the balance of surface free energies:

$$\Delta\gamma = \gamma_f + \gamma_i - \gamma_s \quad (2-11)$$

where γ_f, γ_i and γ_s represent the surface free energies of the film, interface, and substrate [146], respectively. Frank-van der Merwe growth occurs when $\Delta\gamma \leq 0$, while Volmer-Weber growth dominates when $\Delta\gamma > 0$ which as **Figure 2.4** shows.

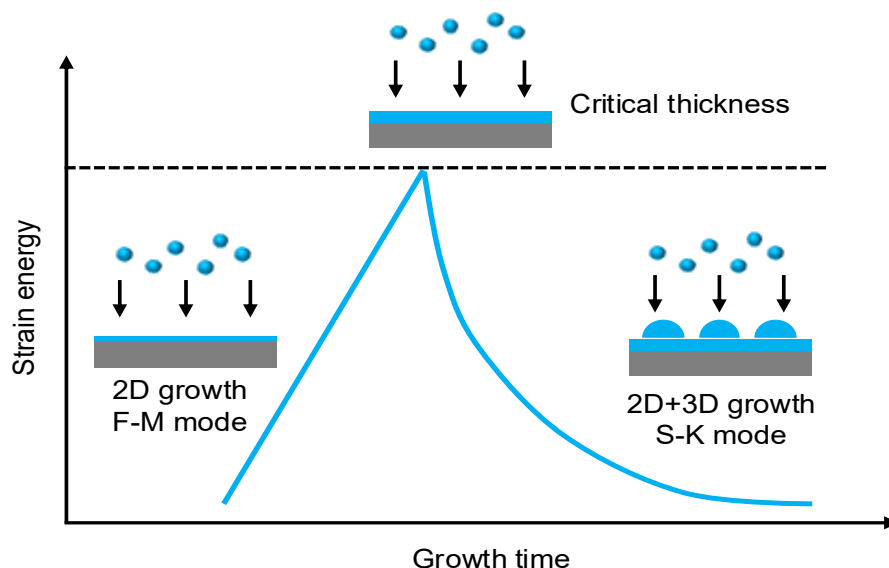


Figure 2.4 Schematic diagram of S-K mode conditions with growth time and strain energy.

The SK growth mode begins with the formation of a wetting layer, a uniform film that grows epitaxially on the substrate surface. Beyond critical thickness, strain energy accumulates due to lattice mismatch between the deposited material and the substrate. To minimize this strain, the material transitions from two-dimensional (2D) layer growth to three-dimensional (3D) island formation. These islands, typically a few nanometres in size, are the building blocks of quantum dots. Studies by Matthews and Blakeslee (1974) [147] provided the theoretical basis for understanding strain relaxation in SK growth. Later, Grundmann et al. (1995) [148] demonstrated the successful formation of InAs quantum dots on GaAs substrates, which became a model system for SK growth. The SK growth mode also offers distinct advantages and challenges in the fabrication of quantum dots. One key advantage is its reliance on self-assembly, where quantum dots form spontaneously without requiring external patterning. This method produces high-quality, defect-free 3D islands due to coherent strain relaxation during growth. Additionally, SK growth is versatile, accommodating various material systems such as InAs/GaAs, Ge/Si, and CdSe/ZnSe. In lattice-mismatched systems, strain energy accumulates with film thickness which is linear to the material misfit strain factor and film thickness. Thus, when the strain energy contributes to the transition from two-dimensional to three-dimensional growth, the corresponding layer thickness was considered as the critical thickness. Furthermore, the incorporation kinetics are significantly complicated by the different behaviors of group III and group V elements when epitaxial of compound semiconductor via MBE. The growth rate is typically limited by the group III flux due to the near-unity sticking coefficient, while the group V elements provide an overpressure that ensures stoichiometric growth [149].

2.2.1.2. GROWTH PARAMETERS OF SK-MODE

For the impact of growth parameters on SK mode for heterogeneous material system, several parameters present crucial factor on the final nanostructure quality which including growth temperature, wetting layer thickness, substrate orientation and capping layer growth. From **Equation 2-8**, with the increased growth temperature during the nucleation stage would enhance the surface diffusion, resulting in larger dots with reduced density. Molecular beam epitaxy (MBE) growth rate similarly affects QD morphology, with slower deposition rates (0.01-0.05 ML/s) promoting thermodynamic equilibrium conditions and yielding more uniform size distributions through enhanced surface diffusion[150]. As the **Figure 2.5** shows, the wetting layer thickness, typically 1.5-1.7 monolayers for InAs/GaAs, determines the critical thickness for elastic strain relaxation and subsequent QD nucleation. Material strain, which proportional to lattice mismatch (7.2% for InAs/GaAs), fundamentally drives SK growth, with higher strain promoting smaller QDs at increased densities through enhanced nucleation rates [151].

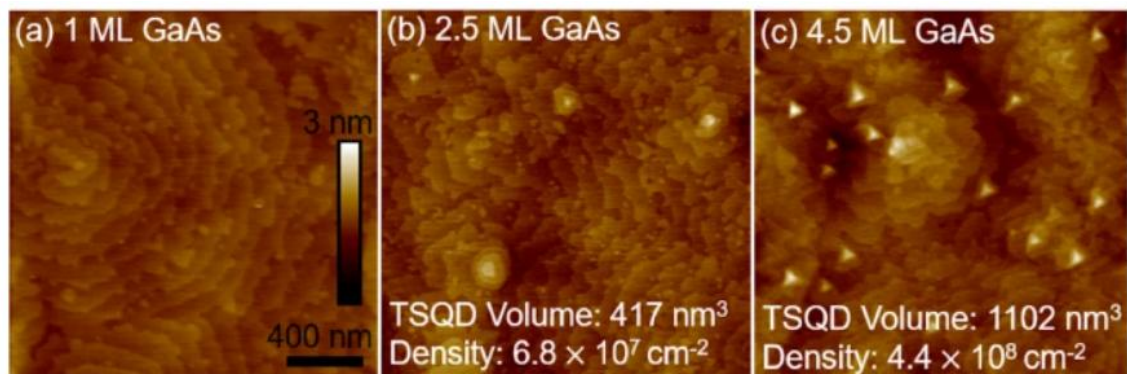


Figure 2.5 $2 \times 2 \mu\text{m}^2$ AFM images showing evolution of the surface morphology of GaAs quantum dots with increasing GaAs deposition amount: (a) 1 ML. (b) 2.5 ML. and (c) 4.5 ML [146].

Another factor presents tremendous influence is known for substrate misorientation which introduces stepped surfaces that act as preferential nucleation

sites, with slight off-cuts (typically 2-6°) promoting lateral ordering through step-flow growth mechanisms [152]. Post-growth thermal annealing (700-850°C) induces controlled In-Ga intermixing, modifying composition profiles and strain distributions, resulting in blue-shifted emission and narrowed linewidths through compositional homogenization [153]. And the cap layer growth conditions are critically influence QD preservation as well, with lower capping temperatures (450-480°C) reducing In segregation and composition intermixing, thereby preserving the as-grown QD structural properties [154]. Recent advanced techniques including growth interruption protocols, strain-reducing layers, and surfactant-mediated growth have demonstrated enhanced control over SK-QD uniformity, addressing the inherent statistical nature of self-assembly processes [23].

To be conclude, the technique is constrained by the need for a high degree of lattice mismatch to induce strain-driven island formation, limiting the range of material combinations. Despite these challenges, quantum dots produced via SK growth are widely utilized in optoelectronics, including quantum dot lasers and intermediate band solar cells, and as single-photon emitters in quantum communication systems, highlighting their importance in advanced technological applications.

2.2.2. DROPLET EPITAXY

Droplet epitaxy (DE) is an alternative technique that enables the fabrication of nanostructures without the need for a wetting layer or high lattice mismatch. In this approach, nanostructures such as quantum dots, rings, and disks are formed from liquid metal droplets on the substrate surface.

Droplet epitaxy (DE) is a versatile technique for fabricating III-V semiconductor nanostructures through a two-step process involving droplet formation and

crystallization. As **Figure 2.6** shows, for the first stage, metal atoms (group III) such as Ga or In are deposited onto a substrate under ultra-high vacuum (UHV) conditions, coalescing into nanoscale droplets. In the second step, these droplets are exposed to a group V source, such as Arsenic or nitrogen, which reacts with the metal to transform the droplets into crystalline nanostructures. The shape, composition, and properties of these structures can be precisely controlled by tuning growth parameters like substrate temperature and material fluxes. Initially demonstrated by Koguchi et al. (1993) [155] for the formation of GaAs quantum dots, DE has since been extended by Mano et al. (2005) [156] to create more complex geometries, such as quantum rings.

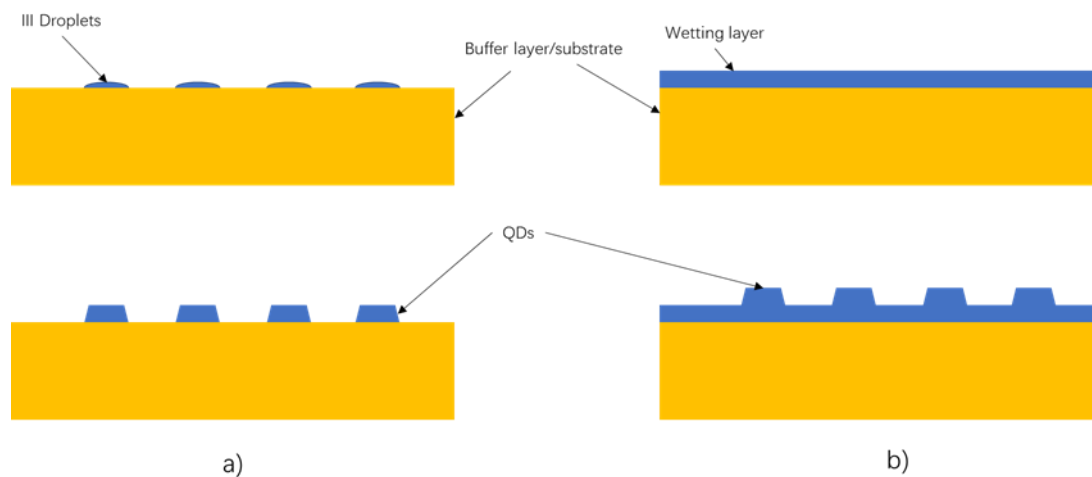


Figure 2.6 Schematic process diagram for DE and SK via MBE a) Droplet epitaxy b) SK mode

A key advantage of DE is its wide material flexibility, as it is not limited by lattice mismatch, allowing for the growth of diverse material systems. Additionally, DE can produce unconventional nanostructures, such as quantum rings, and is conducted at lower temperatures, reducing thermal stress on the substrate. However, challenges remain, including achieving uniform droplet size and distribution, managing surface roughness during droplet formation, and optimizing deposition and crystallization parameters. DE has proven particularly valuable for fabricating strain-free quantum

dots used in high-efficiency light-emitting devices and for quantum rings employed in photonic and sensing applications. Its ability to produce unique geometries holds promise for advanced technologies, including quantum information processing.

Despite its versatility, DE presents several challenges. The two-step growth process introduces complexity and potential reproducibility issues compared to single-step epitaxial techniques. Precise control over droplet crystallization kinetics remains difficult, particularly at low temperatures where surface diffusion is limited, resulting in incomplete crystallization and residual metal incorporation [157]. Surface oxidation during the growth interruption between droplet formation and crystallization can introduce unintended defects, necessitating careful process control and potentially specialized buffer layers [158]. Additionally, DE-grown nanostructures often exhibit broad size distributions (statistical variation ~15-20%) compared to Stranski-Krastanov quantum dots (~8-12%), requiring post-growth selection techniques for applications demanding high uniformity [158]. The low growth temperatures, while advantageous for certain applications, can induce point defects and excess arsenic incorporation, deteriorating optical properties through non-radiative recombination centers. Post-growth thermal annealing at 550-650°C can partially mitigate these defects but introduces structural modifications [159]. Recent advancements employing modified droplet epitaxy protocols with continuous group V background flux during droplet formation (hybrid droplet epitaxy) demonstrate improved crystalline quality and optical properties, though at the expense of reduced morphological control [160].

In conclusion, droplet epitaxy represents a powerful technique for fabricating semiconductor nanostructures with unique advantages in strain engineering and morphological control, though practical implementation requires careful consideration

of process parameters to overcome inherent limitations in crystallization control and defect formation.

2.2.3. DIRECT LASER INTERFERENCE PATTERNING

Direct laser patterning (DLIP) represents a powerful methodology for achieving site-controlled epitaxy of III-V semiconductor nanostructures, addressing the inherent spatial randomness of conventional self-assembled growth. This approach combines the precision of laser processing with the atomic-level control of MBE, enabling the fabrication of nanostructure arrays with predetermined positions, enhanced size uniformity, and tailored optoelectronic properties [161, 162]. Applications of multiple-beam interference extend beyond conventional photolithography to include laser-induced periodic surface structures (LIPSS), direct laser interference patterning (DLIP), and holographic lithography in photosensitive materials [163]. These techniques enable the fabrication of complex structures with feature sizes approaching sub-100 nm dimensions, significantly below the conventional diffraction limit through careful optimization of materials and processing parameters [164, 165].

2.2.3.1. PRINCIPLE THEORY OF MULTIPLE LASER BEAM INTERFERENCE

The fundamental principle underlying direct laser patterning involves the use of focused laser radiation to create localized surface modifications that subsequently serve as preferential nucleation sites during epitaxial growth. Unlike conventional lithographic techniques that typically employ resist layers and chemical processing, direct laser

patterning minimizes surface contamination—a critical consideration for maintaining high crystal quality in MBE growth [166].

The interaction between laser radiation and semiconductor surfaces can be described through the heat diffusion equation with a source term representing laser absorption:

$$\rho C_p \frac{\partial T(r,z,t)}{\partial t} = \nabla \cdot [k \nabla T(r,z,t)] + \alpha I(r,t) e^{-\alpha z} \quad (2-12)$$

where ρ is the inferred density, C_p is the specific heat capacity, k is the thermal conductivity, α is the absorption coefficient, and $I(r,t)$ is the laser intensity distribution [167]. As a Gaussian laser beam profile shown in **Figure 2.7**, the intensity can be expressed as:

$$I(r,t) = I_0 \exp\left(-\frac{2r^2}{w_0^2}\right) f(t) \quad (2-13)$$

where I_0 is the peak intensity of the laser beam, w_0 is the beam waist radius, and $f(t)$ represents the temporal pulse shape. This theoretical framework enables the prediction of temperature evolution during laser irradiation [168], which is the key feature of controlling the type and extent location of surface modifications [169].

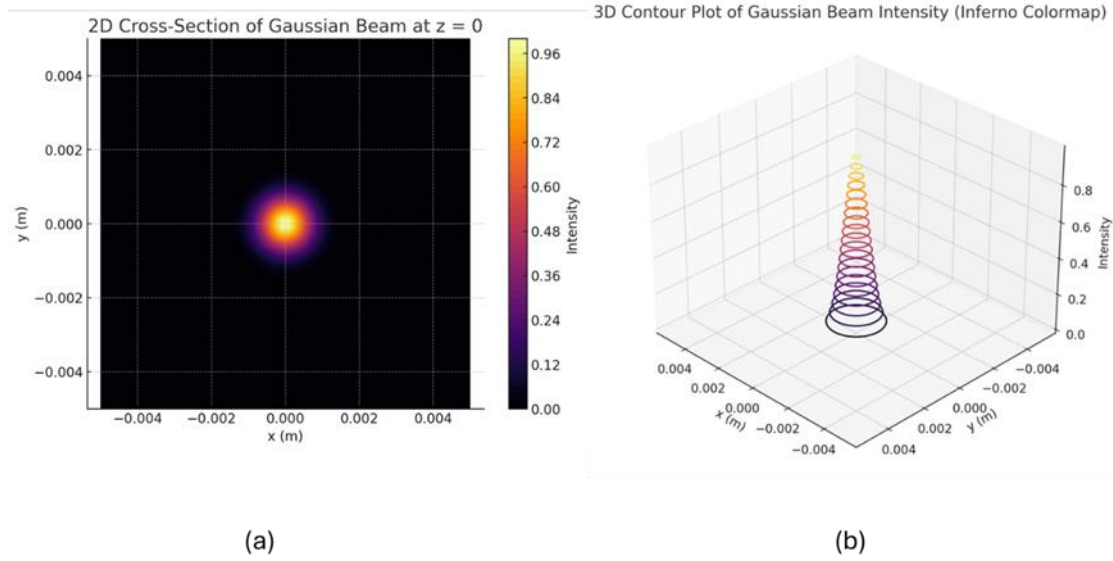


Figure 2.7 Simulated 500nm waist radius Gaussian beam intensity distribution profile of (a) 2-D view. (b) 3-D view.

The maxima temperature of the surface center for a Gaussian beam can be conducted by:

$$T_{max} \approx T_0 + \frac{2\alpha E_p}{\pi\rho C_p w_0^2} \cdot \frac{1}{\sqrt{1+4Dt_p/w_0^2}} \quad (2-14)$$

where T_0 is the initial temperature before applied the laser beam, E_p is the total energy from pulse wave, D is the thermal diffusivity, and t_p is the pulse duration[170]. This relationship provides a quantitative model for laser parameters selection to best fit the demanded surface modification requirements. However, the temperature evolution during laser irradiation leads to various surface modification mechanisms depending on the laser parameters which follows the Ficks's first law. At low fluences, thermal annealing induces surface diffusion without material removal, the diffusion coefficient of atoms D following Arrhenius equation:

$$D_s = D_0 \exp\left(-\frac{E_{des}}{k_B T_{peak}}\right) \quad (2-15)$$

where D_0 When fluence exceeds the threshold value of desorption energy (E_{des}), the dominant mechanism shifts from surface diffusion to material ablation which leads

to multiple atomic layers through phase explosion or direct vaporization when the maxima temperature approaches or exceeds the critical temperature of the surface material.

By applying the theory in the MBE chamber with UHV environment, thereby minimizing surface contamination [171]. The optical setup typically involves focusing the laser beam through a viewport onto the substrate mounted on the growth manipulator, with spatial resolution limited by:

$$d_{min} \approx 0.61 \frac{\lambda}{NA} \quad (2-16)$$

where λ is the laser wavelength and NA is the numerical aperture of the focusing system. This diffraction-limited spot size is equivalent to the patterning area.

2.2.3.2. MATHEMATICAL DERIVATION OF FOUR-BEAM INTERFERENCE SYSTEM

When multiple-beam interference stems from the superposition principle of electromagnetic waves. When multiple coherent laser beams intersect, their electric fields add vectorially, resulting in a spatially modulated intensity distribution. For a system of N laser beams, the total electric field at a point \mathbf{r} can be expressed as:

$$\mathbf{E}(\mathbf{r}, t) = \sum_{j=1}^N \mathbf{E}_j(\mathbf{r}, t) = \sum_{j=1}^N \mathbf{E}_{0j} \exp [i(\mathbf{k}_j \cdot \mathbf{r} - \omega t + \phi_j)] \quad (2-17)$$

where \mathbf{E}_{0j} represents the product of amplitude and unit polarization vector, \mathbf{k}_j is the wave vector, \mathbf{r} is the position vector, ω is the angular frequency, and ϕ_j is the initial phase of the j -th beam [172]. The resulting intensity distribution, which determines the pattern recorded in photosensitive materials, is proportional to the time-averaged square of the electric field:

$$I(\mathbf{r}) \propto \langle |\mathbf{E}(\mathbf{r}, t)|^2 \rangle_t = \sum_{j=1}^N |\mathbf{E}_{0j}|^2 + \sum_{j=1}^N \sum_{l \neq j}^N \mathbf{E}_{0j} \mathbf{E}_{0l} \cos [(\mathbf{k}_j - \mathbf{k}_l) \cdot \mathbf{r} + (\phi_j - \phi_l)] \quad (2-18)$$

This equation reveals that the interference pattern consists of a constant background term (first summation) and interference terms (second summation) that produce the spatially modulated component [173].

$$\begin{aligned} \mathbf{E}_j &= A_j [-(\cos \theta_j \cos \varphi_j \cos \psi_j - \sin \varphi_j \sin \psi_j) \cdot \mathbf{i} \\ &- (\cos \theta_j \sin \varphi_j \cos \psi_j + \cos \varphi_j \sin \psi_j) \cdot \mathbf{j} - (\sin \theta_j \cos \psi_j) \cdot \mathbf{k}] \\ \mathbf{k}_j &= k (\sin \theta_j \cos \varphi_j \cdot \mathbf{i} + \sin \theta_j \sin \varphi_j \cdot \mathbf{j} - \cos \theta_j \cdot \mathbf{k}) \\ \mathbf{r} &= x \cdot \mathbf{i} + y \cdot \mathbf{j} + z \cdot \mathbf{k} \end{aligned}$$

where $k = 2\pi/\lambda$ denotes the wave number and A_j is the amplitude of the j -th number, θ_j refers the angle of incidence, φ_j is the azimuthal angle, ψ_j is the polarisation angle.

Accordingly, four-beam configurations enable the creation of square or rectangular lattices[174]. The practical implementation of multiple-beam interference requires precise control over beam parameters[175]. Phase stability between interfering beams is particularly critical, as phase fluctuations can degrade pattern quality[176]. Active phase stabilization systems employing feedback control loops have been developed to maintain phase relationships with nanometer precision [177].

For the specific case of a $N = 3$ configuration, by assuming beams of equal intensity arranged symmetrically around the z -axis with incidence angle θ which is the angle between each beam and the substrate normal [178], the fringe pitch distance (Λ) for minimum period can be determined by:

$$\Lambda = \frac{\lambda}{2 \sin \theta} \quad (2-19)$$

where λ is the wavelength of the laser [179]. The resulting pattern can be further manipulated by controlling the polarization states of individual beams, as shown by Lai et al [157]. Beyond three beams, four-beam configurations enable the creation of square

or rectangular lattices. Wang et al. (2003) [180] demonstrated that the symmetry of the interference pattern is directly related to the geometric arrangement of the incident beams. For four beams arranged at the vertices of a square cone with the same polar angle θ , the resulting pattern displays four-fold symmetry with a period:

$$\Lambda_{four-beam} = \frac{\lambda}{2\sqrt{2} \sin \theta \sin(\pi/4)} \quad (2-20)$$

Thus, in multiple-beam laser interference, several coherent beams create complex periodic patterns. Three-beam interference produces triangular lattices, four beams generate square arrays, and six beams create hexagonal patterns. While other parameters affect contrast and fine features, incident angle fundamentally controls spatial frequency—essential for applications requiring specific lattice constants for targeted optical or electronic properties.

2.2.3.3. SIMULATION OF MULTIPLE-BEAM INTERFERENCE PATTERNING

By applying the theoretical model of multi-beam interference pattern into python code, investigation of various beam parameters influence interference patterns in multiple-beam laser interference can be conducted. In this thesis, all simulations employed a 355 nm laser wavelength with equal beam amplitudes and zero initial phases as baseline conditions. The schematic of the four-beam spatial illumination shows in **Figure 2.8**.

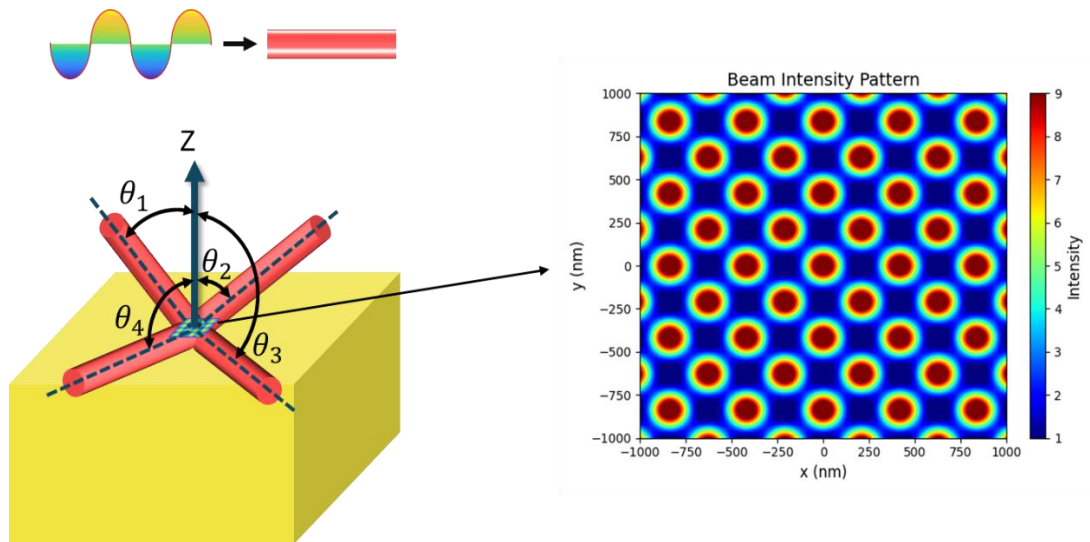


Figure 2.8 Illumination of four-beam interference configuration at an incident angle of θ and equivalent azimuth angle with an example of simulated intensity distribution map shown on the right.

From the mathematical derivation in **Chapter 2.2.3.2**, the number of interfering beams fundamentally determines the symmetry and complexity of the resulting patterns. Two-beam interference produces simple one-dimensional periodic fringes, while three-, four-, and six-beam configurations generate two-dimensional arrays with circular, square, and hexagonal symmetries, respectively. More complex and exotic patterns emerge when using five, seven, or more beams. In all simulations, the beams were arranged symmetrically with identical 30° incidence angles and transverse magnetic (TM) polarization (0° polarization angle) shows in **Figure 2.9**. The three-beam and four-beam pattern has presented the highest potential for 2-D ordered arrays of structures.

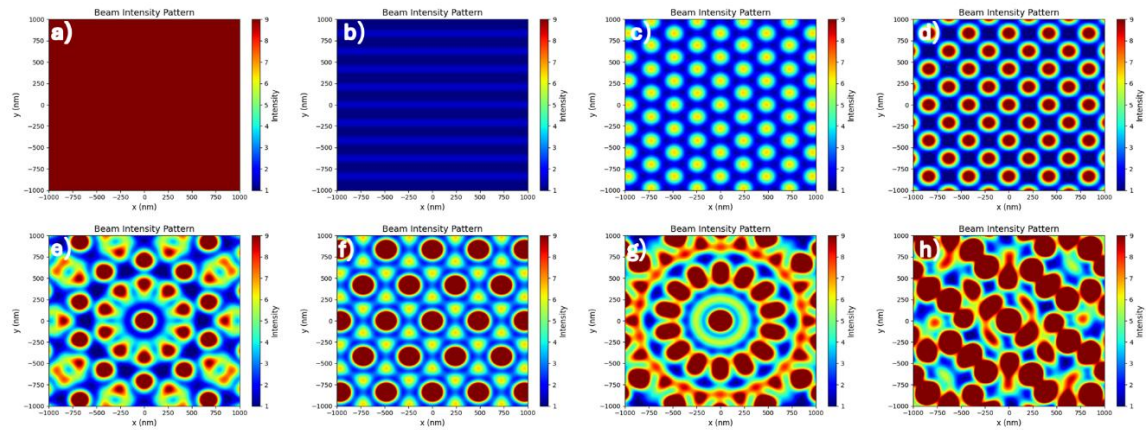


Figure 2.9 Simulated interference laser intensity distribution of 58° incident angle and 0° polarization angle with (a) 1 beam. (b) 2 beams. (c) 3 beams. (d) 4 beams. (e) 5 beams. (f) 6 beams. (g) 7 beams. (h) 8 beams.

This research primarily focused on four-beam interference with beams positioned at azimuthal angles of 0° , 90° , 180° , and 270° to generate square arrays of surface features. The incidence angle proved to be the dominant parameter controlling the pattern's lattice pitch (periodicity). At 355 nm wavelength with 60° incidence angle, the lattice pitch measured approximately 290 nm with TM polarization but decreased to approximately 205 nm when using transverse electric (TE) polarization (90° polarization angle).

Another key feature for the DLIP technique is the polarization angle which shows in **Figure 2.10**, Polarization states significantly influence both the geometric shape and contrast of the interference patterns. At 60° incidence, TM-mode polarization (all beams at 0° polarization angle) delivered superior pattern contrast compared to other polarization configurations. This demonstrates how polarization manipulation allows fine-tuning of pattern characteristics without altering the basic periodicity determined by the incidence angle.

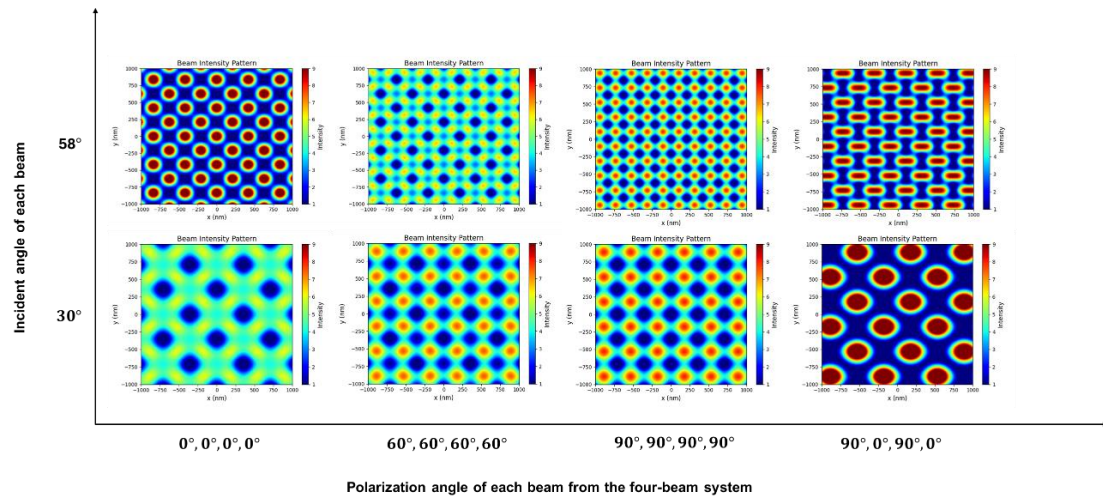


Figure 2.10 Simulation of four-beam interference intensity patterns using various combinations of incidence and polarization angles.

These simulation results demonstrate how multiple-beam interference offers extensive control over surface pattern characteristics through parameter adjustment. By manipulating the number of beams, incidence angles, polarization states, and maintaining uniform beam intensities, researchers can precisely engineer periodic nanostructures with tailored symmetries, periodicities, and feature shapes for various advanced applications in photonics, plasmonic, and surface engineering.

2.3.SUMMARY

The epitaxial growth techniques for III-V semiconductor nanostructure arrays have been demonstrated in this chapter. MBE enables precise atomic-layer deposition under ultra-high vacuum conditions, producing high-purity epitaxial layers with controlled surface processes. Three fundamental growth modes—Frank-van der Merwe (layer-by-layer), Volmer-Weber (island formation), and Stranski-Krastanov (layer-plus-island)—have been identified, each determined by the balance of surface free energies and kinetic processes.

The chapter presents three principal methods for fabricating ordered nanostructure arrays: Stranski-Krastanov growth, Droplet Epitaxy, and Direct Laser Interference Patterning. The SK mode relies on lattice mismatch to induce strain-driven formation of three-dimensional islands after initial wetting layer growth. Growth parameters such as temperature, deposition rate, and wetting layer thickness significantly influence the size, density, and uniformity of the resulting quantum dots.

Droplet Epitaxy employs a two-step process involving initial metal droplet formation followed by crystallization through exposure to group V elements. This technique overcomes the lattice mismatch limitations of SK growth and enables diverse nanostructure geometries including quantum rings and disks. Crystallization kinetics can be precisely controlled by modifying growth parameters, though challenges remain in achieving uniform droplet size distribution.

DLIP creates precisely positioned nucleation sites through multiple coherent laser beams. Simulations demonstrate that interference patterns with different symmetries can be achieved by adjusting beam parameters. Four-beam configurations produce square arrays with periodicities determined by incident angle and polarization states.

The surface modification mechanisms during epitaxial growth follow temperature-dependent kinetics, with diffusion coefficients exhibiting Arrhenius behavior. The results presented demonstrate that MBE-based epitaxy provides excellent potential for creating high-quality semiconductor nanostructure arrays with precisely controlled dimensions and properties.

3. EXPERIMENTAL AND CHARACTERISTICS

METHODS

This chapter covers the MBE process used to grow all the samples discussed in this thesis, along with the characterization methods applied to them. It begins with an overview of MBE and its key features, followed by a description of structural characterization techniques such as AFM and TEM. Finally, it explains the principles and applications of optical characterization through photoluminescence (PL) measurements.

3.1. Molecular Beam Epitaxy System

Molecular Beam Epitaxy (MBE) represents a sophisticated epitaxial growth technique predicated on the interaction between atomic or molecular beam fluxes and heated substrate surfaces within an ultra-high vacuum (UHV) environment, typically maintained at pressures ranging from 10^{-8} to 10^{-12} mbar. Unlike conventional deposition methodologies, MBE facilitates exceptionally precise control over beam flux parameters and growth conditions, while simultaneously achieving remarkably low deposition rates—approximately 1 monolayer per second (1ML/s)—which contributes significantly to the technique's capacity for growing films with exacting thickness specifications, superior purity, and minimal crystallographic defects [128, 181].

3.1.1. FUNDAMENTALS OF MBE SYSTEMS

The standard solid-source MBE apparatus comprises a hierarchical arrangement of chambers, each serving distinct functions within the growth process as **Figure 3.1** shown. The primary growth chamber houses multiple effusion cells that generate the requisite atomic or molecular beam fluxes directed toward the substrate surface. For III-V semiconductor growth, elemental sources including gallium, indium, and aluminium (Group III), as well as phosphorus, arsenic, and antimony (Group V) are employed, with additional dopant cells containing silicon (n-type) and beryllium (p-type) to facilitate controlled doping profiles [182]. The buffer and load lock chambers, separated by precision gate valves, maintain the integrity of the UHV environment during substrate introduction and preparation procedures. **Figure 3.1** provides a schematic representation of a typical solid-source MBE growth chamber, illustrating the spatial configuration of critical components including effusion cells, substrate manipulator, and monitoring equipment. MBE is based on the physical vapor deposition (PVD) technique, in which atomic or molecular beams are thermally evaporated from effusion cells and directed toward a heated substrate. The interaction of these beams with the substrate under UHV conditions leads to epitaxial growth, where the deposited material aligns itself with the crystalline lattice of the substrate. The key stages of MBE growth include the adsorption of atoms on the substrate surface, surface diffusion to energetically favorable sites, and incorporation into the growing lattice.

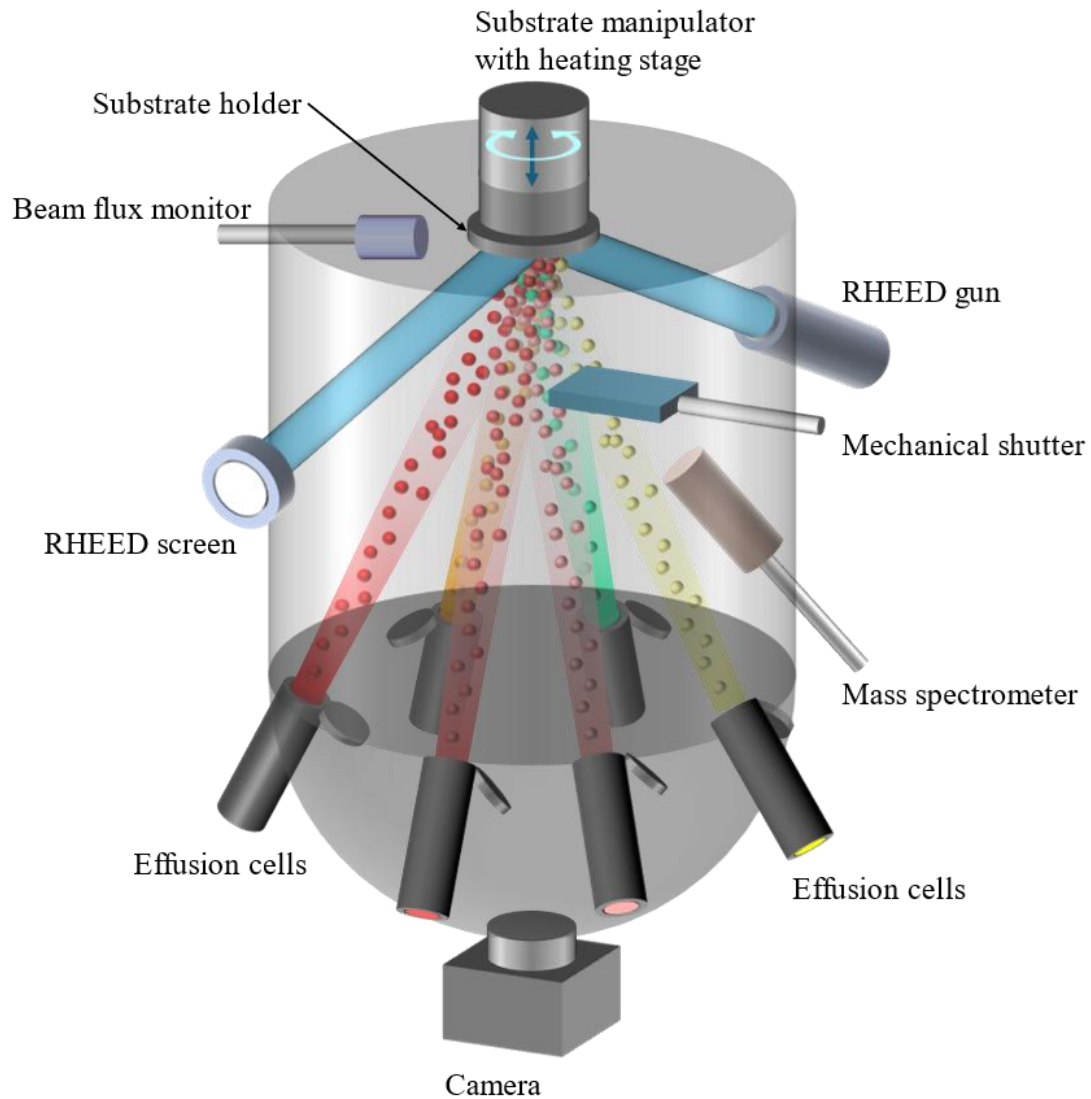


Figure 3.1 Illustration of a typical solid-source MBE growth chamber.

The monitoring infrastructure integrated within the MBE system enables comprehensive in situ characterization of growth dynamics. Reflection High Energy Electron Diffraction (RHEED) constitutes a particularly valuable analytical tool, whereby high-energy electrons incident at a grazing angle ($1\text{-}2^\circ$) are diffracted from surface atoms and subsequently detected on a phosphor-coated screen. The resulting diffraction patterns provide real-time information regarding surface morphology, roughness, reconstruction states, and—through analysis of intensity oscillations—growth rates [131, 183]. Complementary monitoring systems include beam flux

monitors for precise quantification of beam equivalent pressures and thermocouples for accurate temperature measurement at effusion cell crucibles.

Several critical process parameters fundamentally influence the quality of epitaxial growth. Substrate temperature represents a paramount variable, governing the desorption behavior of Group III atoms—with characteristic desorption temperatures of approximately 500°C for indium, 620°C for gallium, and 1000°C for aluminium—while simultaneously affecting the migration length of surface atoms and, consequently, surface morphology and optical properties of resultant nanostructures [184, 185]. The

Group V/III flux ratio constitutes another crucial parameter, with typical beam equivalent ratios ranging from 15 to 25 for GaAs-based materials. The requirement for excess Group V atoms arises from their relatively lower sticking coefficients compared to Group III species, necessitating higher partial pressures to ensure stoichiometric incorporation [186]. Additionally, deposition rate exerts significant influence on surface morphology, with lower rates generally facilitating improved adatom mobility and, consequently, enhanced crystalline quality [187]. The experimental methodology employed in this dissertation for GaAs sample preparation adhered to a rigorous protocol optimized for high-quality epitaxial growth. Epi-ready two-inch wafers or quarter wafers were initially introduced into the load lock chamber and evacuated to a pressure of 1×10^{-8} mbar using a turbomolecular pump. Subsequently, wafers underwent thermal degassing in the buffer chamber at 300°C for a minimum duration of 30 minutes to eliminate surface contaminants. Following transfer to the main chamber, the substrate temperature was elevated to approximately 650°C to facilitate desorption of native oxide from the GaAs surface, with arsenic flux maintained at substrate temperatures exceeding 400°C to prevent dissociative loss of arsenic from the substrate. The growth process commenced with the deposition of a GaAs buffer layer,

servicing to planarize the interface and encapsulate potential interfacial contaminants. Confirmation of epitaxial quality was achieved through observation of pronounced surface reconstruction features in the RHEED pattern, indicative of atomically smooth surfaces with well-defined crystallographic ordering [188].

3.1.2. THE MBE SYSTEM WITH DIRECT LASER INTERFERENCE PATTERNING SET-UP

A specialized solid-source MBE system, manufactured by Dr. Eberl MBE-Komponenten GmbH of Germany, was utilized for the growth of III-V semiconductor materials in this research, as **Figure 3.2** shows.

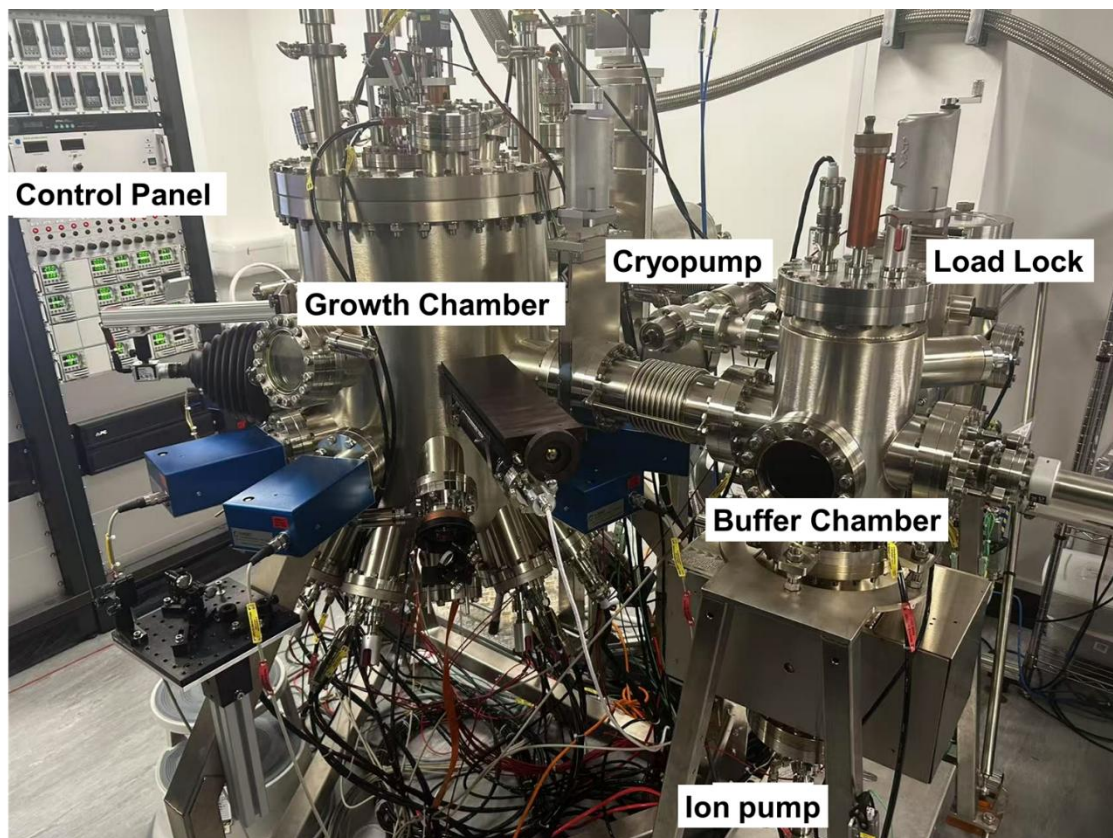


Figure 3.2 Photograph of the modified MBE system which provided by Dr. Eberl MBE-Komponenten® GmbH (Germany).

The system's architecture consists of three interconnected chambers: the growth chamber (also called the main chamber), the buffer chamber, and the load lock chamber. These chambers are physically isolated from each other by gate valves to maintain appropriate vacuum conditions in each section.

The growth chamber houses a comprehensive array of material sources necessary for III-V semiconductor fabrication. From Group III elements, the system incorporates indium (In), aluminum (Al), and gallium (Ga) effusion cells. For controlled doping capabilities, silicon (Si) cells provide n-type doping while beryllium (Be) cells enable p-type doping. Group V elements are supplied through arsenic (As) and antimony (Sb) valved-cracker cells, which offer precise control over gas-phase delivery of these volatile elements.

To achieve the ultra-high vacuum necessary for high-quality epitaxial growth, the system employs a sophisticated pumping arrangement combining a cryopump with a titanium sublimation pump. This configuration achieves base pressures significantly below 10^{-10} mbar, creating an extremely clean environment for crystal growth.

Each material source is equipped with a computer-controlled shutter positioned directly in front of the cell, allowing for precise interruption of molecular beam fluxes during growth sequences. Temperature monitoring of each effusion cell is accomplished through thermocouples in direct contact with the crucibles containing source materials. To quantify the molecular flux during calibration and growth, a specialized beam flux monitor—an unshielded Bayard-Alpert ionization gauge—can be positioned directly beneath the substrate.

The sample preparation protocol for all GaAs substrates in this dissertation followed a standardized procedure. Epi-ready two-inch wafers or quarter wafers were initially loaded into the load lock chamber and pumped down to approximately 1×10^{-8}

mbar using a turbo pump. Following this initial evacuation, the wafers were transferred via a mechanical transfer rod into the buffer chamber, where they underwent a thorough degassing process on a heated stage maintained at 300°C for a minimum of thirty minutes.

After degassing, the substrates were moved into the growth chamber, where the temperature was gradually increased to approximately 650°C to thermally remove the native oxide layer from the GaAs surface. Throughout the heating process at temperatures exceeding 400°C, a controlled arsenic flux was continuously supplied to prevent dissociation of the GaAs substrate, thereby maintaining the crystal structure integrity in preparation for subsequent epitaxial growth.

3.1.2.1. MODIFICATION ON MBE

Since the MBE operates as a large vacuum chamber incompatible with internal optical components, a custom external laser system has been designed to DLIP application. The laser source is positioned on an optical table adjacent to the MBE chamber, with optical components distributed across three sub-optical breadboards installed around the system perimeter.

The optical path begins with beam redirection to an optical sub-frame via a steering mirror. A periscope assembly aligns the laser beam height with the MBE optical viewports. Three 50:50 beam splitters divide the primary beam into four sub-beams, which are then directed into the MBE chamber through symmetrically positioned UV anti-reflection coated viewports at 0°, 90°, 180°, and 270°. Each beam enters at a 58° incident angle to the substrate—fixed by the welded viewport positions. The complete optical path spans approximately 3.5-4 meters. **Figure 3.3** (a-c) show photographs of selected optical components surrounding the MBE chamber.

Precise beam alignment is achieved using an upward-facing CMOS camera positioned at a surface-normal viewport. This procedure requires loading a 2-inch InGaN wafer compatible with MBE conditions into the chamber. The InGaN wafer absorbs UV light and emits blue luminescence detectable by the camera, which is otherwise insensitive to scattered 355 nm light. **Figure 3.3** (d) displays a camera capture showing all four sub-beams successfully aligned at the center of an InGaN wafer.

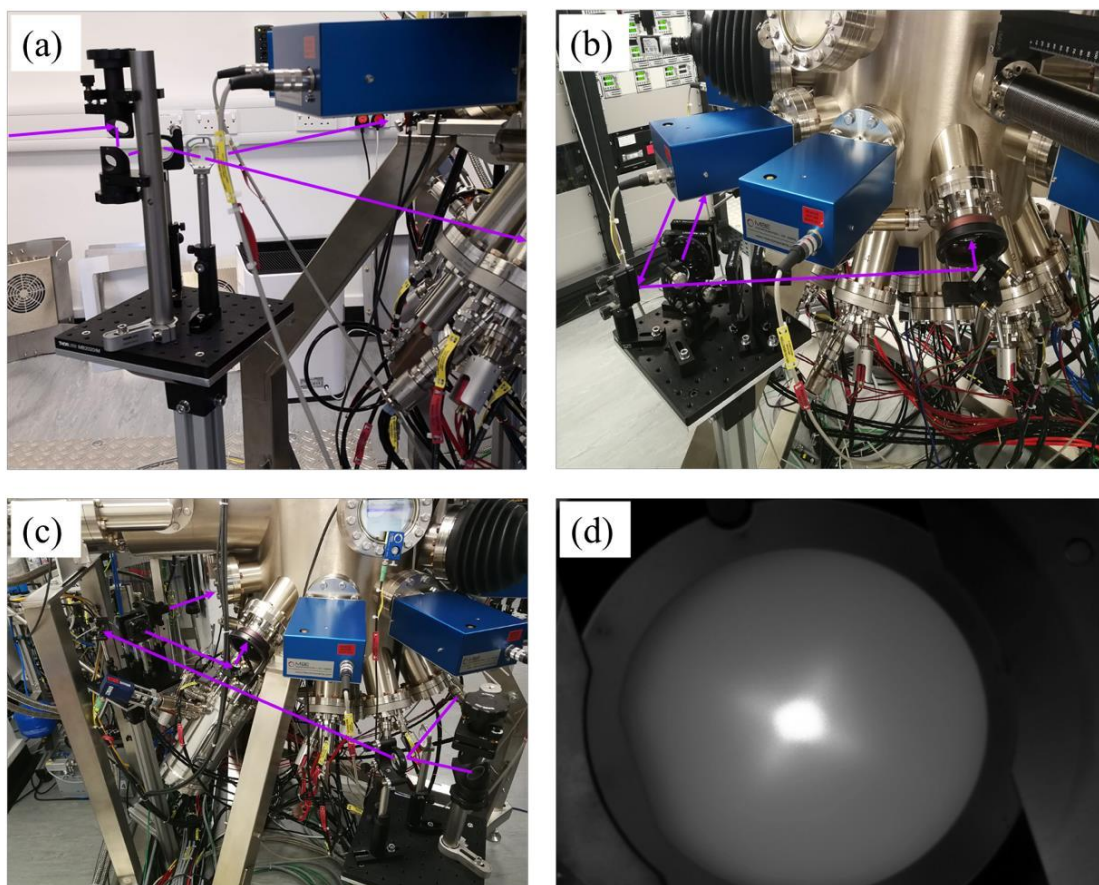


Figure 3.3 (a–c) Photos showing parts of the DLIP setup surrounding the MBE chamber. (d) Camera image of four laser beams focused at the center of an InGaN wafer.

3.1.2.2. OVERVIEW OF THE DLIP-MBE SYSTEM

The radiation source used was a flash-lamp pumped Neodymium-doped yttrium aluminum garnet (Nd: YAG) laser (InnoLas SpitLight 1000) operating at $\lambda = 355$ nm, as **Figure 3.4** shows. This system generates a fundamental infrared beam at 1064 nm through a flashlamp-pumped Nd: YAG rod. Harmonic generation crystals convert this to outputs at 532 nm (second harmonic), 355 nm (third harmonic), and 266 nm (fourth harmonic).

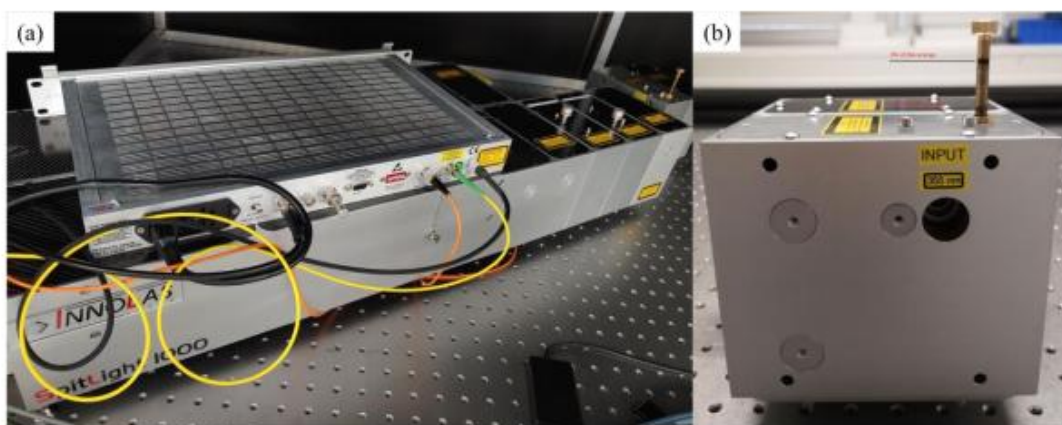


Figure 3.4 Photographs of (a) the Nd: YAG laser with a seeder. (b) The attenuator.

To enhance output laser bandwidth and spatial profile, a temperature-stabilized single-mode semiconductor fiber laser was implemented as an injection seeder. High laser energy was achieved through Q-switching using a Pockels cell electro-optic device. For precise single pulse exposure, an external shutter extracted individual pulses from the 5 Hz laser repetition rate, timed according to the laser Pockels cell trigger signal.

The full schematic of the specialized four-beam DLIP setup was integrated with MBE system for in-situ growth of semiconductor nanostructures as **Figure 3.5** shows.

the 355nm laser beam is first elevated by a periscope assembly before being divided into four identical sub-beams using three 50:50 UV beam splitters (BS1-3). These four sub-beams are then reflected by UV mirrors positioned at azimuthal angles of 0° , 90° , 180° , and 270° , converging at the center of a 2-inch sample surface with a 58° incidence angle.

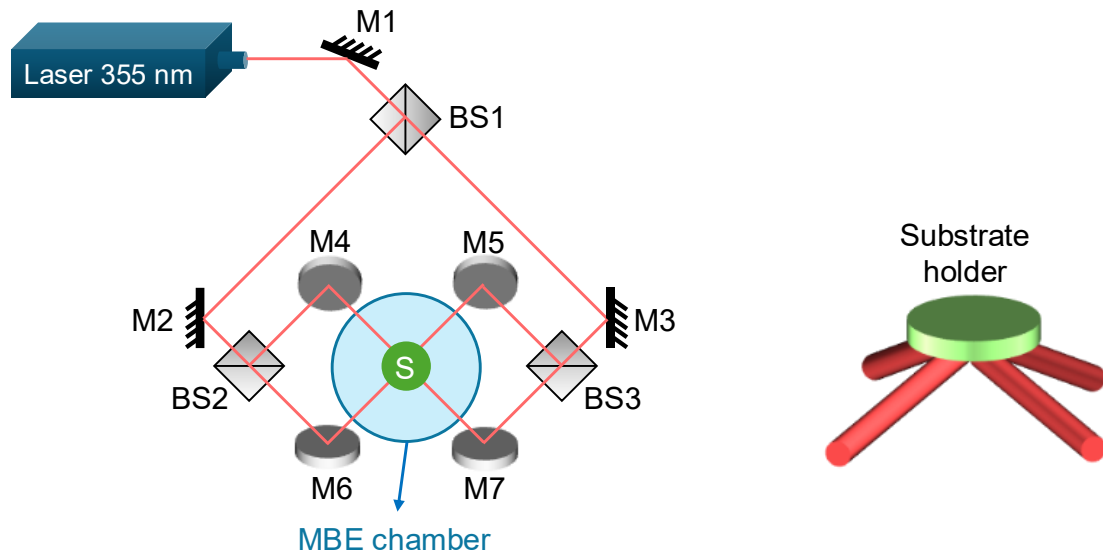


Figure 3.5 General layout of the four-beam DLIP configuration for MBE growth. BS1- BS3: 50:50 beam splitters, M1-M7: high reflective UV mirrors and S for the substrate holder.

Each beam path incorporates a half-wave plate and Glan-laser polarizer to control pulse energy and polarization states. The polarizer determines the target polarization angle, while the half-wave plate enables adjustment to any arbitrary polarization plane through rotation. Beam alignment is facilitated by a downward-facing CMOS camera.

To address challenges from the large incidence angle (which creates elliptical beam spots and complicates alignment), a beam shaping system is implemented before BS1. This system uses two cylindrical lenses—a plano-concave ($f = -100\text{mm}$) and a plano-convex ($f = 200\text{mm}$)—to achieve $2 \times$ horizontal magnification. This pre-compensates for spot distortion caused by non-perpendicular incidence.

Without beam shaping, the four elliptical beams cannot completely overlap even when properly aligned, creating large areas with undesired two-beam interference. The beam shaping system converts the initial laser beam into an elliptical shape that, when projected at the 58° angle, produces a round beam profile which shown look like a bright round spot in **Figure 3.3** (d). This enables larger overlap areas and creates uniform large-area multi-beam interference patterns.

3.2. Atomic Force Spectroscopy

Atomic Force Microscopy (AFM) is a sophisticated surface analytical technique that generates three-dimensional topographical images of solid materials with nanometer resolution. This method works by detecting minute atomic forces between a tiny probe and the sample surface.

The core AFM structure consists of a sharp tip (less than 10nm in diameter) attached to a microcantilever, typically made of silicon or silicon nitride, across a sample surface to detect forces between the tip and the surface at the atomic scale. The horizontal resolution depends on the tip's radius of curvature, typically 5-7nm in our implementation. As the probe encounters surface variations, the cantilever deflects according to Hooke's law. A laser beam directed at the cantilever's back reflects and shifts position with these deflections. By tracking these changes through a position-sensitive photodetector, the system collects detailed surface information.

AFM operates in three main scanning modes known as Non-contact mode: Non-contact mode involves the cantilever oscillating 5-10nm above the sample, with interactions governed by Van der Waals forces. This approach preserves both sample and tip from damage but performs best in ultra-high vacuum conditions since ambient environments cause water layer absorption on samples, interfering with measurements.

In contact mode, the tip maintains continuous contact with the sample surface, generating repulsive forces. The pressure applied during scanning may alter the sample's morphology, making this unsuitable for delicate specimens.

Tapping mode serves as an intermediate approach and is most used for semiconductor imaging. The cantilever oscillates at a preset resonant frequency, detecting surface features through phase shifts in oscillation. The tip makes only periodic, gentle contact with the sample, making this ideal for examining delicate materials. Tapping mode better handles the water layer present in ambient conditions, enhancing effectiveness in standard laboratory environments.

AFM is particularly valuable for characterizing semiconductor nanostructures, especially quantum dots. The technique provides critical measurements of diameter, height, shape, density, and rough surface. In our research, we used a tapping mode AFM system (FSM NanoView-1000) operating in air to analyze our fabricated samples as **Figure 3.6** shows. Our silicon AFM probes featured tip radii under 10nm, lengths of 100 μ m, and resonance frequencies of approximately 300kHz. All analyses were conducted using Gwydion and WSxM software packages.

AFM's non-destructive nature and high-resolution capabilities make it essential for advanced materials research, particularly in semiconductor development where nanoscale surface characteristics significantly influence device performance. By providing detailed structural information at the nanometer scale, AFM enables researchers to optimize fabrication processes and understand the fundamental relationships between structural properties and functional performance of semiconductor devices

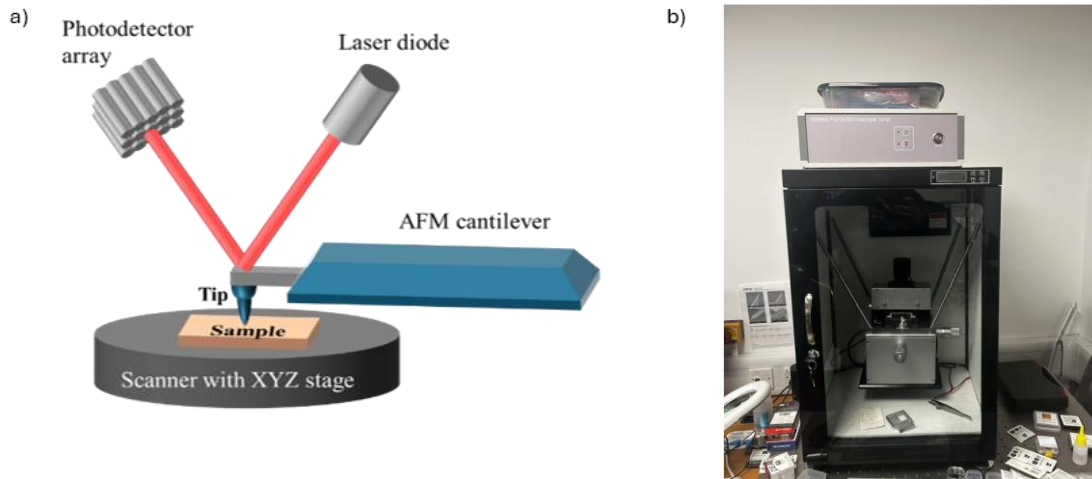


Figure 3.6 (a) Diagrammatic illustration of the principle of AFM. (b) Photograph of an AFM instrument.

3.3. Photoluminescence Spectroscopy

Photoluminescence (PL) measurement is a powerful and non-destructive optical technique used to study the electronic and optical properties of materials, especially semiconductors, nanostructures, and thin films. The following parts introduce the principle of the photoluminescence spectroscopy first. Then the details and theory of comprehensive Micro-PL measurements system for both temperature dependent and power dependent application used for all the PL spectra in this thesis are explained.

3.3.1. PRINCIPLE OF PHOTOLUMINESCENCE SPECTROSCOPY

This technique involves the excitation of a material using a light source, leading to the emission of light (photoluminescence) because of electron-hole recombination. The emitted light provides information about the material's bandgap, defect states, carrier dynamics, and quantum efficiency. Due to its versatility and sensitivity, photoluminescence measurement has found widespread applications in materials science, photonics, and quantum technologies. This review delves into the principles

underlying photoluminescence, the factors influencing its measurement, and its applications in characterizing materials.

Figure 3.7 illustrates the fundamental difference between recombination processes in direct and indirect bandgap semiconductors. In direct bandgap semiconductors (**Figure 3.7 (a)**), electrons in the conduction band (cb) can recombine directly with holes in the valence band (vb) because the minimum of the conduction band aligns with the maximum of the valence band in k-space (momentum space). This direct transition releases energy as a photon ($h\nu$) with energy equal to the bandgap energy (E_B), resulting in efficient radiative recombination. In contrast, indirect bandgap semiconductors (**Figure 3.7 (b)**) have their conduction band minimum and valence band maximum offset in k-space. For electron-hole recombination to occur, conservation of both energy and momentum is required. Once photons carry negligible momentum, a third particle—a phonon—must be generated in the process. This phonon-assisted transition involves the electron simultaneously emitting (or absorbing) a phonon to change its momentum while emitting a photon during recombination with a hole.

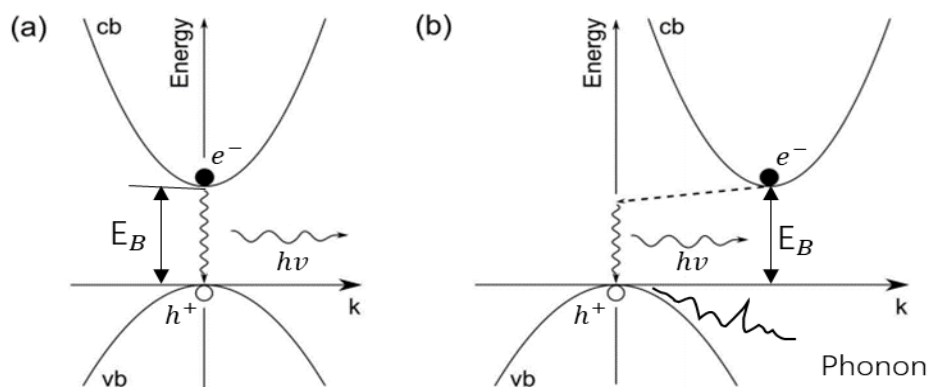


Figure 3.7 Schematic band diagram of interband transitions in bulk semiconductors. (a) Band edge recombination in a direct bandgap

semiconductor. (b) Indirect, phonon assisted recombination in an indirect bandgap semiconductor.

This three-particle process (electron, hole, and phonon) in indirect semiconductors occurs with significantly lower probability than direct recombination, resulting in longer carrier lifetimes and reduced radiative efficiency. This fundamental difference explains why direct bandgap materials like GaAs are preferred for light-emitting applications, while indirect bandgap semiconductors like silicon are less efficient light emitters. As photoluminescence is conducted as the emission of light from material following the absorption of photons. The process involves three key steps: photon absorption, excitation of electrons, and radiative recombination.

When a material absorbs photons with energy equal to or greater than its bandgap energy, electrons in the valence band (VB) are excited to the conduction band (CB), leaving behind holes in the VB which reveals in **Figure 3.8**. This creates electron-hole pairs, also known as excitons, in the material. The energy of the absorbed photon must be greater than or equal to the electronic transitions allowed in the material, which could include band-to-band transitions, defect states, or quantum confinement levels.

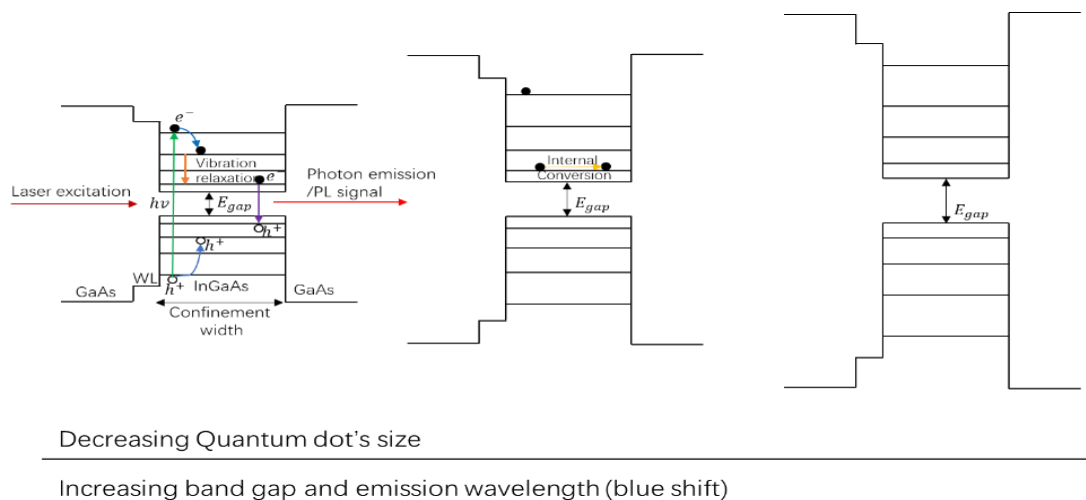


Figure 3.8 Schematic band diagram via different size InGaAs/GaAs QDs.

After the excitation stage, the electrons in the CB and holes in the VB can relax to lower-energy states through non-radiative processes, such as phonon scattering, or radiative processes, which involve the emission of photons. The relaxation mechanisms and rates are determined by the material's electronic structure, defect density, and temperature.

Then radiative recombination occurs when an electron recombines with a hole, emitting a photon. The energy of the emitted photon corresponds to the energy difference between the recombination states. In semiconductors, this is often the bandgap energy or transitions involving defect states or impurities. The emitted light provides crucial information about the energy levels in the material.

The intensity, wavelength, and spectral features of the emitted light are detected and analysed in a photoluminescence measurement system, providing insights into the optical and electronic properties of the material.

In conclusion, several factors significantly influence photoluminescence (PL) spectroscopy measurements in semiconductor materials. Defects and impurities introduce localized states within the bandgap that can trap carriers and modify radiative recombination pathways, enabling PL to serve as a diagnostic tool for identifying these states through characteristic sub-bandgap emission peaks. Temperature plays a critical role in PL analysis, with low-temperature measurements offering sharper emission peaks and enhanced spectral resolution due to suppressed thermal excitation, while elevated temperatures activate non-radiative recombination channels that diminish overall PL intensity. In quantum-confined structures such as quantum wells and dots, the spatial restriction of carriers results in quantized energy levels, which PL can effectively characterize through systematic observation of emission energy shifts corresponding to dimensional variations. The excitation intensity fundamentally affects

carrier generation rates, with low power densities typically yielding spectra dominated by radiative recombination processes, while higher intensities may introduce complex nonlinear effects and saturation phenomena that alter the spectral characteristics and relative peak intensities.

3.3.2. Micro-Photoluminescence Spectroscopy (μ -PL)

Micro-photoluminescence (μ -PL) spectroscopy represents a critical advancement in the optical characterization of quantum dot (QD) heterostructures, enabling spatially resolved investigations at micrometer and sub-micrometer scales.[189] Unlike conventional PL techniques that average signals over larger sample areas, μ -PL provides the spatial resolution necessary to examine individual QDs or small QD ensembles, thereby revealing critical information about local optical properties that would otherwise be obscured in ensemble measurements [190]. The fundamental principle of μ -PL involves focusing an excitation laser beam to a diffraction-limited spot (typically 1-2 μm) on the sample surface using high numerical aperture microscope objectives which as the **Figure 3.9**. The subsequent luminescence is collected through the same objective, spectrally dispersed, and detected with high sensitivity. This approach enables investigation of single QD emission characteristics, including exciton fine structure, linewidth broadening mechanisms, and spectral diffusion effects that are

essential for understanding quantum confinement phenomena at the nanoscale [191, 192].

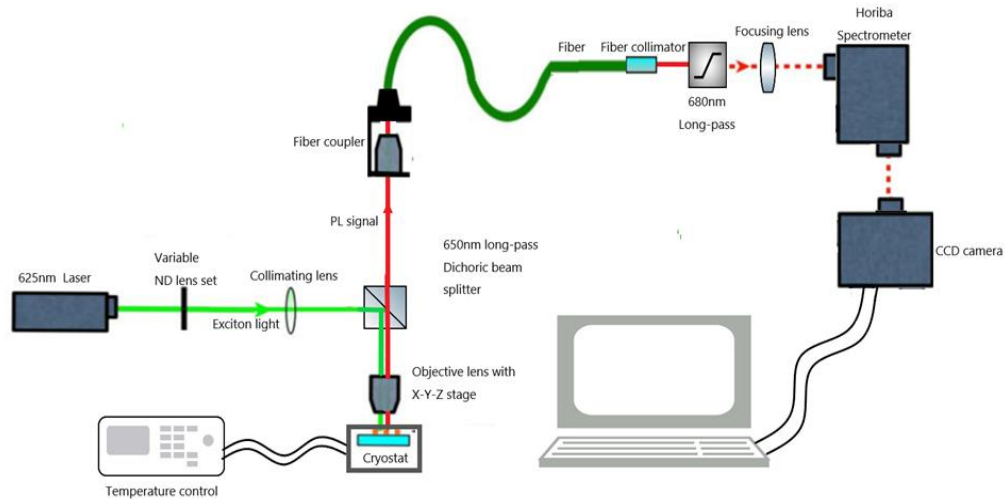


Figure 3.9 Schematic diagram of a typical μ -PL setup the excitation path (green), collection path (red), and cryogenic sample stage with nanopositioning capabilities. Essential components include the excitation laser, beam conditioning optics, high-NA objective, spectrometer, and detector array.

For self-assembled QDs that exhibit inherent inhomogeneities in size, composition, and strain distribution, μ -PL enables direct correlation between spatial positions and spectral variations. Modern systems typically employ either cold-finger cryostats or specialized objective-compatible flow cryostats for low-temperature measurements (4-10K), which significantly enhance spectral resolution by reducing homogeneous broadening effects. The advancement of μ -PL techniques continues to expand our understanding of QD optical characteristics, driving the development of quantum photonic devices including single-photon sources, quantum bit operations, and entangled photon pair generation for quantum information technologies [115] [193].

3.3.2.1. Temperature Dependence

Temperature-dependent μ -PL studies, typically conducted from 4K to 300K, probe thermal activation energies and non-radiative recombination pathways crucial for room-temperature applications. As temperature increases, characteristic redshifts in emission energies occur due to bandgap narrowing, while spectral broadening reveals the role of phonon coupling. The integrated PL intensity typically follows an Arrhenius-type behavior, enabling extraction of activation energies associated with carrier escape mechanisms [194].

The thermal quenching of luminescence intensity provides direct evidence of carrier delocalization processes, particularly important in QD ensembles with inhomogeneous size distributions. Furthermore, temperature-dependent linewidth analysis reveals the contribution of homogeneous broadening mechanisms, with low-temperature measurements minimizing phonon scattering effects and enhancing spectral resolution [195].

Combined power and temperature studies enable comprehensive mapping of QD electronic structure, including level spacing, binding energies, and capture/escape dynamics. These measurements are particularly valuable for engineering QD-based devices operating across various temperature regimes, from cryogenic single-photon sources to room-temperature lasers [196].

3.3.2.2. Excitation Power Dependence

Power-dependent μ -PL investigations involve systematic variation of excitation power density, typically spanning several orders of magnitude (10^{-2} to 10^3 W/cm²). At low excitation powers, emission is dominated by ground-state exciton recombination,

characterized by narrow linewidths and distinct single-exciton peaks. As excitation power increases, spectral features evolve to include biexciton and charged exciton (Trion) states, identifiable through their super linear and sublinear power dependencies, respectively [197]. The saturation behavior of individual emission lines provides critical information about capture cross-sections and oscillator strengths. Moreover, power-dependent measurements can reveal many-body interactions including state-filling effects and Coulomb interactions between carriers that manifest as energy shifts in emission lines [198].

3.3.2.3. The experimental set-up of the μ -PL system

The μ -PL system used for all PL spectrum revealed in this thesis shows in **Figure 3.10**. The main components of the system include excitation source, the Nanopositioner platform with fixed optical objective lens, sample stage with cryostat and the spectrum data acquisition devices. In this work, several lasers were used for different sample materials, including both continuous wave (CW) and pulsed lasers. The continuous wave lasers, all manufactured by Coherent, provide adjustable output power between 1-20mW at wavelengths of 495nm, 580nm, 625nm, and 780nm. The 1045nm High-Q 2 (Spectra-Physics) pulsed laser with 63MHz repetition rate with a maximum output of 2W.

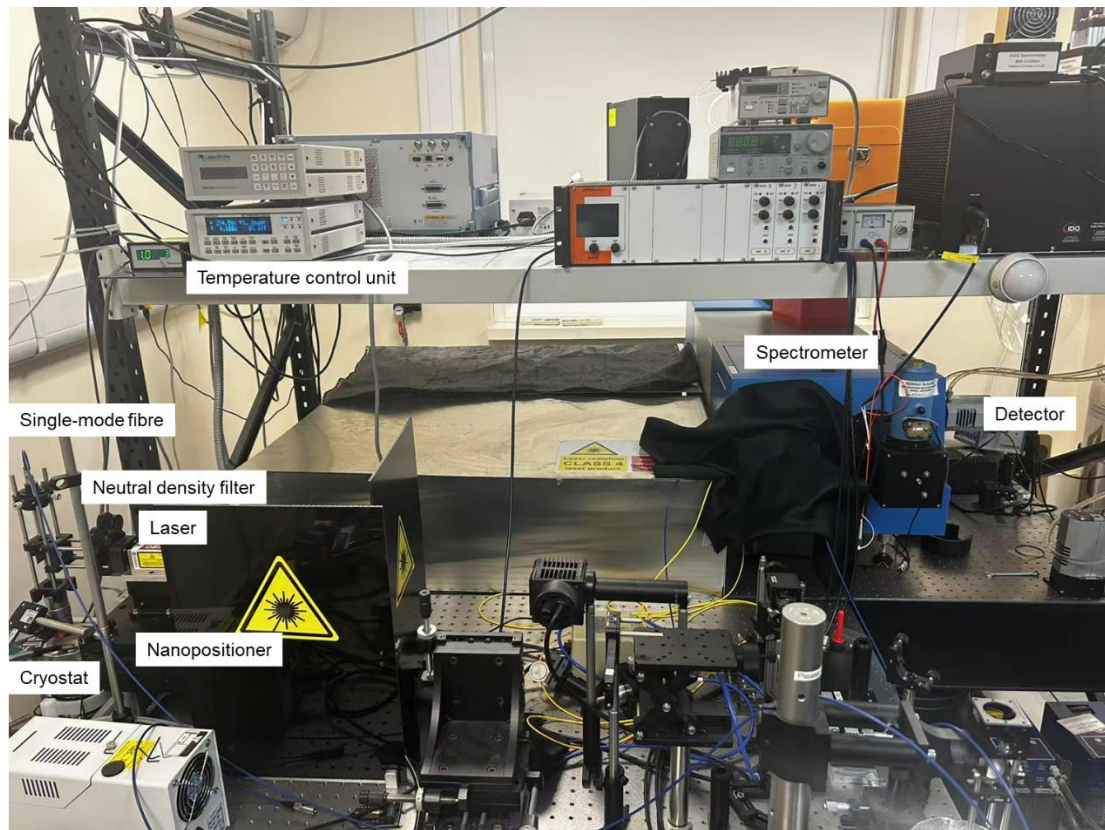


Figure 3.10 Photo of the key components of the μ -PL system used in this thesis.

The 3-axis Nanopositioner platform (Standa & XIMC) provides $\pm 6000 \mu\text{m}$ in x-y direction and $\pm 1500 \mu\text{m}$ in z direction. For the x-y direction movement controlled by the dual-axis controller, the minimum movement step length in x-y direction is 25nm. The z-axis controller has provided a better step length of 20nm. The nanometer scale movement of the Nanopositioner enables potential of precise spatial PL spectrum acquisition.

The sample stage with integrated cryostat can cool samples to 14K. The temperature is regulated by a Model 331 temperature controller (Lakeshore) with an operational range between 10K-300K, enabling temperature-dependent measurements.

For PL spectrum data acquisition, the system employs two primary components: an FHR 1000 (HORIBA) spectrometer and iDus series detectors (Andor). The FHR 1000 spectrometer provides a spectral resolution of 0.008nm per 10 μm slit width and a

scanning range of 0-1500nm. The iDus detectors from Andor used for PL measurements include a silicon-based detector for the 600-900nm range and an InGaAs-based detector for the 900-1300nm range.

3.3.3. Time-Resolved PL

Time-resolved photoluminescence (TRPL) spectroscopy represents an essential technique for investigating carrier dynamics in semiconductor quantum dots (QDs), providing direct access to recombination lifetimes, relaxation pathways, and energy transfer mechanisms occurring at timescales ranging from picoseconds to microseconds. Unlike steady-state measurements, TRPL reveals the temporal evolution of optical transitions, offering critical insights into fundamental processes that govern QD optoelectronic behavior [199].

The fundamental principle of TRPL involves exciting the sample with an ultrashort laser pulse and recording the subsequent luminescence decay as a function of time. Modern TRPL systems typically employ either time-correlated single-photon counting (TCSPC) or streak camera detection schemes. TCSPC offers superior dynamic range and sensitivity for longer timescales ($>100\text{ps}$), whereas streak cameras provide better temporal resolution ($\sim 1\text{ps}$) for ultrafast phenomena [200]. In this work, the TRPL system mainly consists of the High-Q 2 laser as the excitation source and SPC-130EM (Becker & Hickl) single photon counter which trigger by the single photon detector ID230 (ID Quantique) with a minimum time resolution of 200ps.

For self-assembled semiconductor QDs, TRPL measurements reveal characteristic multiexponential decay profiles that reflect the complex interplay between radiative and non-radiative processes. At low temperatures ($\leq 10\text{K}$), single QDs typically exhibit monoexponentially decays with lifetimes ranging from 0.5-2ns for InAs/GaAs systems, corresponding to the radiative recombination of confined excitons [201]. Temperature-

dependent TRPL further reveals thermal activation of non-radiative channels, manifesting as accelerated decay components at elevated temperatures.

Excitation power-dependent TRPL studies provide invaluable information about many-body effects in QDs. At low excitation densities, single exciton dynamics dominate, while increasing power introduces biexciton and charged exciton states with distinct lifetime signatures. The biexciton-to-exciton lifetime ratio offers direct insight into the enhancement of oscillator strength due to Coulomb interactions [201]. Moreover, resonant excitation TRPL measurements enable investigation of coherent phenomena including Rabi oscillations and pure dephasing processes critical for quantum information applications [202].

Recent advances in TRPL instrumentation have enabled spatial mapping capabilities, combining the benefits of micro-PL with temporal resolution. These hyperspectral TRPL measurements generate comprehensive datasets correlating spatial position, emission energy, and decay dynamics across QD samples, providing unprecedented insights into how sample status influences carrier behavior [203].

3.4.SUMMARY

This chapter highlights the MBE as a sophisticated crystal growth technique that operates in ultra-high vacuum conditions (10^{-8} to 10^{-12} mbar). This method enables exceptional precision in the creation of semiconductor materials by controlling atomic or molecular beam fluxes directed onto heated substrate surfaces. MBE achieves remarkably slow deposition rates—approximately one monolayer per second—which allows for precise control over film thickness, superior purity, and minimal crystallographic defects.

A standard MBE system consists of three interconnected chambers: the growth chamber (main chamber), buffer chamber, and load lock chamber. The growth chamber houses effusion cells containing elements like gallium, indium, aluminum (Group III), as well as arsenic and antimony (Group V), along with dopants such as silicon (n-type) and beryllium (p-type). These chambers are separated by gate valves to maintain proper vacuum conditions.

Critical to MBE operation is in-situ monitoring through techniques like Reflection High Energy Electron Diffraction (RHEED). This analytical tool directs high-energy electrons at a grazing angle onto the surface, creating diffraction patterns that provide real-time information about surface morphology, reconstruction states, and growth rates.

The document also describes a modified MBE system integrated with Direct Laser Interference Patterning (DLIP). This setup uses a Nd: YAG laser operating at 355 nm wavelength to create four sub-beams that converge on the sample surface at precise angles. The integration enables in-situ patterning during growth, allowing for novel nanostructured semiconductor materials.

For characterization, Atomic Force Microscopy (AFM) provides three-dimensional topographical images with nanometer resolution by detecting forces between a sharp tip and the sample surface. Photoluminescence (PL) spectroscopy complements this by analyzing the light emitted when excited electrons recombine with holes, revealing crucial information about bandgap, defect states, and carrier dynamics in the semiconductor materials.

4. AUTO-MAPPER SYSTEM FOR AUTOMATED SPATIAL PHOTOLUMINESCENCE SPECTROSCOPY

This chapter includes the Automapper system enables optical imaging method that simultaneously achieves nanometer-scale spatial resolution and automatically PL spectrum acquisition, allowing for visualization of nanoscale intensity or wavelength mapping by photoluminescence dynamics. The Chapter starts with the objectives of the Automapper system. Then the details of the design logic of the system and two different system set-ups are well explained. Some results of intensity mapping are shown after. The summary of the Automapper system presents at last.

4.1. OBJECTIVES AND AIM OF THE AUTOMAPPER SYSTEM

Photoluminescence intensity mapping has become an essential characterization technique for developing and optimizing semiconductor quantum dot structures in advanced laser applications. The Stranski-Krastanov growth method has emerged as the standard for producing coherent, defect-free quantum dots for GaAs-based structures with embedded InAs QDs that operate at the 1.3 μm wavelength. These structures demonstrate superior performance characteristics, including lower threshold current density, higher gain, and enhanced quantum efficiency. However, achieving optimal device performance requires meeting multiple criteria simultaneously: sufficiently deep localizing potential, small QD size, high uniformity, substantial volume filling factor, and defect-free material.

A significant challenge in quantum dot technology is the inherent inhomogeneity of individual quantum dot parameters across semiconductor wafers. Variations in size, chemical composition, and stress distribution lead to broadened emission spectra, ultimately reducing laser efficiency. This challenge necessitates high-resolution spatial characterization techniques to accurately assess QD uniformity and identify localized variations, which is precisely where PL mapping proves invaluable.

Photoluminescence intensity mapping provides a non-destructive method for assessing spatial variations in optical properties across QD structures. By systematically measuring PL spectra at defined intervals across a sample surface, researchers can generate detailed maps that correlate spatial position with critical parameters such as emission wavelength, linewidth, and intensity. Unlike other techniques such as transmission electron microscopy or scanning tunnelling microscopy, PL mapping can be performed under various environmental conditions without sample destruction, enabling researchers to study temperature-dependent phenomena that directly influence device performance.

The experimental approach described illustrates how PL mapping has been applied to understand the influence of InGaAs & InAs QD properties across the sample. By mapping samples with spiral pattern, researchers can systematically evaluate the region with pattern and density distribution across the sample. The high-resolution mapping (0.05 μm steps across a 10mm \times 10mm area) provides statistically significant data on spatial variations that reveal correlation lengths of property variations, helping identify whether inhomogeneities stem from growth conditions, substrate imperfections, or intrinsic material limitations. This level of understanding directly informs growth optimization strategies to enhance QD uniformity and ultimately improve device performance, establishing PL mapping as an indispensable tool for developing the next

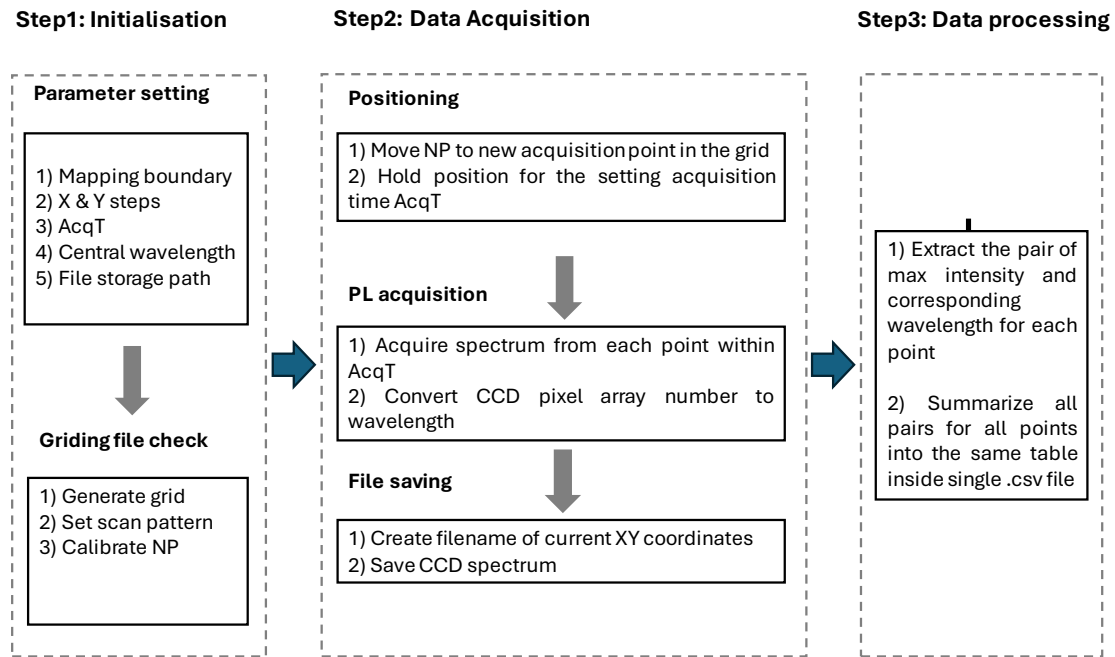
generation of high-performance quantum dot laser structures with the uniformity and efficiency required for commercial applications.

4.2. DEVELOPMENT OF THE AUTOMAPPER SYSTEM

This system demonstrates a comprehensive approach to addressing one of the key challenges in spatial spectroscopy: accurately tracking measurement positions across non-planar surfaces. By implementing an optional tilted-plane mapping algorithm and spiral scanning pattern, the system achieves efficient data collection while maintaining spatial accuracy.

4.2.1. TECHNICAL ROUTE

The system follows a modular design with clear separation between initialization, data acquisition, and processing components. Each module handles a specific aspect of the workflow, enhancing maintainability and flexibility as **Figure 4.1** shows. The system starts with the key architectural feature which depended on JSON-based configuration system that stores critical parameters including datapoint file paths, corner axis coordinates, step lengths, raw data storage path, and delimiter preferences with optional setting of plane fitting, detector acquisition time and post data fitting. This configuration-driven approach allows parameters to be modified without code changes, enables multiple experimental setups to be saved as different configuration files, and maintains a clear record of experimental parameters. The configuration loading module implements error handling for missing paths, ensuring system robustness during initialization.



AcqT : Acquisitiontime. NP : Nano positioner.

Figure 4.1 Flow chart of Automapper System.

Then the system flow to the data storage part, the system implements a hierarchical architecture where individual measurement files are named according to their spatial coordinates, each file contains wavelength and intensity pairs for that specific position, and a post-processing step can aggregate these measurements into a summary file. This approach balances storage efficiency with data accessibility, allowing both individual point analysis and comprehensive spatial mapping.

The cornerstone of the system's spatial accuracy is the implementation of planar equations in the geometry module. Rather than using simple three-point plane fitting, the system employs optional advanced plane detection algorithms based on the 3D Hough Transform as described in research by Hulik et al. (2014) [204]. This implementation of the 3D Hough Transform allows for robust plane detection even in the presence of noisy or imperfect measurement data. Unlike basic plane fitting that requires exactly three defined points, the Hough Transform approach can identify the most probable plane from a point cloud with many potential surface points. This

provides significant advantages for spectroscopic mapping across samples with complex topography or when dealing with calibration uncertainties. A particularly innovative aspect is the spiral scanning algorithm. Unlike traditional raster scanning that moves line-by-line, this algorithm starts from a central point, moves outward in a spiral pattern, and dynamically increases step length as it progresses. This spiral approach prioritizes measurements near the center, which is typically the region of interest, and allows for early termination if needed while still providing complete central coverage.

4.2.2. INITIALISATION

During the system's initialization phase, a carefully orchestrated sequence of operations prepares the spectroscopic mapping apparatus for data collection. The process begins by loading configuration parameters from the JSON file, which contains essential information about file paths, step lengths, and the crucial corner coordinates that define the measurement plane. These corner points, typically containing known x, y, and z coordinates, serve as the foundation for all subsequent spatial calculations.

The system then applies mathematical algorithms to determine the plane equation based on these corner points. If the plane fitting option is enabled, the system loads configuration parameters, applies the 3D Hough Transform to calculate the optimal measurement plane, generates a grid of measurement points using a spiral algorithm, and writes these points to a CSV file for verification. The Hough Transform approach first converts the corner point coordinates into a discretized parameter space where each bin represents a possible plane. By accumulating votes from all input points, the algorithm identifies the parameters of the most likely plane, even if some input coordinates contain measurement errors.

As the points are generated as **Figure 4.2** shows, the system continuously verifies that each position falls within the defined boundary conditions. These safety checks are critical to prevent potential hardware damage that could result from attempting to move positioning equipment beyond its physical limits. Several validation mechanisms are employed, including range checking for absolute position values and logical validation to ensure minimum values are indeed less than maximum values.

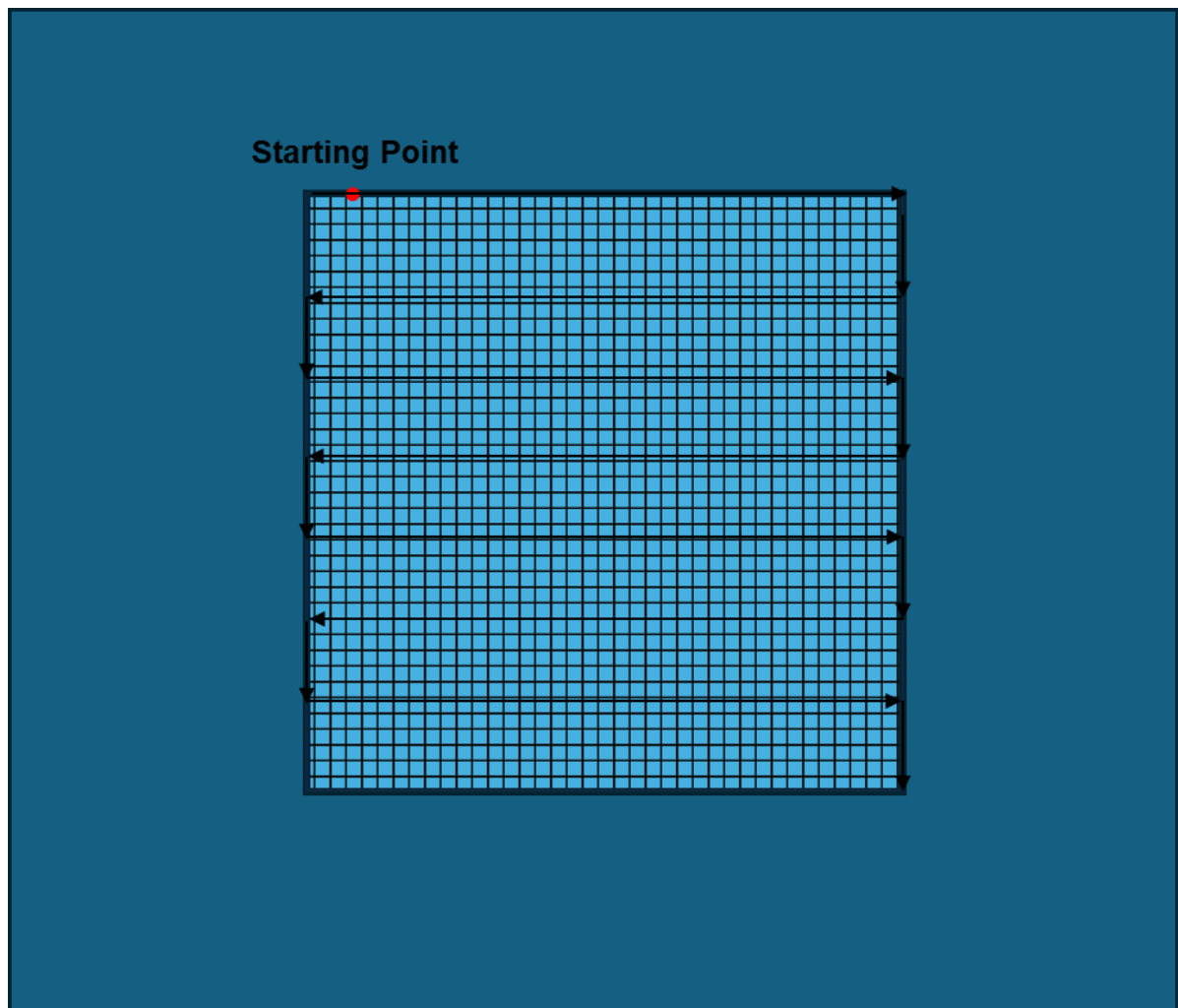


Figure 4.2 Example of scanning route of the preset grid.

When all points have been calculated and verified, the system writes the complete measurement grid to a CSV file. This file serves multiple purposes: it provides a record of the planned measurement positions, allows for visual inspection of the pattern before beginning the time-consuming acquisition process, and serves as the reference map for

the actual data collection phase. The file includes precise x, y, and z coordinates for each measurement point, ensuring the positioning system can accurately navigate to each location during data acquisition. And option like detector acquisition time, post data smoothing and log are ready to pass to the programme. This thorough initialization process, with its emphasis on mathematical precision and hardware safety, forms the foundation for reliable spectroscopic mapping across non-planar sample surfaces.

4.2.3. DATA ACQUISITION

The data acquisition phase represents the operational heart of the automated spectroscopy system, where theoretical measurement coordinates transform into physical spectral data. This phase consists of positioning, spectrum acquisition, and file saving operations. The positioning subsystem interprets coordinate data and translates it into physical movement commands, requiring nanopositioning stages with sub-micron precision. Once positioned, the system stabilizes before capturing the complete spectral response, often integrating detector signals over a predefined acquisition time to improve signal-to-noise ratio. As spectra are collected, the system saves data with filenames incorporating spatial coordinates, creating an unambiguous connection between location and spectral information. The CSV format pairs wavelength values with corresponding intensity measurements, creating self-contained data files that are human-readable and easily imported into analysis software. There are two sets of system Via different programming platform for various requirements.

4.2.3.1. PYTHON-BASED SYSTEM

For the high resolution, code execution speed and massive data acquisition requirements, the python language has dominated for decades. With compared to the LabVIEW, the python SDK provided by Standa for the Nanopositioner is more reliable. And with the fixed central wavelength from the HORIBA FHR1000, it will provide a single frame of 40.8nm (with 500um entrance slit) to the 1024 pixels iDus detector which led to a maximum resolution around 0.04nm.

This python-based system process begins with the positioning subsystem, which interprets the coordinate data generated during initialization and translates it into physical movement commands. For each point in the measurement grid, the system must carefully position its optical components at exact x, y, and z coordinates. This positioning must account for mechanical precision limitations and potential backlash in the positioning system. The positioning system typically employs nanopositioning stages with sub-micron precision to ensure accurate placement at each measurement point. Once the system arrives at a specified coordinate, it must stabilize before acquisition begins, eliminating vibrations or drift that could compromise measurement quality.

After positioning, the spectrum acquisition phase activates the spectroscopic instrumentation. The system captures the complete spectral response at each spatial location, recording intensity values across the specified wavelength range. This often involves integrating detector signals over a predefined acquisition time to improve signal-to-noise ratio, especially for weak spectral features. The acquisition parameters, such as integration time and spectral resolution, remain constant throughout the mapping to ensure data comparability across the measurement grid. At each position,

the system may perform additional real-time processing, such as background subtraction or normalization, to enhance spectral quality.

The final component of the acquisition phase involves systematic data storage. As each spectrum is collected, the system must reliably save the data with a filename that preserves its spatial context. The implemented naming convention directly incorporates the x, y, and z coordinates of each measurement position, creating an unambiguous connection between spatial location and spectral data. For example, a measurement at position (1000, 2000, 150) would be saved as "1000_2000_150.csv". This coordinate-based naming scheme enables straightforward data retrieval and spatial reconstruction during later analysis.

The data storage module employs a simple yet effective CSV format that pairs wavelength values with their corresponding intensity measurements. This two-column approach creates self-contained data files that include complete spectral information without requiring external calibration files. The CSV format offers several advantages: it's human-readable, easily imported into various analysis software, and efficiently compressible for long-term storage.

By segmenting the acquisition phase into these three distinct operations—positioning, spectrum acquisition, and file saving—the system maintains clear separation of concerns while ensuring reliable data collection. The process repeats for each point in the measurement grid, gradually building a comprehensive spatial map of spectroscopic properties as **Table 4.1** shows. The careful implementation of this acquisition phase enables accurate mapping of spectral features across non-planar surfaces with minimal operator intervention, making it suitable for extended measurement sessions that might require thousands of individual spectra to be collected across a sample surface.

Table 4.1 Overall mapping flowchart of Python-based system

Flowchart Step	Corresponding Code Files	Purpose
Step 1: Setup & Grid Generation	config. Json, getDatapoints.py, Preprocess.py, loadConfig.py	Defines scan pattern, step size, and generates a grid file.
Step 2: Acquisition Process	evenPoint.py, getDatapoints.py, DataStore.py	Moves NP, acquires spectrum, converts CCD data, and saves results.
Step 3: Data Processing & Summary	outputPos.py, Preprocess.py, DataStore.py	Extracts maximum intensity per point and compiles data into setting destination

4.2.3.2. LABVIEW-BASED SYSTEM

LabVIEW is known for its compatibility, visualization interface and accessibility. Firstly, The LabVIEW-based system could accomplish a wide range of scans by controlling the spectrometer to grab multiple frames with varied wavelength range from the detector and combine them into the output spectrum as the **Figure 4.3** shows.

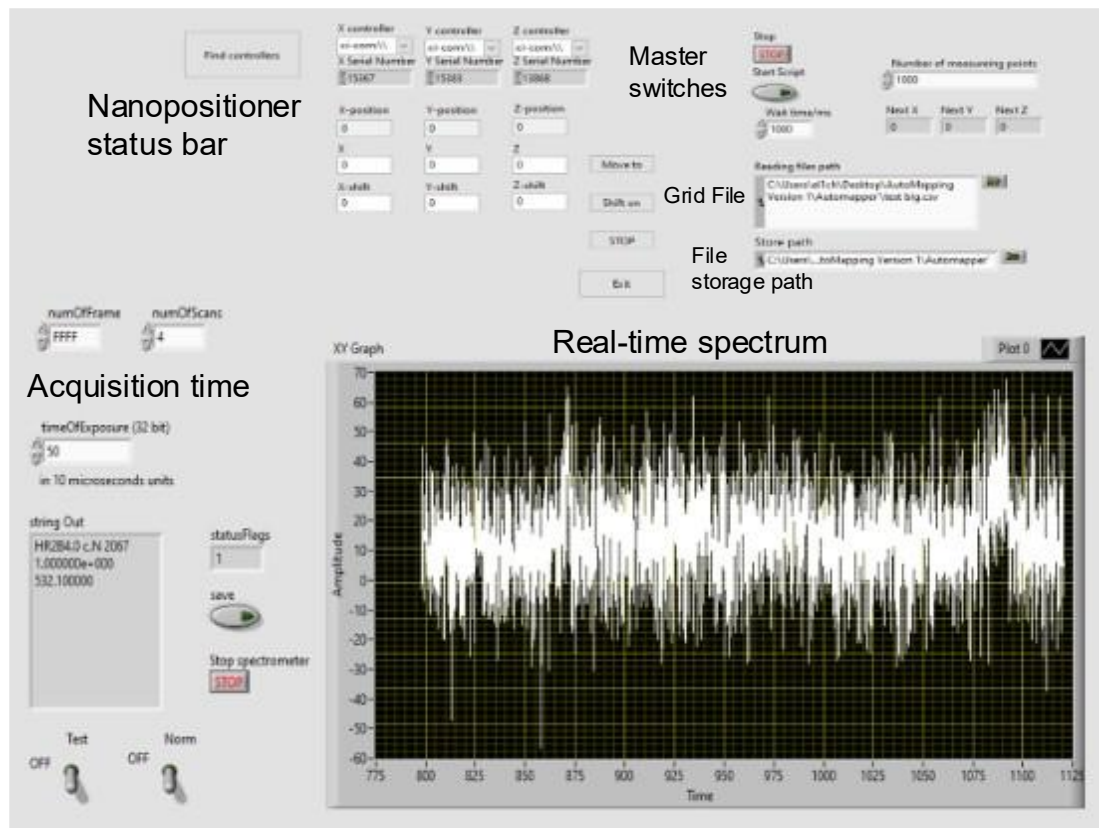


Figure 4.3 The running LabVIEW-based system.

For the initialization phase, use LabVIEW's file I/O VIs to read the JSON configuration file and parse the parameters. The JSON functionality can be implemented using the JKI JSON library or native LabVIEW JSON parsing VIs. The 3D Hough Transform plane detection algorithm can be implemented using LabVIEW's mathematics VIs or by calling external code through the MathScript Node.

The acquisition phase benefits from LabVIEW's hardware integration capabilities. Use instrument drivers for positioning stages (such as NI-Motion or vendor-specific drivers) and spectrometers (Ocean Optics, Horiba, or similar). Create a state machine architecture for coordinating the positioning, acquisition, and file saving operations. LabVIEW's file I/O functions streamline the creation of properly named CSV files for each measurement.

4.2.4. POST DATA PROCESSING.

When all points have been calculated and verified through the 3D Hough Transform algorithm, the system generates a comprehensive mapping grid that conforms to the detected sample plane. This grid data is then systematically organized and saved to a CSV file, marking the completion of the initialization phase. This output file serves as a critical bridge between the theoretical mapping design and the physical measurement process that follows.

The CSV file functions as a multifaceted resource within the workflow. First, it provides a permanent record of all planned measurement positions, documenting the exact spatial sampling strategy used in the experiment. This documentation is invaluable for experimental reproducibility and allows researchers to revisit the exact measurement conditions during later analysis or when comparing results across multiple samples.

Before committing to the time-intensive data acquisition process, researchers can use this file to visually inspect the planned measurement pattern. The coordinates can be imported into visualization software or the system's built-in preview function to confirm proper coverage of regions of interest and appropriate measurement density. This verification step often saves substantial time by identifying potential issues before physical measurements begin.

During the actual data collection phase, this file serves as the authoritative reference map that guides the positioning system. The instrumentation controller sequentially reads each coordinate triplet, directing the motorized stages to position optical components at precise x, y, and z locations. The inclusion of pre-calculated z-coordinates is particularly critical, as it ensures the system maintains proper focus and working distance while following the sample's non-planar topography.

Each record in the file contains the exact numerical coordinates with sufficient precision to match the capabilities of the positioning hardware, typically in micrometre or nanometer units. This precision ensures that the physical measurement points will accurately correspond to the intended sampling pattern determined during initialization as the **Figure 4.4** shows.

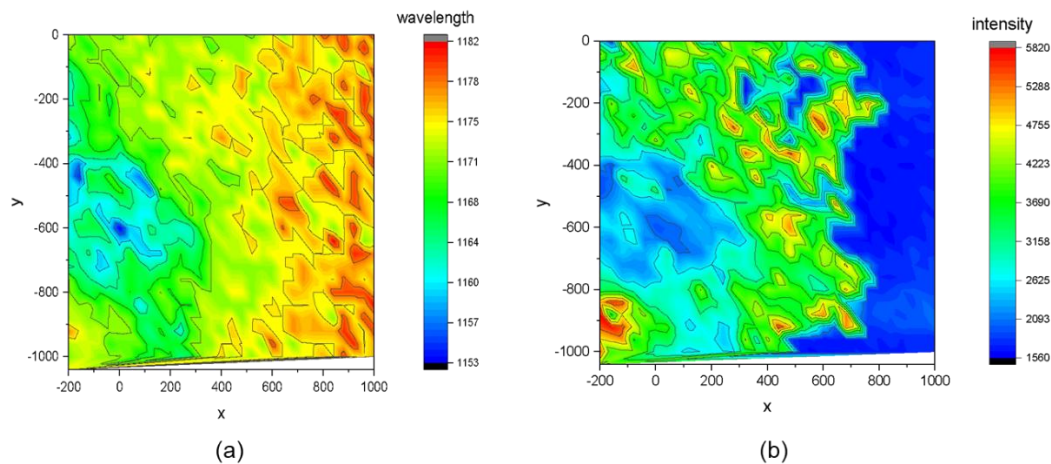


Figure 4.4 Example of automapping results of an InAs QDs sample of a 1X1 mm region by (a) wavelength distribution. (b) Intensity distribution.

By establishing this detailed spatial framework before any spectroscopic measurements begin, the system creates a solid foundation for reliable data collection. This thorough initialization process, emphasizing both mathematical precision and hardware safety constraints, enables consistent and accurate spectroscopic mapping across samples with complex surface geometries.

4.3. SYSTEM ACHIEVEMENTS

This system appears well-suited for several scientific applications. The intensity vs. wavelength data structure aligns with photoluminescence spectroscopy requirements. The tilted plane handling makes it ideal for mapping optical properties across non-flat

samples. The system could identify spatial variations in emission or absorption properties of heterogeneous materials. Finally, the spatial resolution could detect defects or variations in semiconductors or optical materials.

In conclusion, the automated spectroscopy system demonstrates a sophisticated approach to spatial spectroscopic mapping through its innovative plane-fitting algorithm and spiral scanning pattern with various setup. Its modular architecture and configuration-driven operation provide flexibility while maintaining robustness. The combination of mathematical rigor in the plane calculations with practical data management creates a system that addresses real-world challenges in spectroscopic mapping, particularly for non-planar samples. The spiral scanning pattern optimization further enhances efficiency by prioritizing central regions of interest. While additional enhancements could be implemented, such as adaptive sampling or parallel processing, the current system represents a well-designed solution for automated spatial spectroscopy applications in research and materials characterization environments.

4.4.SUMMARY

This system appears well-suited for several scientific applications. The intensity vs. wavelength data structure aligns with photoluminescence spectroscopy requirements. The tilted plane handling makes it ideal for mapping optical properties across non-flat samples. The system could identify spatial variations in emission or absorption properties of heterogeneous materials. Finally, the spatial resolution could detect defects or variations in semiconductors or optical materials.

5. EPITAXY AND CHARACTERIZATION OF ORDERED InGaAs/AlGaAs/GaAs QDS ARRAY VIA DROPLET EPITAXY

This chapter explores how to fabricate ordered quantum dot arrays using DLIP, which integrating in-situ lithographic patterning with droplet epitaxy. The study focuses on three main areas: (i) forming ordered InGaAs QD arrays via DLIP-assisted MBE, (ii) optimizing growth parameters for site-controlled nucleation without compromising optical quality, and (iii) analyzing the structural and optical properties of the resulting QD arrays.

5.1. INTRODUCTION

The development of InGaAs/GaAs quantum dot (QD) arrays addresses a critical need in quantum information technologies, where deterministic positioning of precisely engineered quantum emitters is essential. These nanostructures exhibit superior optical properties—including narrow emission linewidths, high quantum efficiency, and tunable emission wavelengths (900–1550 nm)—making them ideal for quantum photonic applications such as indistinguishable single-photon generation [115, 205]. Arrays of spatially ordered InGaAs/GaAs quantum dots are particularly valuable for integration with photonic crystal cavities and waveguides, enabling strong light–matter interactions that are essential for implementing quantum gates, repeaters, and on-chip quantum networks [206, 207]. Furthermore, scalable fabrication of uniform QD arrays overcomes the inherent randomness of traditional self-assembly, significantly improving device yield and reproducibility for practical quantum technologies.

Self-assembled semiconductor quantum dots have emerged as a cornerstone of quantum photonics and optoelectronics due to their three-dimensional quantum confinement, enabling discrete energy levels and high localization of carriers [151, 208]. The concept of self-assembled QDs originated in the early 1990s, with the spontaneous formation of coherent 3D islands in strained heteroepitaxial systems—initially observed in Ge/Si(100) and later in InAs/GaAs systems [118]. This discovery led to intensive investigation of the fundamental aspects of heteroepitaxial growth systems, revealing that the formation of coherent islands is directed by the elastic relaxation energy resulting from lattice mismatch between the substrate and deposited material [115, 209].

Conventional fabrication of self-assembled QDs predominantly relies on the Stranski-Krastanov (SK) growth mode, wherein epitaxial strain between lattice-mismatched materials drives the spontaneous formation of three-dimensional islands after a critical thickness of a wetting layer. The Stranski-Krastanov (S-K) growth mode has been the predominant method for fabricating InGaAs/GaAs QDs. The conventional approach to QD growth is based on the Stranski–Krastanov (SK) mode, where lattice mismatch-induced strain drives the transition from 2D wetting layers to 3D island formation once a critical thickness is surpassed. In the InAs/GaAs(001) system, this critical thickness ranges between 1.5 and 1.8 monolayers (ML), depending on the growth temperature [210, 211]. Typical surface densities of SK-grown InGaAs QDs are between 1×10^8 and 1×10^{11} cm⁻², with heights of 1-15 nm and widths of 10-100 nm [212]. While SK growth produces high-quality QDs, it suffers from stochastic nucleation, resulting in variability in size, shape, and composition, which complicates deterministic integration into photonic devices.

To address these limitations, droplet epitaxy (DE)—first introduced by Koguchi et al. in 1993—emerged as a strain-independent alternative that decouples group III and group V deposition [155]. DE enables the fabrication of both lattice-matched and lattice-mismatched III-V nanostructures, allowing the growth of structures like GaAs/AlGaAs QDs and InGaAs/GaAs QDs [155, 213, 214].

The development of $\text{In}_x\text{Ga}_{1-x}\text{As}/\text{Al}_{0.3}\text{Ga}_{0.7}\text{As}/\text{GaAs}$ system offers several distinct advantages for optoelectronic and quantum information applications. The inclusion of aluminum in the barrier layers creates a higher confinement potential for carriers within the QDs, improving performance at elevated temperatures. Additionally, the $\text{Al}_{0.3}\text{Ga}_{0.7}\text{As}$ barrier layers provide excellent lattice matching to GaAs substrates, minimizing defect formation while maintaining a significant band offset. The emission wavelength of these QDs can be precisely engineered by adjusting the indium content (x), allowing tuning from near-infrared to telecom wavelengths (900-1550 nm) [215]. This tunability makes the system highly versatile for various applications, including quantum key distribution, entangled photon generation, and integrated quantum photonic circuits.

Figure 5.1 Cross-section transmission electron microscopy photos: (a) 100 nm scale. (b) 20 nm scale for the $\text{In}_{0.6}\text{Ga}_{0.4}\text{As}/\text{GaAs}$ QDIP[216]. typically displays cross-sectional transmission electron microscopy (TEM) images, showing lens-shaped QDs with base diameters of 20–30 nm and heights of 5–8 nm, along with corresponding photoluminescence (PL) spectra exhibiting narrow linewidths (~20–40 meV), demonstrating high optical quality and uniformity.

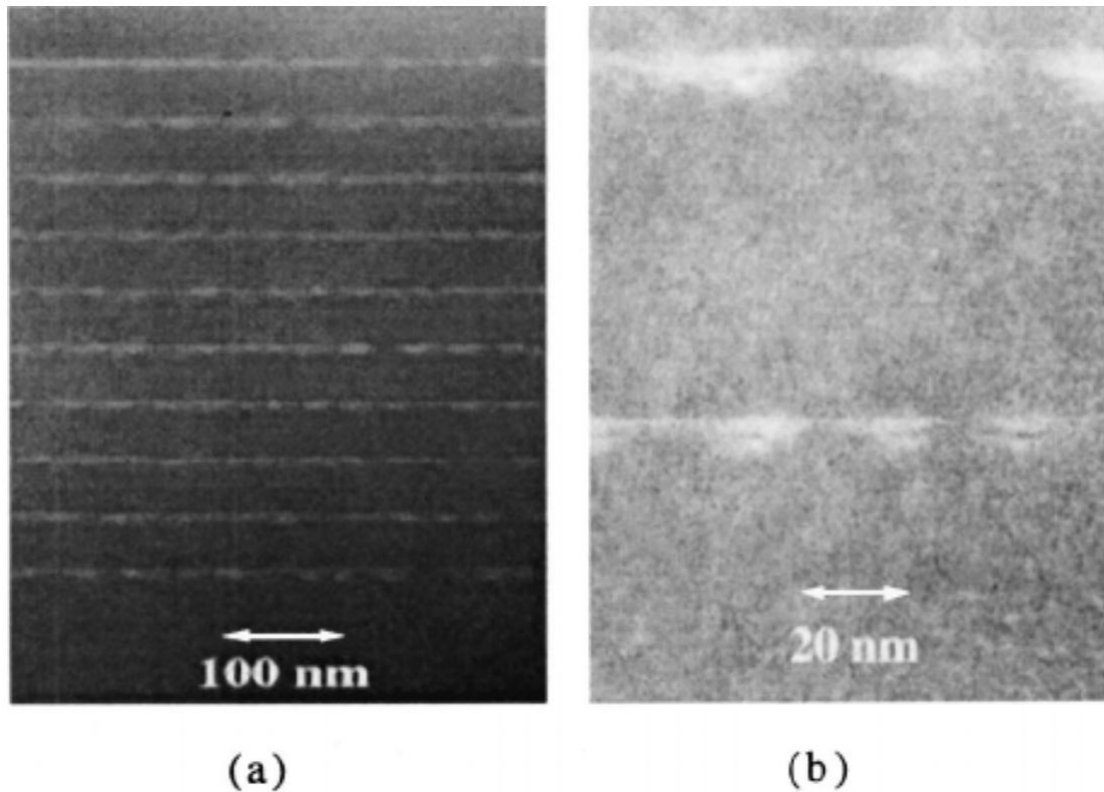


Figure 5.1 Cross-section transmission electron microscopy photos: (a) 100 nm scale. (b) 20 nm scale for the $\text{In}_{0.6}\text{Ga}_{0.4}\text{As}/\text{GaAs}$ QDIP[216].

Despite these advantages, fabricating high-quality structures requires precise control over parameters like substrate temperature, V/III flux ratio, and deposition rate. For DE, maintaining an ultralow As background is critical to avoid premature crystallization, necessitating long growth interruptions and advanced MBE protocols [217] [218].

Despite these advantages, fabricating high-quality structures requires precise control over parameters like substrate temperature, V/III flux ratio, and deposition rate. For DE, maintaining an ultralow As background is critical to avoid premature crystallization, necessitating long growth interruptions and advanced MBE protocols[100, 103] [111].

The development from S-K to DE growth modes represents a paradigm shift in control over QD properties, particularly for lattice-matched systems[219]. While S-K

growth relies on strain relaxation and is thus limited to lattice-mismatched material combinations, DE offers greater flexibility in material selection and nanostructure morphology, enabling the creation of complex structures including quantum rings and concentric rings [220]. This versatility, combined with advanced positioning techniques, positions the InGaAs/Al_{0.3}Ga_{0.7}As/GaAs system as a leading platform for next-generation quantum photonic devices and fundamental quantum optical studies.

The scope of this research encompasses both fundamental materials science and device applications. Beginning with a systematic investigation of template fabrication and growth kinetics, the work progresses to demonstrate functional devices that leverage the advantages of ordered QD arrays [221].

By addressing the critical challenge of spatial ordering in self-assembled quantum dots, this research aims to bridge the gap between the exceptional optical properties of epitaxial QDs and the deterministic integration requirements of advanced quantum photonic circuits [222].

5.2. EPITAXY OF PATTERNED In_xGa_{1-x}As QUANTUM DOT ARRAYS

This section detailed explains in detail the hybrid growth mechanism the hybrid growth mechanism of the sample, the comprehensive method to achieve highly ordered quantum dots Via DLIP-MBE.

5.2.1. PRINCIPLE OF THE EPITAXIAL PROCESS

In this thesis, droplet epitaxy offers an alternative growth paradigm that decouples group III and V deposition steps. Initially, metallic group III droplets form on the substrate surface, followed by crystallization through exposure to group V flux [223]. This approach circumvents the strain requirement inherent to SK growth, enabling the

fabrication of lattice-matched QDs. The process is governed by surface kinetics rather than strain relaxation, with droplet formation following Ostwald ripening mechanisms characterized by the temporal evolution of droplet size distribution $n(r, t)$ according to the Lifshitz-Slyozov-Wagner theory [224].

Direct laser interference patterning (DLIP) has emerged as a promising technique for creating ordered templates for site-controlled QD growth. The physical principles derive from the interference of multiple coherent laser beams generating periodic intensity distributions. When Λ represents the pattern periodicity as previously described in **Chapter 2.2.3.2**, this periodic intensity distribution creates thermal gradients on semiconductor surfaces, with temperature profiles calculated using the heat diffusion equation $\partial T/\partial t = D\nabla^2 T + Q(r, t)/\rho C_p$, where D represents thermal diffusivity, ρ is density, C_p denotes heat capacity, and $Q(r, t)$ is the heat source term from laser absorption [225].

The pattern formation mechanisms in DLIP involve complex surface modification processes including localized melting, evaporation, and recrystallization. Surface temperature can transiently reach several thousand kelvins with gradients exceeding 10^9 K/m, generating thermocapillary flows described by the Marangoni effect, where surface tension gradients ($\partial\gamma/\partial T$) drive material transport [226] as **Figure 5.2** shows. The characteristic ripple structures formed through DLIP exhibit periodicities ranging from sub-micron to several microns, with depths controlled by laser fluence, number of pulses, and material properties [227].

The thermal gradient formation mechanism during DLIP is governed by the Gibbs-Marangoni effect, wherein the spatially modulated intensity distribution induces localized heating at interference maxima. The thermal gradient drives the migration of subsequently deposited metallic adatoms toward cooler regions, creating ordered

nucleation sites. The optimization of laser pulse energy is critical, with experimental results demonstrating that energies between 40-55 mJ/cm² produce the most uniform patterns. Exceeding the threshold value of 40 mJ results in pattern degradation through overlapping thermal fields and potential surface damage.

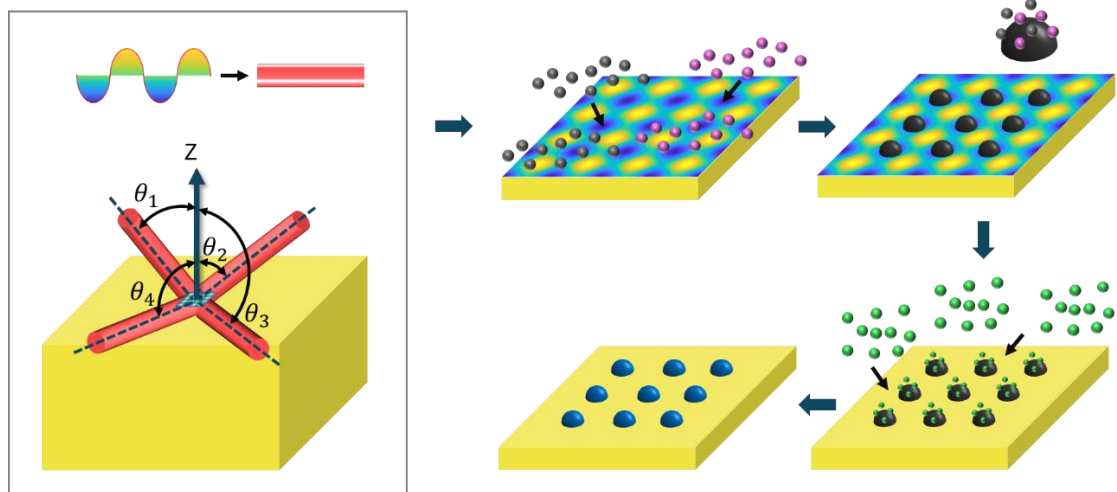


Figure 5.2 Schematic diagram of (a) Demonstration of Four-beams laser interference patterning with same incident angle. (b) Formation process of InGaAs DE quantum dot array.

5.2.2. SAMPLE STRUCTURE

All the samples shown in this chapter are grown on 2-inch the (001) undoped GaAs substrate, **Figure 5.3** presents the schematic cross-sectional structure a typical sample. The growth condition for each layer maybe varied towards further investigation of the influence of the growth parameter which would be presented in **chapter** 错误!未找到引用源。 .

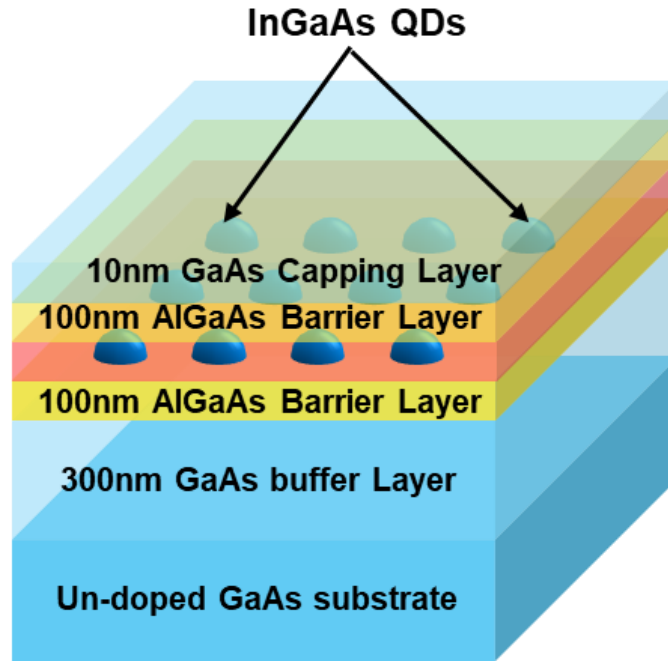


Figure 5.3 Comprehensive schematic cross-sectional structure diagram of the InGaAs/AlGaAs/GaAs quantum dots array sample.

5.2.3. SAMPLE GROWTH

Before epitaxy of the samples in this thesis, the substrate wafer has been deoxidated by raise the temperature to 630°C to remove oxide. Then a 300nm GaAs buffer layer was grown priorly on the substrate and a 100nm $\text{Al}_{0.3}\text{Ga}_{0.7}\text{As}$ layer on the buffer layer at 600°C with a growth rate of 3.0 \AA s^{-1} , which indicated by the RHEED oscillation period. Then the sample reduce the temperature to 150°C and annealing to 2 hours, and the arsenic valve was closed until the background pressure inside the growth chamber was reduced to 3×10^{-10} mbar.

Samples presented in this chapter are applied with experimental setup utilized a flash-lamp-pumped Nd: YAG laser operating at its third harmonic (355 nm) with 7 ns pulse duration. The laser beam was split into four coherent beams with incident angles of $\theta_1 = \theta_2 = \theta_3 = \theta_4 = 58^\circ$ to produce a precise interference pattern on the substrate

surface. Afterwards, in-situ four-beam DLIP with a vary laser intensity between 40-55mJ/cm² was applied on the Al_{0.3}Ga_{0.7}As layer with momentarily stop of the substrate rotation. Additionally, a 20s interruption to reduce the sample temperature to 100°C.

The droplet epitaxy process builds upon the laser-patterned surface through a sequence of carefully controlled steps. A 1.78-2.27ML In/Ga was provided at a GR of 0.25 ML/s to form metallic droplets with raising substrate to 200°C for 1h 40mins. Following DLIP treatment, the residual arsenic is evacuated to achieve a group III-terminated surface condition [228]. In_xGa_{1-x}As adatoms (ranging from 1.78 to 2.5 ML) are deposited, forming metallic droplets preferentially at the thermal pattern's cooler regions. These droplets are subsequently crystallized through controlled exposure to As₄ flux for 10mins, transforming them into semiconductor quantum dots [229]. The spatiotemporal dynamics of this crystallization process are governed by surface diffusion kinetics and follow the Volmer-Weber growth mode [230]. The InGaAs nanostructure is capped with a 30 nm Al_{0.3}Ga_{0.7}As layer under 400°C, then the substrate temperature rises to 600°C for 10min interruption which follows a 70nm Al_{0.3}Ga_{0.7}As layer growth, a 10 nm GaAs layer is grown on the top of the sample under 600°C.

To investigate how DLIP and growth parameters affect the ordering of InGaAs QDs, varied parameter including laser interference pulse energy, and InGaAs coverage, capping layer, and In/Ga ratio. The next section presents the detailed experimental results of surface morphology and PL spectroscopy.

5.3.RESULT AND DISCUSSION

This chapter detailed discussed the systematic investigation of the correlation between structural morphology and optical properties in In_xGa_{1-x}As quantum dot arrays fabricated via direct laser interference patterning (DLIP). Atomic force microscopy analyses reveal that InGaAs coverage (1.78-2.27 ML) critically influences dot density,

size distribution, and site occupancy, with optimal uniformity achieved at 2.0-2.07 ML. Higher coverage leads to increased coalescence and degraded size homogeneity. Correspondingly, photoluminescence studies demonstrate that structural uniformity directly translates to superior optical emission, with single-site quantum dots exhibiting remarkably narrow linewidths (9.7 meV) and discrete emission peaks. The research establishes precise processing windows for laser fluence and growth parameters that optimize both structural ordering and optical performance for quantum photonic applications.

5.3.1. INFLUENCE FACTORS OF THE GROWTH PROCESS

Comprehensive morphological analysis of the InGaAs quantum dot arrays was conducted using atomic force microscopy (AFM) to elucidate the effects of growth parameters on QD formation and spatial distribution. This section presents a systematic investigation of the relationship between InGaAs coverage and resultant quantum dot characteristics.

5.3.1.1. LASER INTENSITY

Experimental investigations reveal that the applied laser energy plays a pivotal role in addressing the metallic droplets through the Gibbs-Marangoni effect. Following the absorption of UV laser pulses with an interference pattern on the growth surface, a systematic temperature distribution develops, with localized maxima at interference peaks. Our results demonstrate that within a critical threshold value of single-pulse UV laser energy (approximately 40 mJ for the growth structure employed in this study), the thermal lateral gradient drives metallic droplet migration toward cooler regions with enhanced probability and uniformity [113, 231].

Comparative analysis of samples grown with 2 ML of $\text{In}_{0.15}\text{Ga}_{0.85}\text{As}$ under different laser fluence energies (55 mJ/cm^2 versus 40 mJ/cm^2) reveals significant morphological differences. As illustrates in **Figure 5.4**, samples exposed to higher energy (55 mJ) exhibit reduced symmetry and increased instances of multiple dots overlapping at common nucleation sites. Conversely, samples processed with threshold energy (40 mJ/cm^2) display superior uniformity with a consistent pitch distance of approximately 300 nm and reduced central pit depth ($0.5 \pm 0.1 \text{ nm}$).

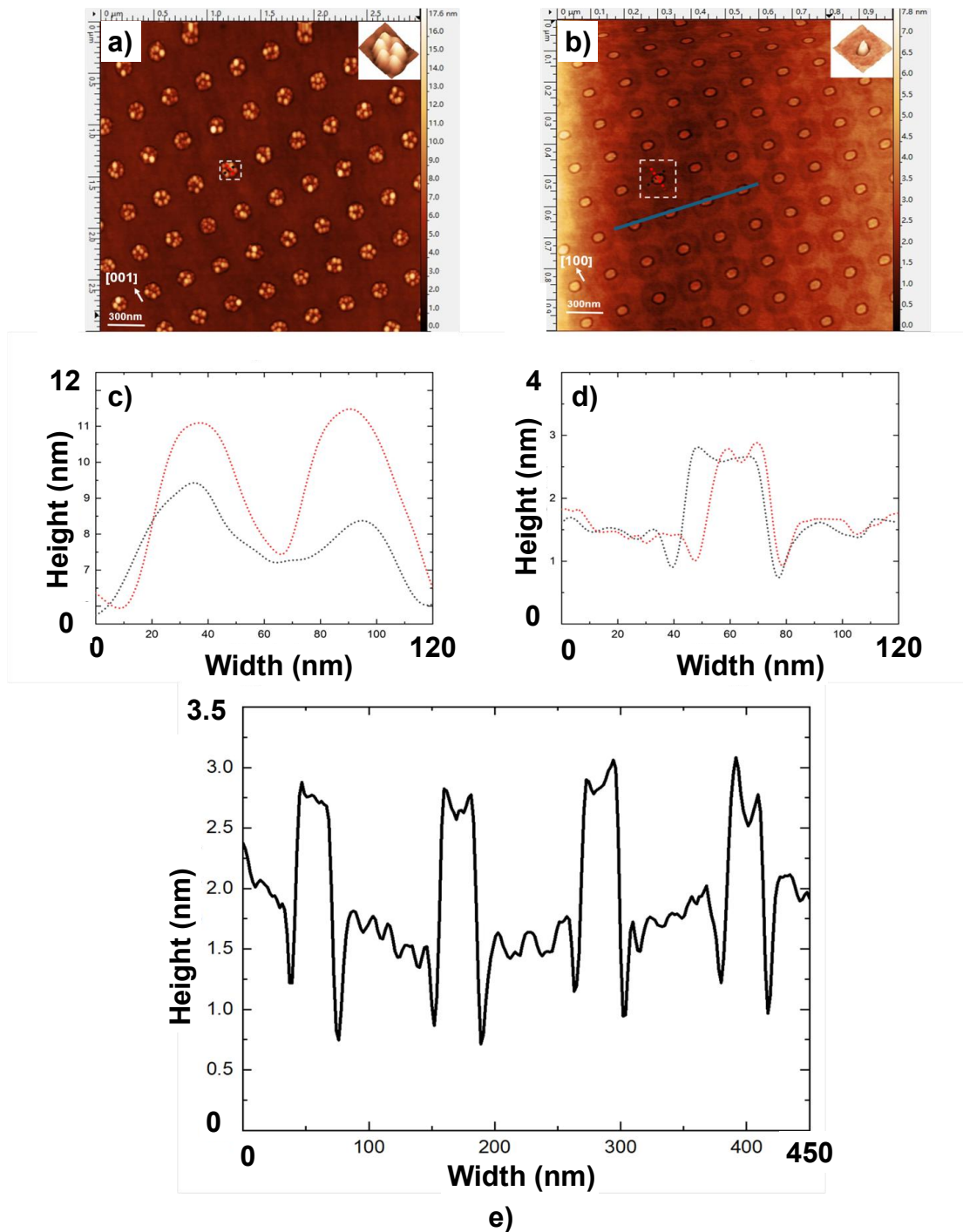


Figure 5.4 Effects of laser energy on quantum dot morphology. (a) AFM micrographs of InGaAs QD arrays fabricated using laser energy of 55 mJ/cm². (b) QD arrays fabricated using 40 mJ/cm². (c)-(d) Cross-sectional height profiles along the direction. (e) Statistical distribution of dot height and diameter for both energy regimes.

Quantitative analysis presented in **Table 5.1** demonstrates that exceeding the critical laser energy threshold results in not only poorer symmetry but also significant dot size broadening. The mean diameter increases from 42 ± 4 nm to 58 ± 9 nm, while height variations expand from 5.8 ± 0.6 nm to 8.3 ± 1.2 nm, representing a substantial decline in dimensional uniformity.

Table 5.1 Quantitative comparison of QD morphological parameters as a function of laser energy

Parameter	40 mJ/cm ²	55 mJ/cm ²
Mean diameter (nm)	42±4	58±9
Mean height (nm)	5.8±0.6	8.3±1.2
Areal density (μm ⁻²)	11.1±0.3	9.7±1.2
Size uniformity (%)	90.5	84.3
Central pit depth (nm)	0.5±0.1	0.9±0.2

These observations align with theoretical models suggesting that above-threshold laser energy induces excessive thermal gradients, leading to uncontrolled droplet coalescence and migration [114]. The results establish a critical processing window for laser energy to achieve optimal QD uniformity and spatial ordering.

5.3.1.2. InGaAs COVERAGE FOR ORDERED QD FORMATION

This subsection discussed different In/Ga ratio versus different In/Ga Coverage for order QDs array formation.

5.3.1.2.1. $\text{In}_{0.15}\text{Ga}_{0.85}\text{As}/\text{Al}_{0.3}\text{Ga}_{0.7}\text{As}/\text{GaAs}$ SYSTEM

The variation in $\text{In}_{(x)}\text{Ga}_{(1-x)}\text{As}$ coverage exhibits a clear correlation with quantum dot density and morphology. **Figure 5.5** presents three-dimensional AFM images of samples with identical growth conditions and laser parameters but varying InGaAs coverages (1.78-2.27 ML). Statistical analysis reveals that as deposition coverage increases, the average number of QDs per nucleation site progressively increases from approximately 1 to 8, accompanied by systematic changes in nanoisland morphology.

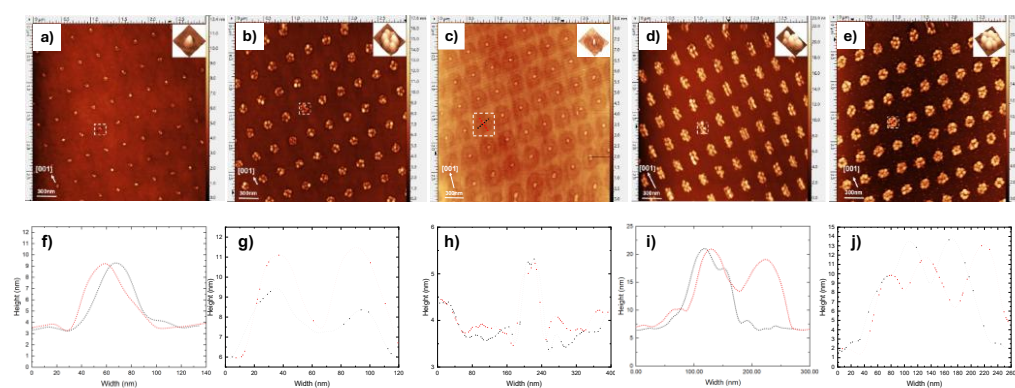


Figure 5.5 Evolution of quantum dot morphology with increasing In/Ga coverage for $\text{In}_{0.15}\text{Ga}_{0.85}\text{As}$. Three-dimensional AFM images showing QD formation at coverage values of: (a) 1.78 ML. (b) 2.0 ML. (c) 2.07 ML. (d) 2.17 ML. and (e) 2.27 ML. Lower panels (f-j) show corresponding cross-sectional profiles along the [001] direction.

The progression in material coverage demonstrates the dynamics of QD formation. At 1.78 ML coverage, QDs are sparse, smaller, and exhibit reduced uniformity, representing early-stage nucleation. As coverage increases to 2.0 ML and 2.07 ML, QD density increases with improved size uniformity, establishing a critical coverage threshold for optimal QD density and dimensional homogeneity. Beyond this threshold (at 2.17 ML and 2.27 ML), further increases in coverage enhance QD density but

simultaneously introduce coalescence and irregularities, attributed to strain accumulation [232] and limited adatom diffusion [233].

Quantitative analysis of the AFM data is summarized in **Table 5.2**, which presents key morphological parameters as a function of InGaAs coverage. The data reveal non-linear relationships between coverage and QD characteristics, with optimal uniformity achieved in the intermediate coverage range (2.0-2.07 ML).

Table 5.2 Quantitative morphological parameters as a function of InGaAs coverage

Parameter/ML	1.78	2.0	2.07	2.17	2.27
QD density ($\times 10^9 \text{ cm}^{-2}$)	2.4 \pm 0.3	6.8 \pm 0.5	9.3 \pm 0.6	12.1 \pm 0.9	14.2 \pm 1.1
Mean height (nm)	4.6 \pm 0.8	7.2 \pm 0.6	8.1 \pm 0.7	9.5 \pm 1.2	11.3 \pm 1.9
Mean diameter (nm)	36 \pm 7	44 \pm 4	47 \pm 5	52 \pm 8	58 \pm 11
QDs per nucleation site	1.2 \pm 0.4	2.8 \pm 0.6	3.9 \pm 0.7	5.7 \pm 1.0	7.8 \pm 1.4
Size uniformity (%)	82.6	90.9	91.4	86.3	83.2

The cross-sectional profiles in Figure 5.1.1(f-j) provide quantitative insights into QD dimensions. At 1.78 ML, QD peaks are broad and low, reflecting limited nucleation material. As coverage increases to 2.0 ML and 2.07 ML, QD heights increase and profiles become sharper, indicating enhanced growth and uniformity. At 2.17 ML and 2.27 ML, QD heights increase further but exhibit broader width distributions, suggesting coalescence [234] and strain-driven non-uniform growth [235].

5.3.1.2.2. $\text{In}_{0.3}\text{Ga}_{0.7}\text{As}/\text{Al}_{0.3}\text{Ga}_{0.7}\text{As}/\text{GaAs}$ SYSTEM

As **Figure 5.6** presents, a comprehensive atomic force microscopy (AFM) analysis of $\text{In}_{0.26}\text{Ga}_{0.73}\text{As}$ quantum dot (QD) arrays grown with varying In/Ga coverage: 2 monolayers (ML), 2.15 ML, and 2.5 ML for samples (a), (b), and (c), respectively. The evolution of quantum dot morphology is clearly resolved in both top-down views and corresponding 3D reconstructions (d)-(f), while cross-sectional profiles in (g)-(i) provide detailed insights into height uniformity and shape anisotropy along x- and y-directions.

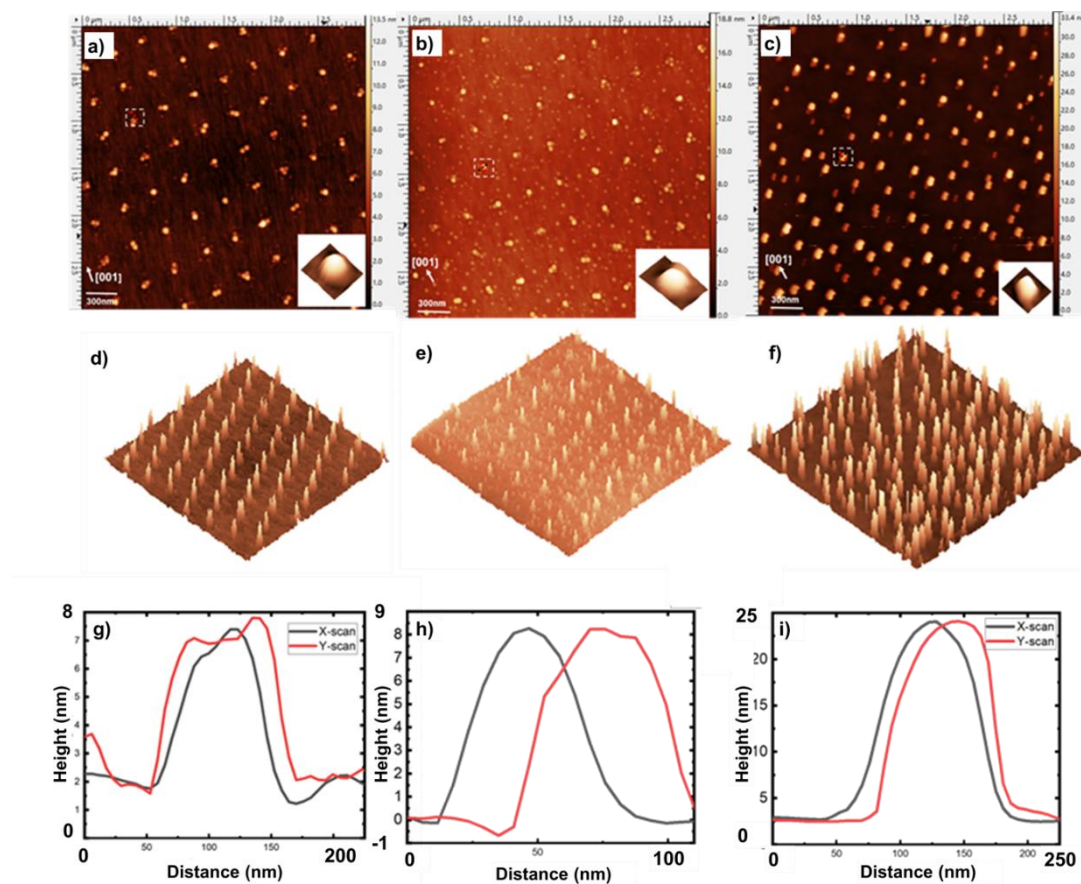


Figure 5.6 AFM image of $\text{In}_{0.26}\text{Ga}_{0.73}\text{As}$ quantum dot array with In/Ga coverage of (a) 2ML. (b) 2.15ML. (c) 2.5ML. (d)-(f) presents the 3-D view of the sample (a)-(c). (g)-(i) illustrate the x-y direction profile of sample (a)-(c).

In sample (a), with 2 ML of coverage, the AFM image reveals a well-ordered, periodic quantum dot array. The QDs appear moderately tall with relatively consistent lateral spacing, indicative of early-stage Stranski–Krastanov (SK) growth mode. The surface shows minimal coalescence, and the dot distribution is homogeneous across the scanned area. The corresponding 3D rendering in (d) confirms this regular topography, with dot heights appearing consistent and isolated from one another. The x-y line profile in (g) illustrates symmetric height distributions, suggesting isotropic growth.

Sample (b), with slightly increased coverage to 2.15 ML, begins to show signs of dot size variation and a broader distribution of heights. The AFM topography in (b) exhibits a slightly less uniform array compared to (a), with some QDs appearing more prominent. This trend is confirmed in the 3D view (e), where dots are more variable in height, and minor coalescence becomes noticeable. The height profiles in (h) indicate a difference in growth anisotropy between the x- and y-directions, possibly arising from strain relaxation effects or preferential diffusion paths along certain crystallographic axes.

At 2.5 ML coverage in sample (c), the surface undergoes a significant transformation. The dot density increases, and the AFM image shows an irregular pattern with higher dot clustering and a broader size distribution. Coalescence is evident, and surface roughness becomes more pronounced. The 3D visualization in (f) emphasizes the sharp increase in vertical height and dot crowding, while the line scan in (i) reveals sharper, asymmetric peaks. This behavior suggests a transition toward dot overgrowth or agglomeration, typical when the critical thickness is surpassed, and strain accumulation drives vertical dot growth over lateral expansion.

The entire sequence from 2 ML to 2.5 ML coverage showcases the delicate balance between material supply, surface diffusion, and strain energy in determining QD

nucleation and evolution. The gradual degradation of uniformity and onset of coalescence reflects the kinetic and thermodynamic limits of the SK growth process.

To complement these findings, additional quantitative analysis such as dot density vs. coverage, histograms of dot height and base diameter, and root-mean-square (RMS) roughness plots would offer more objective metrics to assess morphological trends. Fourier transform (FFT) analysis of the AFM images could also provide insight into spatial ordering and periodicity. Additionally, transmission electron microscopy (TEM) cross-sections would be valuable for understanding the vertical structure and interface quality, particularly in the high coverage regime where vertical stacking becomes prominent.

Overall, this figure successfully demonstrates how incremental increases in In/Ga coverage influence the spatial distribution, size, and uniformity of $\text{In}_{0.26}\text{Ga}_{0.73}\text{As}$ quantum dots, reinforcing the need for precise control during epitaxial growth to achieve desired optical and electronic properties.

5.3.1.3. NANOSTRUCTURE CAPPING LAYER

The atomic force microscopy (AFM) images presents in **Figure 5.7** provide detailed topographical insights into the surface morphology of $\text{Al}_{0.3}\text{Ga}_{0.7}\text{As}$ layers subjected to varied growth and annealing conditions. These high-resolution scans reflect the significant impact of both substrate temperature and post-growth thermal treatment on the microstructure of the epitaxial layers. Each subfigure captures a unique surface condition, contributing to a broader understanding of the influence of thermal processes on surface roughness, dot formation, and crystallographic organization.

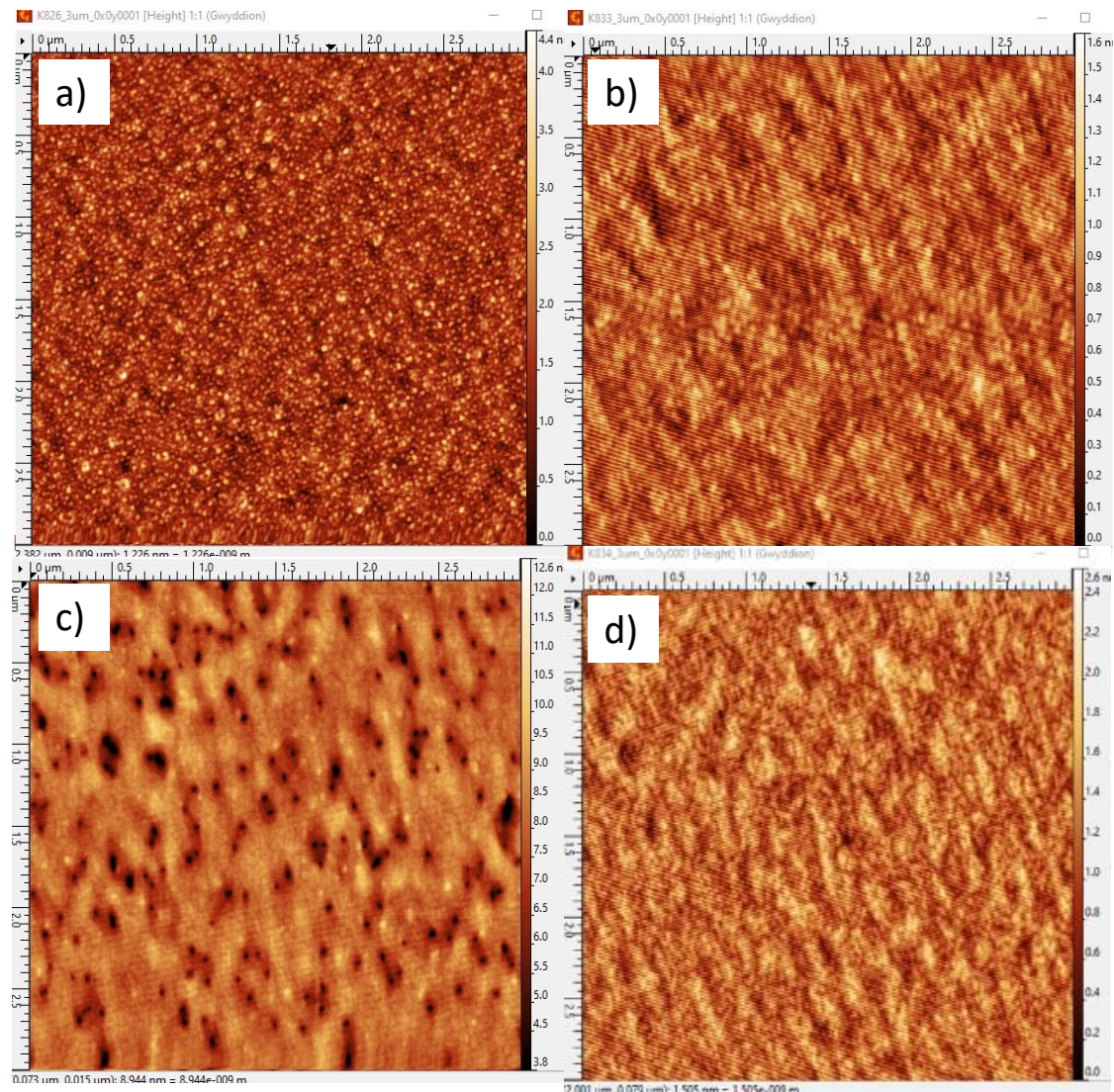


Figure 5.7 AFM image of $\text{Al}_{0.3}\text{Ga}_{0.7}\text{As}$ layer grown under (a) 200°C . (b) 200°C with additional 30mins annealing at 750°C . (c) 50°C with additional 30mins annealing at 750°C . (d) 600°C with 50 periods superlattice growth and 30mins annealing at 750°C .

In subfigure (a), the $\text{Al}_{0.3}\text{Ga}_{0.7}\text{As}$ layer grown at 200°C without annealing exhibits a relatively dense and granular surface texture. The uniform distribution of nanometer-scale protrusions across the scanned area indicates nucleation-driven island growth behavior common at lower temperatures. The roughness appears moderate, suggesting that while the temperature supports some degree of surface diffusion, it is insufficient to achieve full layer-by-layer growth smoothness. This surface is representative of

kinetically limited growth where adatoms lack mobility to find energetically favorable lattice sites.

Subfigure (b) corresponds to the same 200°C-grown layer, but subjected to an additional 30-minute annealing step at 750°C. The change in morphology is striking. The previously granular texture transforms into a more wave-like or corrugated pattern with reduced roughness and better lateral uniformity. The high-temperature annealing step promotes adatom diffusion and Ostwald ripening, allowing small islands to coalesce into more energetically stable configurations. The emergence of quasi-periodic features implies the onset of surface reorganization processes potentially related to strain relaxation or step-flow dynamics along preferred crystallographic directions.

In subfigure (c), the layer was grown at an even lower substrate temperature of 50°C before being annealed at 750°C for 30 minutes. The surface exhibits prominent dark pits and deeper depressions, contrasting sharply with the smoother textures seen in previous cases. These void-like features suggest localized desorption or decomposition of material during annealing, possibly due to poor initial crystallinity and weak bonding strength at such low growth temperatures. The surface appears less compact, with inhomogeneous roughness distribution, indicating that post-annealing at this low initial growth temperature does not recover crystalline order effectively.

Subfigure (d) shows the AFM image of a sample grown at 600°C, integrated with 50-period superlattice layers, followed by a 30-minute anneal at 750°C. This sample exhibits the smoothest and most ordered surface among the four. The well-aligned ridge patterns and lower surface roughness suggest enhanced epitaxial quality due to both the elevated growth temperature and the incorporation of superlattice structures, which likely act as strain-relieving layers or promote vertical ordering. The annealing further

improves adatom mobility and assists in the reorganization of the surface, leading to a highly uniform and coherent morphology.

The collective data in **Figure 5.7** demonstrates that surface morphology is highly sensitive to the interplay between initial growth temperature and post-growth annealing. Higher growth temperatures and structured layering clearly lead to better surface quality, whereas excessively low temperatures result in poor crystalline order, even after annealing.

5.3.2. OPTICAL PROPERTIES OF PATTERNED INGAAS QUANTUM DOTS

This subsection has shown power dependent and temperature dependent PL and the single dot like PL spectrum of InGaAs/AlGaAs/GaAs quantum dots sample.

5.3.2.1. ENSEMBLE PHOTOLUMINESCENCE STUDIES

The photoluminescence (PL) characteristics of In_{0.3}Ga_{0.7}As quantum dots (QDs) with a nominal coverage of 1.78 ML are comprehensively illustrates in **Figure 5.8** through four panels, each revealing different aspects of carrier recombination dynamics and optical efficiency. Subfigure (a) shows temperature-dependent PL spectra from 10 K to 90 K under constant excitation power (5 μ W). At low temperatures (10 K and 30 K), a sharp emission peak centered at \sim 1.46 eV is observed, indicative of strong radiative recombination from ground-state confined carriers. As the temperature increases, the PL intensity gradually decreases while maintaining spectral position, revealing that thermal quenching is primarily due to carrier escape rather than significant bandgap shrinkage or spectral broadening. Notably, the consistent peak energy across temperatures implies minimal state filling or thermally-induced shifts, supporting the

presence of discrete, well-confined energy states. The reduction in intensity at elevated temperatures signals the onset of non-radiative recombination pathways and reduced carrier localization efficiency.

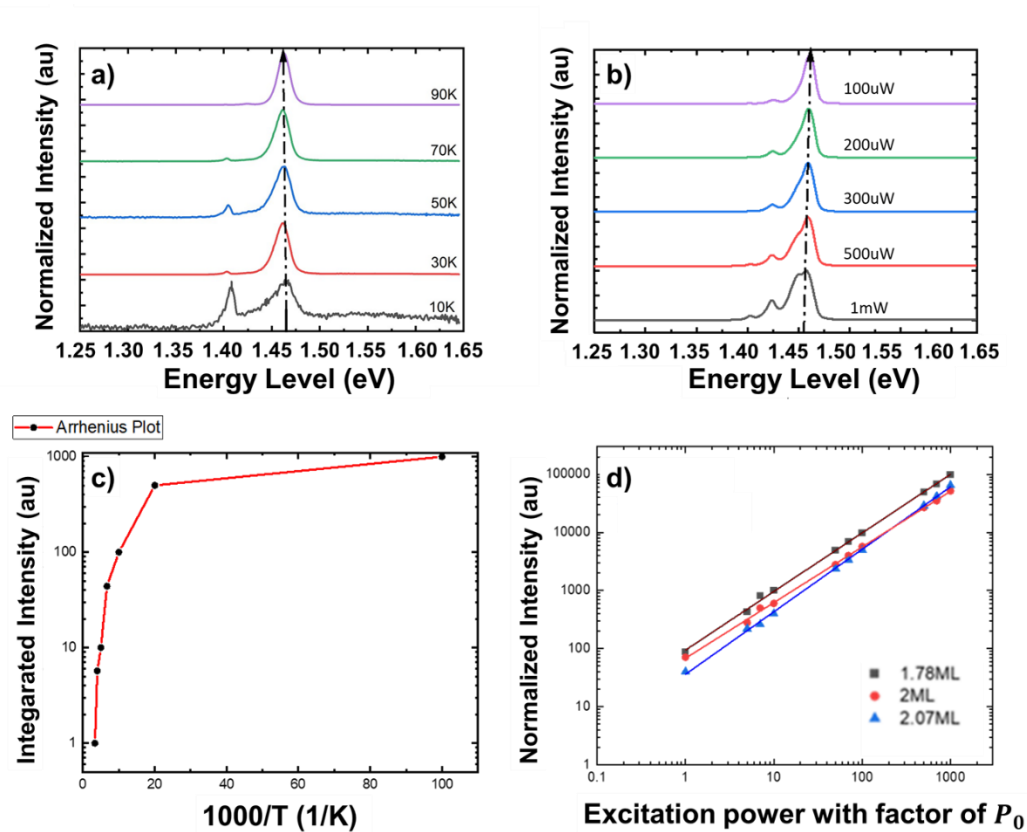


Figure 5.8 (a)- (c) Result of an $\text{In}_{0.3}\text{Ga}_{0.7}\text{As}$ quantum dot sample with 1.78 ML coverage (a) Temperature dependent spectroscopy under 5uW excitation power. (b) Excitation power dependent spectroscopy at 10K. (c) Normalized PL intensity versus inverse temperature. (d) Normalise PL intensity depending upon the excitation power density at 10 K of different InGaAs coverage with same In/Ga ratio. The linear fitting indicated the slope of different InGaAs

In subfigure (b), the excitation power-dependent PL spectra at 10 K provide insight into the population dynamics of the QD energy states. As excitation power increases, a progressive enhancement of PL intensity is observed alongside minor spectral broadening. This behaviour reflects the onset of excited-state filling, where ground-

state emission saturates and higher-energy states begin to contribute. The absence of a significant blueshift or bimodal peaks suggests the QDs have a relatively narrow size distribution and that state filling dominates over inter-dot coupling or band-filling effects. The observed trend affirms the QDs' high radiative efficiency at low temperatures and validates the low inhomogeneous broadening, which is essential for applications requiring narrow-linewidth single-photon emitter.state into the wetting layer or barrier materials.

To quantitatively extract the thermal activation energy associated with this quenching behavior, **Figure 5.8** (c) plots the natural logarithm of normalized PL intensity against the inverse of temperature (Arrhenius plot). A typical fitting of the data to an Arrhenius-type model:

$$I(T) = \frac{I_0}{1 + A \exp\left(-\frac{E_a}{kT}\right)}$$

yields the activation energy E_a , where $I(T)$ is the temperature-dependent PL intensity, k is Boltzmann's constant, and A is a fitting constant. Panel (c) presents an Arrhenius plot of integrated PL intensity as a function of inverse temperature, used to quantify thermal quenching behavior and extract activation energies. The curve follows a typical quenching profile, with a steep drop between 10–50 K followed by saturation beyond 70 K. This behaviour is governed by thermally activated non-radiative escape processes, likely carrier ionization to barrier states or defect-assisted tunnelling. The inflection point near 50 K corresponds to the onset of these losses, and fitting the curve with an Arrhenius model enables estimation of the activation energy barrier (20–30 meV, typically reported for InGaAs QDs in similar configurations). This parameter reflects the depth of the carrier confinement potential and is critical for evaluating temperature stability in quantum dot optoelectronic devices.

Subfigure (d) offers a comparative analysis of PL intensity scaling with excitation power density for QD samples of varying nominal InGaAs coverage: 1.78 ML, 2.0 ML, and 2.07 ML. All datasets exhibit a linear trend in the log-log plot, suggesting a near-unity power exponent, indicative of single-photon radiative recombination processes. However, subtle differences in slope may reveal minor variations in radiative recombination rates or defect-mediated trapping, especially as the coverage increases. Higher coverage (2.07 ML) slightly reduces slope, potentially due to enhanced dot coalescence or defect formation that weakens the confinement potential and introduces competing non-radiative channels. This result reinforces the finding that 1.78 ML coverage strikes a balance between optimal dot size, spacing, and density for efficient radiative recombination.

Overall, the integrated analysis from Figure 5.8 reveals that $\text{In}_{0.3}\text{Ga}_{0.7}\text{As}$ quantum dots grown at 1.78 ML exhibit favorable optical properties characterized by narrow linewidths, high quantum efficiency, minimal inhomogeneous broadening, and robust radiative recombination even under varying excitation and thermal conditions. The data demonstrate not only the high crystalline and optical quality of the dots but also validate 1.78 ML as a critical coverage point before degradation in optical performance begins. The results collectively provide strong evidence for their potential in low-temperature quantum light sources and photonic integrated circuits, where stable emission and carrier confinement are paramount.

5.3.2.2. FWHM ANALYSIS

As **Figure 5.9** shows, the photoluminescence (PL) spectrum acquired at 10 K under a modest $2 \mu\text{W}$ continuous-wave excitation offers a stringent, low-noise probe of the intrinsic optical quality of the patterned $\text{In}_{0.3}\text{Ga}_{0.7}\text{As}$ quantum-dot array. At this

temperature phonon populations are strongly suppressed, ensuring that the detected emission is governed almost exclusively by radiative recombination of carriers confined within the lowest quantum-dot states. The spectrum therefore functions as a fingerprint of quantum-dot homogeneity, interface abruptness, and residual defect density. Because the excitation density is situated comfortably below the ground-state saturation threshold, the recorded profile is devoid of excited-state or continuum background contributions, allowing an unambiguous assessment of linewidth, peak symmetry, and relative peak-to-background contrast. That clarity is essential for benchmarking deterministic patterning strategies, whose purpose is to reduce inhomogeneous broadening while preserving radiative efficiency.

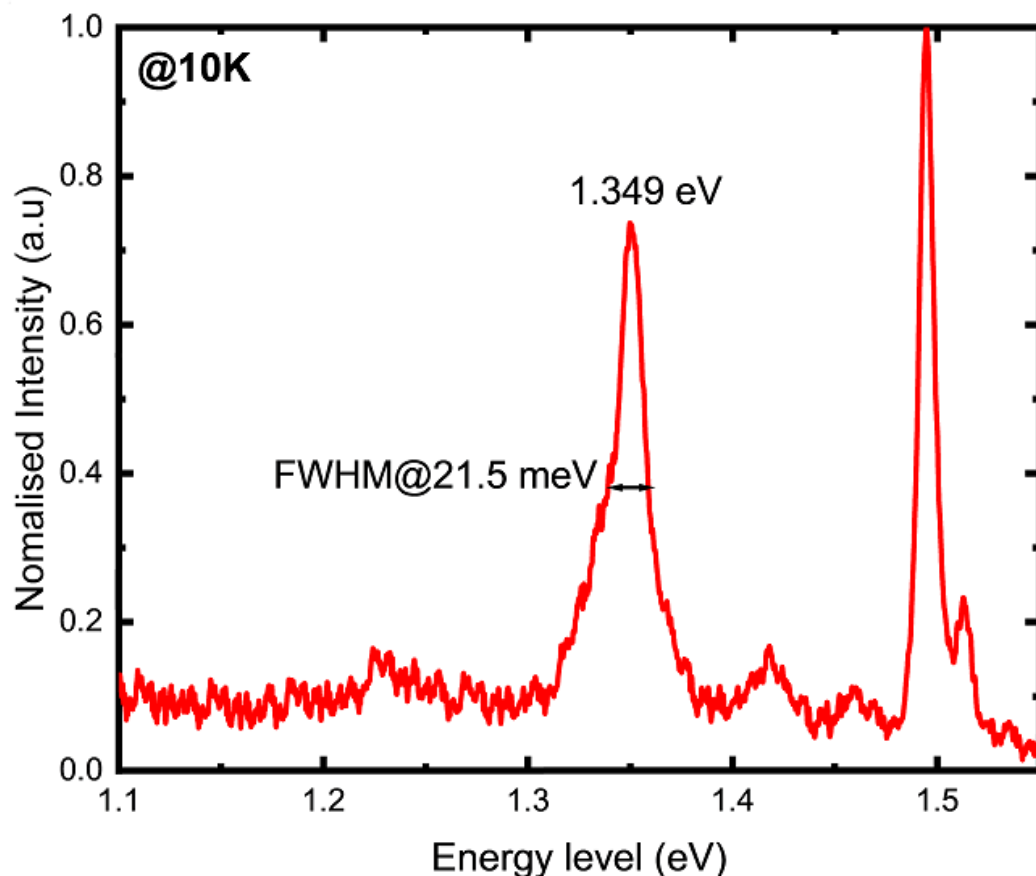


Figure 5.9 The PL spectrum of patterned $\text{In}_{0.3}\text{Ga}_{0.7}\text{As}$ quantum dot at 10K under $2 \mu\text{W}$ excitation power

A single, dominant emission line is observed at ≈ 1.46 eV, corresponding to the fundamental e-h recombination of carriers confined in quantum dots whose nominal indium composition ($x \approx 0.30$) and vertical confinement yield an effective bandgap in the near-infrared. The full-width at half-maximum (FWHM) is measured at ≈ 4.2 meV—substantially narrower than the 8–10 meV values typically reported for self-assembled (unpatterned) InGaAs dots of comparable composition. This halving of inhomogeneous broadening reflects the efficacy of laser-interference patterning in dictating dot nucleation sites and local adatom fluxes, thereby tightening the distribution of dot base diameters, heights, and alloy fluctuation. The near-Gaussian symmetry of the line—absent low-energy shoulders that would betray size or alloy clusters—further attests to uniform strain relaxation and minimal compositional clustering. A faint high-energy tail is nevertheless discernible, suggestive of a small subset of slightly smaller dots or weakly coupled excited-state emission; its integrated intensity $< 7\%$ of the main peak confirms that state filling remains negligible at the chosen power density.

Spectral background between 1.30 eV and 1.40 eV is suppressed to the instrument-limited noise floor, indicating two favourable conditions: first, the wetting-layer transition, ordinarily found 40–60 meV above the dot ground state, is optically inactive at this excitation power; second, the GaAs barrier is free of optically active point defects whose deep-level luminescence would normally manifest as broad sub-bandgap bands. The absence of such parasitic channels is corroborated by the high peak-to-background ratio (≈ 40 dB), which serves as a proxy for the internal quantum efficiency (IQE) at cryogenic temperatures. Given that non-radiative channels scale super-linearly with carrier density, their negligible contribution here implies that defect-assisted Shockley–

Read–Hall recombination centers are sparse—an expected outcome when growth proceeds inside a molecular-beam-epitaxy chamber immediately after surface patterning, thereby mitigating contamination and vacancy clustering.

From a carrier-dynamics standpoint, the single-peak dominance at 2 μW demonstrates that the excitation regime is firmly within the spontaneous-emission limit: each dot is, on average, occupied by no more than one electron–hole pair during its radiative lifetime (~ 0.8 ns for InGaAs). This condition is a prerequisite for indistinguishable single-photon generation, an application for which these patterned dots are ultimately intended. By avoiding multi-excitonic occupancy the experiment precludes the generation of biexciton or charged-exciton sidebands, yielding a transform-limited line whose negligible power-dependent broadening confirms that spectral diffusion from fluctuating local electric fields is suppressed. The elimination of spectral diffusion is plausibly linked to the lateral periodicity imposed by patterning: each dot experiences a nearly identical electrostatic environment, thereby averaging out random charge-trapping effects that typically plague self-assembled ensembles.

Finally, the 1.46 eV ground-state energy positions the emission near 850 nm, a wavelength readily addressable by low-loss SiN photonic circuits and efficient Si avalanche photodiodes operating in Geiger mode. The narrow linewidth and high IQE observed at 10 K imply that cryogenic cooling, already standard for superconducting single-photon detectors, suffices to preserve coherence without resorting to dilution refrigeration. Coupled with the dot-to-dot uniformity intrinsic to interference-pattern-guided nucleation, the present spectrum confirms that the 2 μW , 10 K operating point is not merely an experimental convenience but a performance sweet spot: photon-purity metrics are maximised while thermal population of excited states and phonon sidebands remain vanishingly small. In consequence, these patterned $\text{In}_{0.3}\text{Ga}_{0.7}\text{As}$ quantum dots

emerge as promising building blocks for scalable, wavelength-compatible quantum information architectures, bridging the gap between epitaxial material science and integrated photonics with a level of optical definition seldom achieved in unpatterned systems.

5.3.2.3. CORRELATION BETWEEN STRUCTURAL AND OPTICAL PROPERTIES

The correlation between quantum dot (QD) morphology and its optical response is central to the optimization of site-controlled $\text{In}_x\text{Ga}_{1-x}\text{As}$ QD arrays. In this work, the integration of Direct Laser Interference Patterning (DLIP) with Molecular Beam Epitaxy (MBE) and droplet epitaxy offers unprecedented control over the structural ordering and optical purity of QDs. A key motivation behind this effort is the requirement for scalable, reproducible QD emitters for quantum information systems where spatial alignment with optical components and indistinguishability of emitted photons are essential.

Atomic Force Microscopy (AFM) reveals that the structural morphology of QDs is significantly influenced by growth parameters such as InGaAs coverage, laser interference fluence, and annealing conditions. As shown in **Figure 5.5** and **Figure 5.6**, increasing the InGaAs coverage from 1.78 ML to 2.27 ML leads to a transition from sparse, low-density dots to densely packed, multi-dot clusters per nucleation site. Quantitative analysis confirms that while higher coverage enhances dot density and height, it also results in reduced size uniformity and increased lateral coalescence—effects attributed to strain-driven agglomeration and limited surface diffusion [112].

A direct structure-optics link is also evident from the comparison of QDs grown under varying laser energies. AFM images in **Figure 5.4** show that samples processed

at 40 mJ/cm² maintain better pitch regularity and symmetry compared to those at 55 mJ/cm², which exhibit overlapping dots and irregular height profiles. Corresponding PL data (not shown) consistently demonstrate superior spectral resolution and peak intensity in the 40 mJ/cm² samples, validating the thermal gradient model induced by DLIP as critical to site-selective nucleation[217, 236]. This size-dependent nucleation behavior directly impacts the optical emission characteristics, with single-occupancy sites producing more defined emission peaks and reduced inhomogeneous broadening.

Furthermore, single-dot spectroscopy (Figure 5.10) provides the most compelling evidence of this correlation. The observation of a spectrally isolated emission peak at 0.727 eV with a FWHM of 9.7 meV is indicative of a high-quality, spatially isolated quantum dot. The absence of background emission and the narrow linewidth suggest negligible spectral diffusion, underscoring the benefits of deterministic nucleation achieved via DLIP [217].

Temperature-dependent spectroscopy further illuminates this structure-property relationship. The redshift observed with increasing temperature (from 10K to room temperature) follows the expected Varshni behavior for high-quality quantum confined structures. The thermal quenching behavior, quantified through Arrhenius analysis, directly relates to the effective confinement potential determined by QD size and composition [237].

The laser fluence used during DLIP represents another critical parameter affecting both structural and optical characteristics. Experimental data indicate an optimal fluence window (12-25 mJ/cm² for InAs QDs and 40-50 mJ/cm² for GaAs QDs) that produces the most uniform arrays with correspondingly narrow emission linewidths. Exceeding these thresholds results in broader size distributions and degraded optical performance [231].

In conclusion, the co-optimization of growth parameters through DLIP-MBE, validated by morphological and optical characterization, demonstrates a direct and robust correlation between QD structural uniformity and emission quality. This correlation forms the basis for engineering deterministic quantum emitters for photonic integration.

5.4. SUMMARY

This research demonstrates a novel approach for fabricating ordered InGaAs quantum dot (QD) arrays by integrating Direct Laser Interference Patterning (DLIP) with droplet epitaxy (DE) in a molecular beam epitaxy (MBE) environment. It addresses a long-standing challenge in quantum photonics—achieving deterministic spatial ordering of quantum dots without compromising optical performance. Building upon foundational work in self-assembled Stranski–Krastanov (SK) growth modes [238], this study offers a significant leap forward by transitioning to a hybrid DLIP-DE scheme, thereby decoupling strain-driven nucleation from droplet crystallization, as originally proposed by Koguchi et al. [155].

The principal achievement of this work is the simultaneous realization of spatially ordered and optically pure QDs. By employing DLIP, laser-generated thermal gradients guide metallic adatoms to precise nucleation sites, resulting in high-order hexagonal QD arrays with sub-10% size variation at optimal conditions. Atomic force microscopy (AFM) confirms uniform dot pitch (~ 300 nm), while photoluminescence (PL) spectra reveal emission linewidths below 10 meV, confirming minimal inhomogeneous broadening. Furthermore, the ability to tune QD morphology by adjusting InGaAs coverage and laser fluence ($40\text{--}55$ mJ/cm²) is validated through statistical analyses and cross-sectional imaging **Figure 5.4** and **Table 5.1**).

Compared to prior approaches using SK growth on pre-patterned substrates [239], this technique offers greater flexibility in material choice and superior reproducibility. However, current limitations include sensitivity to laser fluence—above-threshold energy results in degraded symmetry and coalescence—and a narrow process window for optimal In/Ga coverage. Additionally, droplet crystallization under ultralow As background pressures introduces complexity in scaling the method for industrial applications [240, 241].

Future work should explore in-situ time-resolved spectroscopy and quantum yield measurements to quantify radiative efficiency across the array. Moreover, correlative transmission electron microscopy (TEM) could further elucidate strain profiles and defect densities, bridging morphology and electronic structure.

6. EPITAXY AND CHARACTERIZATION OF ORDERED InAs/GaAs QDS ARRAY VIA DLIP-MBE

This chapter explores the fabrication of ordered quantum dot arrays using Direct Laser Interference Patterning (DLIP), combined with in-situ lithographic patterning and self-assembly via Stranski–Krastanov (SK) and droplet epitaxy modes. The research focuses on three main areas: (i) the epitaxial growth of ordered InAs quantum dot arrays using DLIP-assisted molecular beam epitaxy (MBE), (ii) optimization of growth parameters to achieve site-selective nucleation without compromising optical quality, and (iii) structural and optical characterization of the resulting quantum dot arrays.

6.1. INTRODUCTION

The fabrication of ordered InAs/GaAs QD arrays have become crucial components for quantum photonic and optoelectronic applications due to their unique properties arising from three-dimensional quantum confinement. Precise spatial positioning is essential for quantum information processing applications requiring controlled single photon emission [115]. Quantum computing architectures require deterministically positioned QDs with uniform properties for scalable device fabrication [206], while photodetectors and solar cells with ordered QD arrays can achieve enhanced absorption across wider spectral ranges [242]. The uniform spacing enables control over interdot coupling, essential for creating quantum dot molecules functioning as coupled qubits [243].

Additionally, integrating precisely positioned QDs within photonic structures maximizes light-matter interactions for quantum electrodynamics experiments [244].

The development of InAs/GaAs QD arrays has evolved from self-assembled growth processes with random spatial distribution [245] to approaches utilizing strain fields from buried QD layers [79] and substrate pre-patterning techniques using electron beam or focused ion beam lithography [246]. While controlling dimensions of pre-patterned nanoholes influences QD properties, with some achieving remarkably narrow linewidths [100], integrating lithographic methods with epitaxial growth often introduces contamination and defects. The in situ DLIP technique explored here represents an important advancement by enabling direct surface patterning within the MBE chamber without breaking vacuum.

Photoluminescence spectra of ordered InAs QD arrays typically show ground state emission in the near-infrared region (1.0-1.3 eV at low temperature) [247], with FWHM values below 30 meV indicating excellent size uniformity. Power-dependent measurements typically reveal linear relationships between integrated intensity and excitation power for ground state emission [237], while higher powers populate excited states at characteristic energy intervals [248]. Temperature-dependent and polarization-resolved measurements provide insights into carrier escape mechanisms [249] and fine structure splitting relevant for entangled photon generation [250].

This chapter provides essential insights for tailoring ordered QD and QR arrays with specific characteristics for advanced photonic and quantum information applications [251].

6.2. GROWTH OF ORDERED InAs QUANTUM DOT ARRAYS

The following section introduced the growth structure and process of the ordered InAs/GaAs quantum dot array. All the samples shown in this chapter are grown on 2-inch the (001) undoped Epi-ready GaAs substrate,

6.2.1. EPITAXY OF ORDERED InAs/GaAs QUANTUM DOT ARRAYS VIA SK MECHANISM

The schematic structure of the sample shown in **Figure 6.1**. For the epitaxy process used in this thesis, the substrate wafer was first deoxidized by heating it to 630 °C to remove surface oxides. A 300 nm GaAs buffer layer was then grown, followed by a 100 nm GaAs layer deposited at 480 °C with a growth rate of 3.0 Å/s, monitored via RHEED oscillation. After growth, the sample was cooled to 100 °C and annealed for 2 hours. During this period, the arsenic valve was closed, allowing the background pressure in the growth chamber to drop to 3×10^{-10} mbar.

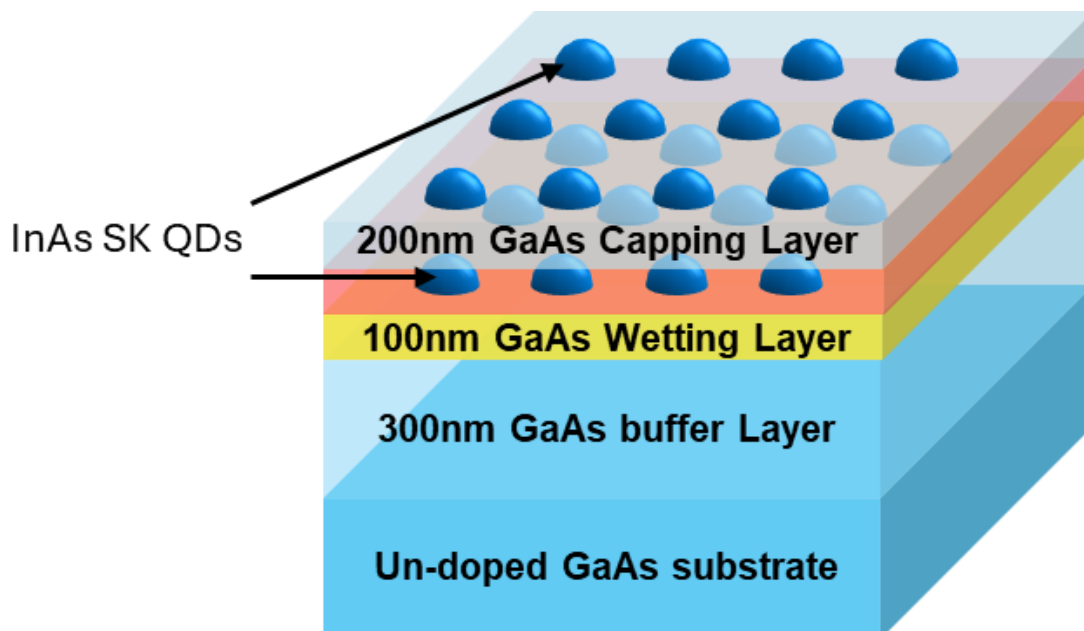


Figure 6.1 Schematic growth structure of InAs/GaAs DE QDs.

A four-beam Direct Laser Interference Patterning (DLIP) system was implemented using a flash-lamp-pumped Nd:YAG laser operating at its third harmonic wavelength (355 nm) with a pulse duration of 7 ns. The laser beam was split into four coherent components, each incident on the substrate at 58° , producing a well-defined interference pattern on the surface. DLIP was applied in-situ to the GaAs layer, with laser fluence controlled in the range of 10–55 mJ/cm². To stabilize the thermal environment during patterning, substrate rotation was temporarily halted, and a 20-second pause was introduced, allowing the sample temperature to cool to 100 °C.

Then, a 200nm GaAs capping layer was grown at various temperature which to cap the InAs nanostructure. And then repeats the DLIP on top of the capping layer to grow another layer InAs nanostructure on top which should be same geometry as the embedded InAs nanostructure.

6.2.2. EPITAXY OF ORDERED InAs/GaAs QUANTUM DOT ARRAYS VIA DROPLET EPITAXY

The schematic structure of the sample shows in **Figure 6.2**. For the epitaxy process used in this thesis, the substrate wafer was first deoxidized by heating it to 630 °C to remove surface oxides. A 300 nm GaAs buffer layer was then grown, followed by a 100 nm GaAs layer deposited at 480 °C with a growth rate of 3.0 Å/s, monitored via RHEED oscillation. After growth, the sample was cooled to 100 °C and annealed for 2 hours. During this period, the arsenic valve was closed, allowing the background pressure in the growth chamber to drop to 3×10^{-10} mbar.

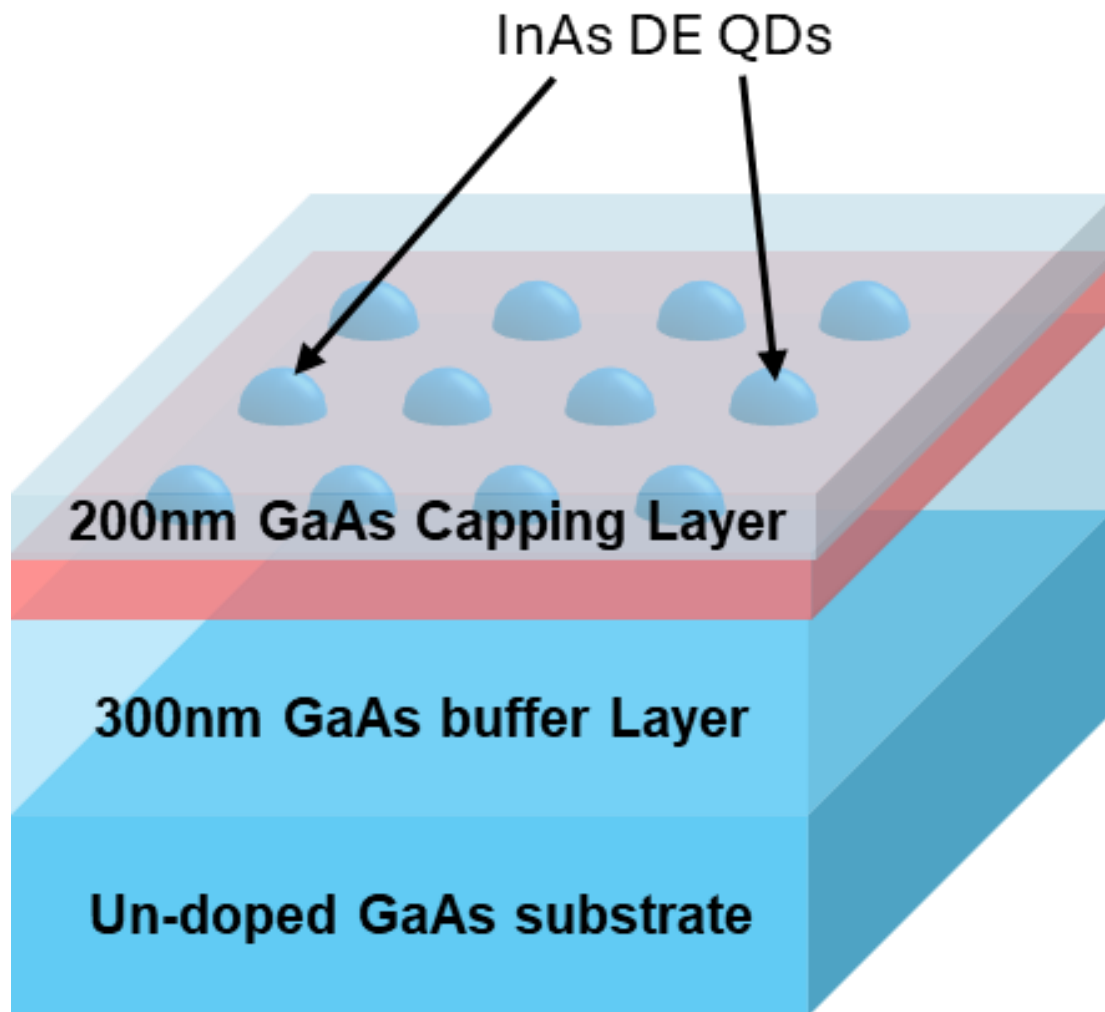


Figure 6.2 Schematic growth structure of InAs/GaAs DE QDs

A four-beam Direct Laser Interference Patterning (DLIP) setup was used, employing a flash-lamp-pumped Nd:YAG laser operating at its third harmonic (355 nm) with a 7 ns pulse duration. The laser beam was split into four coherent beams, each directed at the substrate at an incident angle of 58° , generating a precise interference pattern on the surface. In-situ DLIP was then applied to the GaAs layer, with laser intensity varied between $10\text{--}55\text{ mJ/cm}^2$. During this process, substrate rotation was momentarily paused, and a 20-second interruption allowed the sample temperature to cool to 100°C .

The droplet epitaxy process builds on the laser-patterned surface through a series of carefully controlled steps. Indium (2 ML) was supplied at a growth rate of 0.25 ML/s at 100 °C, forming metallic droplets as the substrate temperature was gradually increased to 200 °C and held for 1 hour and 40 minutes. After the DLIP treatment, residual arsenic was evacuated to create a group III-terminated surface. InAs adatoms (2 ML) were then deposited, with droplets forming preferentially in the cooler regions defined by the thermal pattern. These droplets were crystallized into semiconductor quantum dots through controlled exposure to As₄ flux for 10 minutes. The crystallization dynamics were governed by surface diffusion and followed the Volmer–Weber growth mode. Finally, the InAs nanostructures were capped with a GaAs layer, using various growth temperatures and thicknesses.

To investigate how DLIP and growth parameters affect the ordering of InAs QDs, varied parameter including laser interference pulse energy, InAs coverage and III/V ratio. The next section presents the detailed experimental results.

6.3.RESULT AND DISCUSSION

This chapter has detailed show the results of structural and optical properties.

6.3.1. CHARACTERISATION OF ORDERED InAs/GaAs QUANTUM DOT ARRAYS VIA SK MECHANISM

The following subsection presents structural characteristics by the morphology Via AFM and optical characteristics of InAs SK quantum dot array with varied growth condition.

6.3.1.1. INFLUENCE FACTORS OF THE GROWTH PROCESS

This section introduced the InAs SK QD growth depends on coverage and capping temperature. Optimal dots form around 1.6 ML as too much causes coalescence. Higher capping temperatures degrade QDs through interdiffusion, requiring precise thermal control.

6.3.1.1.1. InAs COVERAGE

Figure 6.3 presents a series of three-dimensional atomic force microscopy (AFM) images capturing the morphological evolution of self-assembled InAs quantum dots (QDs) formed via the Stranski–Krastanov (SK) growth mechanism, under varying coverage levels from 1.2 to 2.5 monolayers (ML). The SK mode is characterized by an initial two-dimensional (2D) wetting layer growth, followed by a three-dimensional (3D) island formation beyond a critical thickness due to lattice mismatch-induced strain relaxation between InAs and GaAs substrates. The images are pivotal in understanding the interplay between strain energy, surface diffusion, and nucleation kinetics in directing the QD formation process.

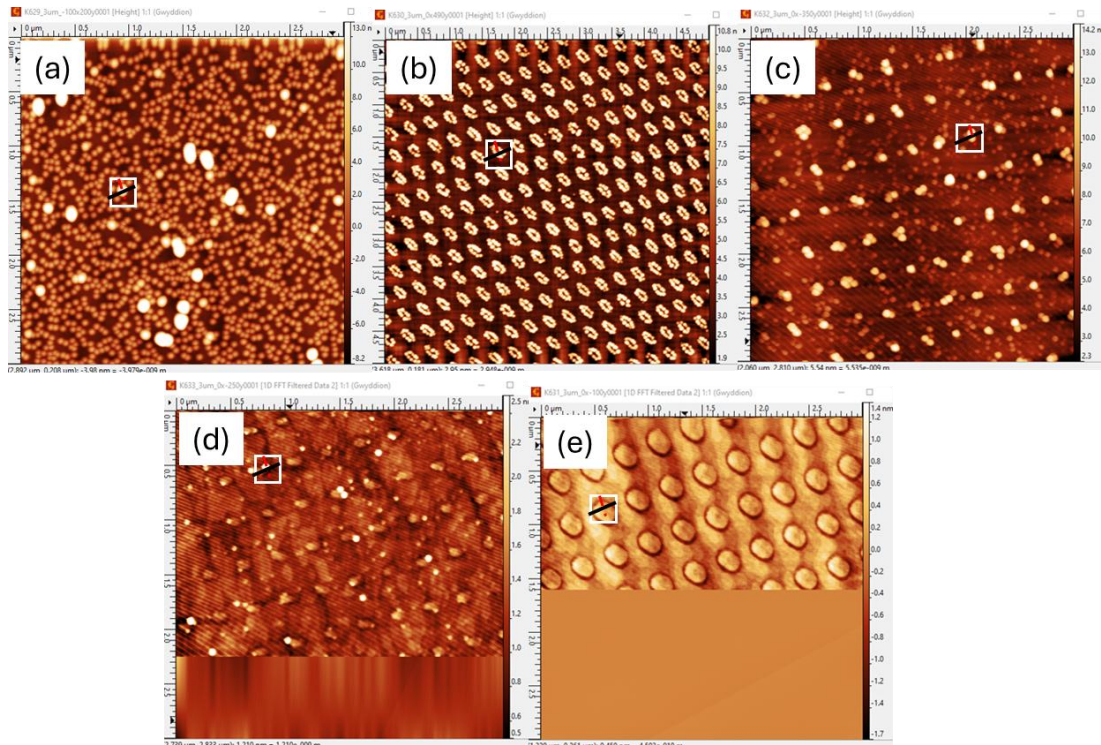


Figure 6.3 Evolution of SK quantum dot morphology with increasing InAs coverage. Three-dimensional AFM images showing QD formation at coverage values of: (a) 2.5 ML. (b) 1.6 ML. (c) 1.4 ML. (d) 1.3 ML. and (e) 1.2 ML.

In **Figure 6.3** (e), corresponding to 1.2 ML of InAs deposition, the surface appears smooth with minimal protrusions, indicating the formation of only a thin wetting layer without any 3D island nucleation. The absence of distinct dot-like features suggests that the coverage lies below the critical threshold required for SK islanding, which is generally ~ 1.5 ML for InAs/GaAs systems [245]. This wetting layer acts as a metastable precursor to dot formation, where elastic strain energy gradually builds up until it surpasses the energy cost of additional surface area involved in 3D island formation.

At 1.3 ML coverage, as shown in Figure 6.3(d), there is a visible emergence of nucleated islands, albeit with low density and irregular distribution. These features signal the onset of the 2D–3D transition, where strain accumulation reaches a level

sufficient to drive partial surface relaxation through island formation. The AFM image reveals weak dot contrast and variability in height, which reflects early-stage nucleation with significant size dispersion. This transition regime is highly sensitive to growth parameters such as substrate temperature and In flux, which affect surface adatom diffusion length and thus dot uniformity [79, 238].

In **Figure 6.3** (c), corresponding to 1.4 ML coverage, well-defined QDs begin to populate the surface with increased density and improved spatial uniformity. The dots are better separated and possess more consistent morphology compared to the 1.3 ML sample. This stage marks a near-complete transition into the 3D SK growth regime, where strain relaxation occurs via coherent islanding. The areal density and shape distribution become more uniform due to the stabilization of surface energy minimization pathways. The increased regularity at this stage is supported by simulations and kinetic models describing strain-driven islanding [252].

Figure 6.3 (b), corresponding to 1.6 ML coverage, represents the optimal SK QD morphology within the experimental conditions. The QDs are uniformly sized, well-aligned, and exhibit a high surface density. The image indicates highly efficient dot nucleation and growth, facilitated by maximized adatom mobility and balanced strain relaxation. This regime is widely reported as ideal for device-quality QDs used in quantum dot lasers, detectors, and solar cells due to narrow size dispersion and homogeneous spatial arrangement [253].

However, at a coverage of 2.5 ML, as depicted in Figure 6.3(a), the morphology begins to deteriorate. The AFM image shows an increase in dot size variability, irregular shapes, and indications of coalescence and ripening. These features are symptomatic of strain overaccumulation and the activation of inter-dot interactions such as Ostwald ripening, where larger dots grow at the expense of smaller ones [254].

In this overgrowth regime, the benefits of uniform self-assembly diminish, and defect formation becomes more probable.

Overall, **Figure 6.3** demonstrates the critical role of InAs coverage in directing SK QD evolution. The transition from 2D wetting layer to coherent 3D dots occurs between 1.3 and 1.4 ML. Optimal QD characteristics, including high density and uniformity, are achieved around 1.6 ML. Beyond this point, excessive material leads to degraded uniformity and onset of coalescence, highlighting the delicate balance required in MBE growth of SK QDs.

6.3.1.1.2. CAPPING LAYER

As **Figure 6.4** presents, atomic force microscopy (AFM) images of GaAs capping layers deposited over InAs quantum dot (QD) structures under varying growth temperatures, with the GaAs thickness fixed at 200 nm. The panels illustrate the influence of substrate temperature—from 515°C to 560°C—on the surface morphology, smoothness, and integrity of the underlying QDs during overgrowth. This analysis is vital for understanding how capping temperature impacts interfacial diffusion, QD shape preservation, and surface roughness—factors directly affecting the optoelectronic properties of quantum dot devices.

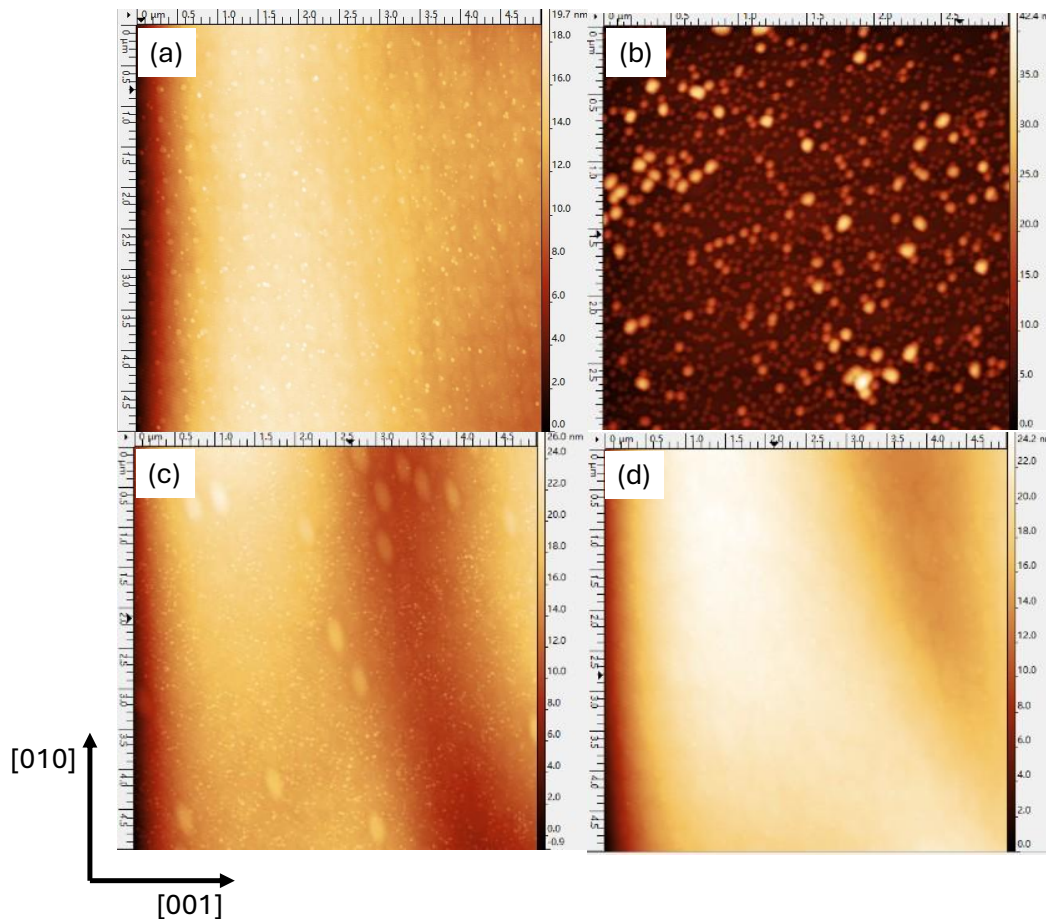


Figure 6.4 AFM images of capping layer with (a) 200nm GaAs capping layer under 515°C. (b) 200nm GaAs capping layer under 530°C. (c) 200nm GaAs capping layer under 550°C. (d) 200nm GaAs capping layer under 560°C.

In **Figure 6.4** (a), the sample capped at 515°C exhibits a moderately smooth surface with small-scale undulations and faint QD signatures visible beneath the surface. The relatively low capping temperature helps preserve the QD morphology by minimizing indium surface diffusion and intermixing with the GaAs matrix. Such preservation is important in maintaining the optical identity and confinement potential of individual QDs, as reported in prior work [255]. However, due to the lower mobility of Ga adatoms at this temperature, the surface may contain slight roughness and incomplete planarization.

Figure 6.4 (b), corresponding to 530°C capping, shows an increase in surface roughness and dot-like protrusions. This behavior suggests partial relaxation or intermixing between InAs and GaAs, likely due to enhanced adatom mobility. At this temperature, indium atoms begin to diffuse from the dot core toward the surrounding matrix, leading to partial flattening or distortion of the original dot shape.

Figure 6.4 (c), at 550°C, reveals elongated surface features and undulations indicative of significant indium-GaAs intermixing. The elevated temperature facilitates lateral indium diffusion, leading to morphological degradation of QDs. This compromises the quantum confinement and homogeneity of the dot ensemble, as previously demonstrated in thermal interdiffusion studies [256].

In contrast, **Figure 6.4** (d) at 560°C shows an extremely smooth and uniform surface, but no visible QD features. This suggests that the QDs have either fully dissolved or interdiffused into the GaAs matrix, eliminating distinct nanostructure contrast. While such smoothness may benefit certain applications requiring planarization, it is detrimental for QD-based light-emitting devices, where preservation of confinement and emission properties is critical [257].

This sequence of AFM images underscores the delicate trade-off between thermal-induced crystallinity improvement and the need to preserve QD integrity. Optimal capping requires careful temperature tuning to balance these competing mechanisms.

6.3.1.2. OPTICAL PROPERTIES OF PATTERNED InGaAs QUANTUM DOTS

Figure 6.5 presents a detailed photoluminescence (PL) characterization of InAs quantum dots (QDs) with 1.8 monolayer (ML) coverage, grown within a lithographically defined pattern region and studied under cryogenic conditions (10 K).

This figure explores the excitation power dependence of emission characteristics, evaluates recombination mechanisms through log-log intensity analysis, and models the emission profile with a Gaussian fit to extract the linewidth—parameters which are crucial for understanding the quantum optical response and uniformity of self-assembled QDs.

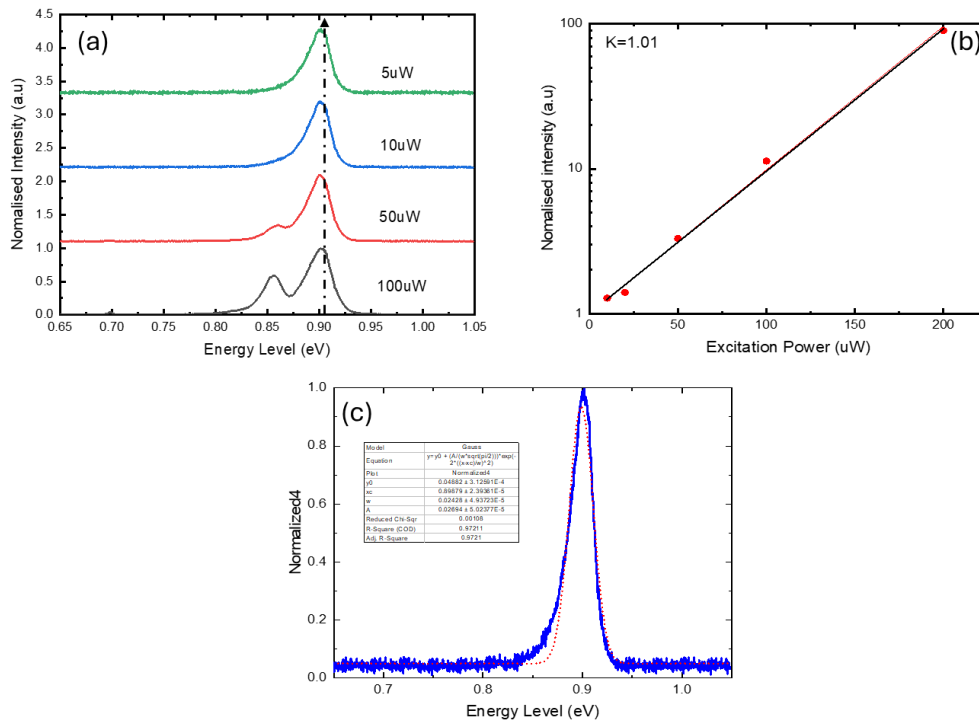


Figure 6.5 PL spectroscopy of a 1.8 ML coverage InAs quantum dots inside the pattern region (a) Excitation power dependent spectroscopy at 10K. (b) Normalise PL intensity depending upon the excitation power density at 10 K. The linear fitting indicated the slope of different InGaAs is around 1.01. (c) The PL spectrum of InAs quantum dot at 10K under $1 \mu\text{W}$ excitation power with Gaussian peak (FWHM=24meV)

Panel (a) displays the excitation power-dependent PL spectra recorded at 10 K, with excitation powers varying from low to higher levels. The spectra exhibit a prominent emission peak centred near $\sim 1.25 \text{ eV}$, attributed to the ground state excitonic

recombination in the InAs QDs. At lower excitation powers, the emission peak is narrow and symmetric, suggesting dominant single-state recombination without significant state filling. As excitation power increases, the intensity of the emission grows, while the spectral line retains its symmetry and peak position, indicating minimal band filling or heating effects under the power regime investigated. This behavior aligns with the radiative recombination regime dominated by exciton recombination in quantum-confined states, consistent with prior PL studies of MBE-grown InAs/GaAs QDs. Notably, no higher-energy excited-state peaks are visible, suggesting that either the excitation density remains below the excited-state occupation threshold, or the QD density is sufficiently low to prevent multi-state overlap.

Panel (b) quantitatively evaluates the PL response by plotting the normalized integrated PL intensity as a function of excitation power density on a logarithmic scale. The linear relationship observed, with a fitted slope of approximately 1.01, provides key insight into the underlying recombination dynamics. A slope near unity indicates that the PL intensity increases linearly with excitation power, affirming that radiative recombination dominates, with negligible contributions from non-radiative centers or Auger processes. This result validates the high optical quality of the QDs, which is essential for quantum emitter applications where linearity and brightness at low excitation are desired.

Panel (c) focuses on the detailed spectral shape of the QD emission under a low excitation power of 1 μW at 10 K. A high-resolution PL spectrum is modelled with a Gaussian function, yielding a full width at half maximum (FWHM) of 24 meV. This linewidth reflects both homogeneous broadening mechanisms (e.g., phonon coupling and radiative lifetime) and inhomogeneous broadening due to dot size and composition distribution. The narrow linewidth indicates excellent dot uniformity and minimal

interdot coupling or alloy fluctuation effects, which are crucial for achieving indistinguishable photon emission in quantum optics application. The fitted parameters (listed in the table inset) show a good correlation coefficient ($R^2 \approx 0.97$), confirming the spectral symmetry and minimal deviation from Gaussian behavior, which often characterizes well-confined, isolated QDs with reduced phonon sidebands.

The comprehensive data in **Figure 6.5** collectively underscore the high crystalline and optical quality of the InAs QDs formed under 1.8 ML coverage in the patterned region. The excitation power-dependent response confirms a robust single-exciton emission regime, while the narrow Gaussian PL peak reflects the structural and compositional uniformity of the dots. These findings are critical for designing quantum photonic devices, particularly where coherence and spectral purity are paramount.

6.3.1.3. CORRELATION BETWEEN STRUCTURAL AND OPTICAL PROPERTIES

The structural and optical performance of InAs/GaAs quantum dot (QD) arrays grown via the Stranski–Krastanov (SK) mechanism exhibit a strong, quantifiable correlation, particularly when fabricated under controlled molecular beam epitaxy (MBE) conditions. Atomic force microscopy (AFM) and photoluminescence (PL) spectroscopy provide complementary insight into the interplay between morphological evolution and quantum confinement, enabling optimization of device-grade QD arrays for photonic and optoelectronic applications.

Structural Insights via AFM Morphology **Figure 6.3** and **Figure 6.4** demonstrates the evolution of QD morphology as a function of InAs coverage. The transition from two-dimensional wetting layers (≤ 1.2 ML) to fully developed three-dimensional islands (~ 1.6 ML) is mediated by strain-induced nucleation. At sub-critical

coverage (1.2 ML), AFM images reveal smooth surfaces with no dot formation, consistent with the metastable wetting layer [245]. At 1.3 ML, early-stage islands begin to nucleate irregularly, marking the onset of the 2D–3D transition—highly sensitive to substrate temperature and indium flux [79, 238].

At 1.4 ML, coherent QDs begin to form uniformly, while at 1.6 ML, optimal morphology is achieved: high density, low size dispersion, and regular dot separation. This corresponds to a state of efficient strain relaxation and minimized surface energy, essential for uniform carrier confinement [252]. However, increasing coverage to 2.5 ML results in coalescence and Ostwald ripening, as shown by irregular shapes and dot agglomeration in AFM images [254]. Thus, precise coverage control is vital to maintaining dot integrity.

Capping temperature further influences structural fidelity post-growth. Figure 6.4 presents AFM images of a 200 nm GaAs capping layer grown at varying temperatures. At 515°C, faint QD topography remains visible, indicating successful morphology preservation with minimal intermixing [255]. As the temperature increases to 550–560°C, surface smoothness improves at the cost of QD degradation due to enhanced indium diffusion, leading to shape distortion and eventual dissolution [256, 257].

Optical Characterization via Photoluminescence (**Figure 6.5**) PL spectroscopy, shown in Figure 6.5, directly links these structural outcomes to quantum optical behavior. QDs grown at 1.8 ML coverage within lithographically defined arrays show a prominent, symmetric emission peak near ~ 1.25 eV under low-temperature (10 K) excitation. The emission remains stable with increasing excitation power, indicating minimal state filling and negligible thermal broadening.

The excitation power-dependent intensity plot (**Figure 6.5 (b)**) yields a power exponent $\alpha \approx 1.01$, confirming radiative exciton recombination as the dominant

mechanism. This linear trend implies minimal influence from non-radiative centers or Auger recombination, corroborating the high crystalline quality inferred from the uniform AFM morphology.

Gaussian fitting of the PL peak (**Figure 6.5** (c)) reveals a full width at half maximum (FWHM) of 24 meV, indicating low inhomogeneous broadening and confirming dot size and compositional uniformity. The symmetry and narrowness of the emission spectrum ($R^2 \approx 0.97$) are typical of well-isolated QDs with minimal phonon sidebands, as reported by Michler et al. (2000) [258] and Finley et al. (2001) [259]. These optical characteristics are directly traceable to the morphological regularity at 1.6–1.8 ML coverage observed in AFM.

6.3.2. CHARACTERISATION OF ORDERED INAS/GAAS QUANTUM DOT ARRAYS VIA DROPLET EPITAXY

The following subsection examines the structural characteristics of InAs dome-shaped (DE) quantum dot arrays through AFM-based morphological analysis, alongside their optical properties under varied growth conditions.

6.3.2.1. INFLUENCE FACTORS OF THE GROWTH PROCESS

This section examined the growth behavior of InAs quantum dots formed via droplet epitaxy (DE), highlighting the critical dependence on material coverage and capping temperature. Optimal QD formation occurs at approximately 1.6 monolayers (ML) of InAs; exceeding this coverage leads to dot coalescence and morphological degradation. Additionally, elevated capping temperatures promote interdiffusion between the QDs and surrounding matrix, resulting in reduced confinement and altered emission

characteristics. These findings underscore the need for precise control over both deposition amount and thermal processing to preserve QD integrity and optical performance.

6.3.2.1.1. ORDERING OF INDIUM DROPLET NUCLEATION ON GaAs SURFACES

The set of atomic force microscopy (AFM) images presented in **Figure 6.6** provides a comprehensive examination of the evolution of InAs droplet epitaxy (DE) quantum dots (QDs) under varying crystallization and group III/V ratio conditions. These surface topography images are essential in understanding the material morphology, density, and ordering characteristics that arise from the droplet epitaxy process—a versatile and substrate-temperature-tolerant method for fabricating self-assembled quantum dots without reliance on the Stranski–Krastanov strain-induced mechanism.

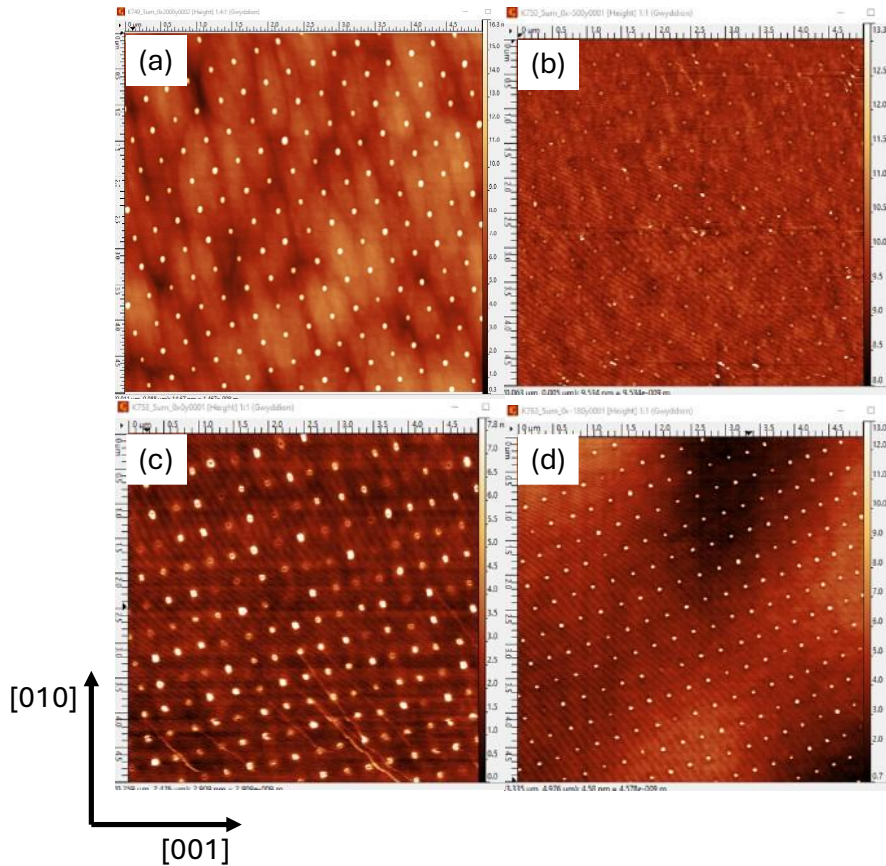


Figure 6.6 AFM image of (a) Indium droplet without crystallization. (b) Indium droplet with crystallization to form InAs DE QDs. (c) Indium droplet without crystallization with 0.6 III-V ratio at 200°C. (d) Indium droplet with crystallization to form InAs DE QDs under 0.8 III-V ratio at 200°C.

In **Figure 6.6** (a), the AFM image depicts the morphology of indium droplets deposited on the substrate surface in the absence of arsenic overpressure (i.e., no crystallization). The droplets appear well-separated and uniformly distributed across the scanned area, signifying a controlled nucleation of metallic indium. The distinct circular profiles are characteristic of liquid-phase indium clusters that are laterally stabilized due to surface tension and the low temperature growth conditions employed. The observed morphology is aligned with previously reported metallic droplet

formation studies, where controlled substrate temperatures and deposition rates help manage coalescence and Ostwald ripening effects [80, 260].

Figure 6.6 (b) illustrates the transformation of these indium droplets into InAs QDs through crystallization, achieved by exposing the system to an arsenic flux post-deposition. The image shows a significant morphological change where droplets convert into well-defined quantum dot features. These features exhibit sharper, more faceted profiles compared to the rounded indium droplets in (a), suggesting the onset of solid-state crystallization. The crystallization initiates a phase transition from metallic to compound semiconductor state, governed by the local As flux and the interfacial energy minimization between the substrate and the crystallized material. These results are consistent with earlier observations where droplet epitaxy under controlled group V exposure produces crystalline nanostructures without wetting layers [261, 262].

Figure 6.6 (c) and **Figure 6.6** (d) examines the impact of varying the III/V ratio during crystallization at a substrate temperature of 200°C. Specifically, **Figure 6.6** (c) represents the case where the group III/V ratio is maintained at 0.6, while **Figure 6.6** (d) corresponds to a slightly increased ratio of 0.8. In both cases, indium droplets are subjected to post-deposition arsenic exposure to facilitate crystallization into InAs DE QDs. In **Figure 6.6** (c), at a lower III/V ratio of 0.6, the AFM image indicates moderate dot formation with a relatively uniform size distribution, but with limited density. This suggests incomplete or less efficient crystallization, potentially due to insufficient arsenic availability to fully convert indium droplets into stoichiometric InAs. The surface shows sporadic dark patches, hinting at either insufficient nucleation or partial As incorporation. These observations underscore the necessity of optimal group V flux

in defining QD density and morphology, as insufficient arsenic leads to incomplete transformation [263, 264].

In contrast, **Figure 6.6** (d), recorded under a higher III/V ratio of 0.8, reveals a more densely packed array of uniform QDs, with minimal background noise or amorphous residuals. The higher arsenic availability in this scenario promotes more complete crystallization and enhanced dot uniformity. Furthermore, the higher dot density and improved ordering may also be a consequence of enhanced surface diffusion kinetics and optimized As-driven stabilization during growth. This aligns with findings in droplet epitaxy literature where the III/V ratio critically governs the transition kinetics, surface diffusion lengths, and resultant nanostructure morphology [255, 265].

These AFM analyses underscore the critical role of group V supply and crystallization conditions in determining the structural outcomes of InAs quantum dots grown via droplet epitaxy. The presence or absence of arsenic, combined with the precise III/V ratio during the crystallization phase, governs the transformation of metallic droplets into semiconducting nanostructures. These images serve not only as a morphological diagnostic but as empirical evidence to support growth optimization models for achieving uniform and high-density quantum dot arrays suitable for optoelectronic device applications.

6.3.2.1.2. CAPPING LAYER

Figure 6.7 presents a series of atomic force microscopy (AFM) images that illustrate the surface morphology of InAs quantum dots (QDs) formed via droplet epitaxy (DE) and subjected to varied thermal treatments and capping protocols. Each panel—(a), (b), and (c)—reflects a distinct thermal evolution sequence involving combinations of low-

temperature GaAs capping, intermediate annealing, and high-temperature encapsulation. The intention of these experiments is to explore how thermal processing and overgrowth temperatures influence QD surface preservation, intermixing, and nanostructure degradation. These insights are crucial for optimizing optical properties of QDs, especially for applications in optoelectronic devices where QD uniformity and surface stability are paramount.

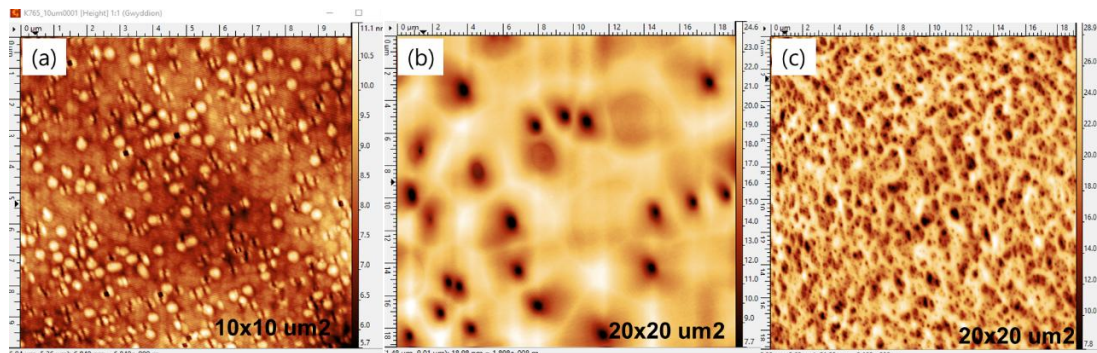


Figure 6.7 AFM image of InAs droplet epitaxy quantum dots sample of (a) 20 nm GaAs layer at 400°C + 10mins annealing at 400°C + 80 nm GaAs layer at 600°C. (b) 20 nm GaAs layer at 400°C + 10mins annealing at 400°C + 80 nm GaAs layer at 600°C + 30 mins annealing at 750°C. (c) 20 nm GaAs layer at 200°C + 80 nm GaAs layer at 600°C + 30 mins annealing at 750°C.

Figure 6.7 (a) depicts the AFM image of an InAs DE sample capped with a 20 nm GaAs layer at 400°C, followed by 10 minutes of annealing at the same temperature and an additional 80 nm GaAs overlayer deposited at 600°C. The observed surface retains clearly defined nanostructures, indicating that this two-step capping process—with an initial low-temperature layer to preserve dot morphology and a subsequent higher-temperature overgrowth to improve crystallinity—effectively stabilizes the QD features. The dots appear well-separated with moderate height contrast, suggesting minimal interdiffusion between InAs and GaAs and limited strain relaxation. This

agrees with previous reports emphasizing that initial low-temperature capping is critical for protecting the dot shape from thermal distortion, a concept initially established by Koguchi and Mano in the development of DE protocols.

In contrast, **Figure 6.7 (b)** reveals the dramatic morphological transformation induced by an additional post-growth annealing step. Here, after the same initial treatment as in (a), the sample is subjected to a 30-minute anneal at 750°C. The AFM image shows a smoother surface with a drastic loss of nanodot features. The blurred and broadened structures imply significant intermixing, surface diffusion, and possibly even dissolution of the QD ensemble into the surrounding GaAs matrix. At this high annealing temperature, In atoms are likely to diffuse out of the quantum dot volume and intermix with Ga atoms, a phenomenon well-documented in thermal interdiffusion studies of III–V heterostructures [256, 266]. This suggests that while annealing improves crystalline quality and reduces non-radiative recombination centers, it comes at the cost of morphological stability unless diffusion barriers or lower ramp rates are employed.

Figure 6.7 (c) provides a comparative morphology for a sample capped with a 20 nm GaAs layer grown at 200°C, followed directly by an 80 nm GaAs overgrowth at 600°C and a 30-minute anneal at 750°C. Unlike (b), the AFM image exhibits a dense and distinct nanodot array. The QD features are sharper and more numerous, indicating that the lower initial capping temperature (200°C instead of 400°C) better preserves the original dot morphology against high-temperature annealing. The success of this approach can be attributed to the suppression of indium diffusion during the initial encapsulation, thereby forming a diffusion-limiting shell.

These results collectively illustrate the delicate interplay between thermal budget, capping strategies, and quantum dot integrity in DE systems. Figure 6.5 confirms that

while high-temperature annealing can significantly enhance crystal quality and remove point defects, it simultaneously induces detrimental morphological changes if not counteracted by a carefully engineered low-temperature capping step. The progression from (a) to (c) exemplifies how subtle variations in growth protocols directly translate into nanoscale structural evolution—an insight essential for fabricating high-performance QD-based devices.

6.3.2.2. TEM ANALYSIS

As the **Figure 6.8** shows, the comparative microstructural and elemental analysis of InAs quantum dots (QDs), fabricated through droplet epitaxy, reveals significant insights into the impact of morphology on crystalline quality and compositional uniformity—both of which are crucial for single-photon emitter performance in photonic integrated circuits (PICs).

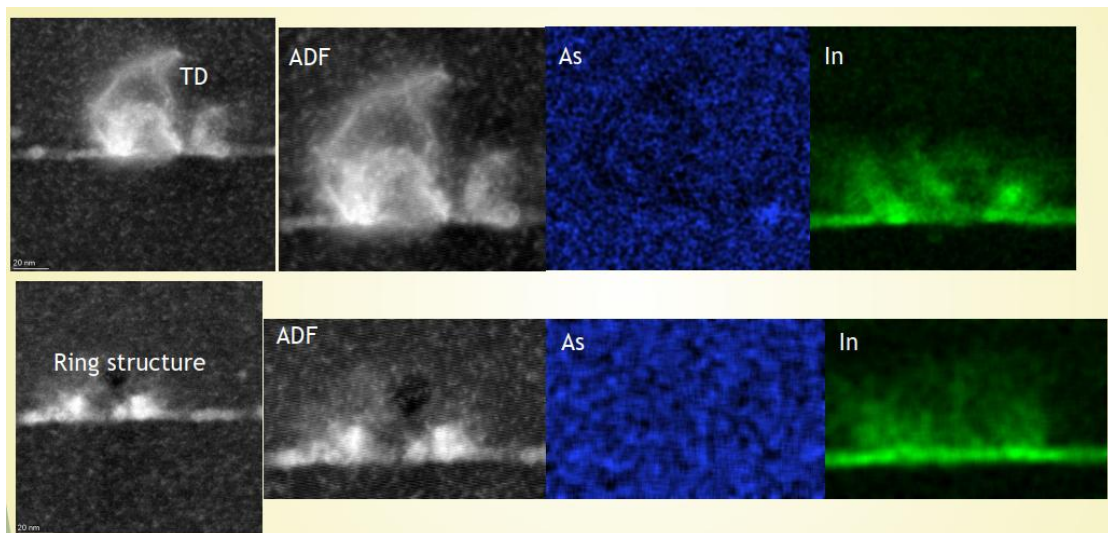


Figure 6.8 STEM image of the InAs Droplet epitaxy quantum dots sample with Annular Dark-Field view image, EELS view of Arsenic and Indium element distribution image,

Two distinct nanostructures are identified: a dome-like QD with a threading dislocation (TD) and a defect-free ring structure. In the case of the TD-associated QD, the presence of vertical defect lines observed in both transmission electron microscopy (TEM) and annular dark field (ADF) images indicates substantial strain relaxation [267]. This strain likely results from lattice mismatch between the InAs quantum dot and the GaAs substrate, consistent with previous observations in strained heteroepitaxial systems. Energy-dispersive X-ray spectroscopy (EDS) mapping further confirms a localized indium-rich region, corresponding to the quantum dot body. However, the presence of dislocations is detrimental, as it introduces non-radiative recombination centers that degrade photon purity, brightness, and the coherence of quantum emission [115, 268]. In contrast, the ring-shaped structure exhibits a defect-free profile with no evidence of threading dislocations in the ADF images. The In EDS signal appears more homogeneously distributed along the base and sidewalls, implying a lower internal strain field and more controlled indium incorporation. Such geometry is characteristic of ring-like quantum dot structures formed via droplet epitaxy, which offers enhanced control over shape and strain distribution when compared to traditional Stranski–Krastanov growth [260]. These structures are known to exhibit improved optical quality, including reduced spectral diffusion and enhanced indistinguishability of emitted photons, making them suitable for scalable integration into quantum photonic chips [269]. Overall, this comparative analysis underscores the advantages of droplet epitaxy in tailoring quantum dot morphology to mitigate lattice strain and suppress defect formation. The ability to fabricate symmetric, low-strain QDs without dislocations is critical for realizing high-performance, deterministic single-photon sources compatible with existing PIC architectures.

6.3.3. DISCUSSION

The development of ordered InAs/GaAs quantum dot (QD) arrays plays a pivotal role in advancing optoelectronic and quantum photonic devices, including single-photon sources, QD lasers, and detectors. This discussion presents a detailed comparison of InAs quantum dots grown via the Stranski–Krastanov (SK) mechanism and droplet epitaxy (DE), focusing on their structural evolution, crystallographic quality, and optical performance. The analysis draws on experimental results from atomic force microscopy (AFM), photoluminescence (PL), and transmission electron microscopy (TEM), and is contextualized with established literature.

SK quantum dots are formed through strain-induced self-assembly, where a two-dimensional wetting layer transitions into three-dimensional islands after a critical thickness of InAs is deposited on GaAs. This transition is driven by elastic strain relaxation arising from the lattice mismatch. At sub-critical coverage (e.g., 1.2 monolayers), the surface remains flat with no dot nucleation. As the coverage reaches approximately 1.3–1.4 ML, isolated QDs begin to nucleate with increasing regularity, and optimal QD morphology appears at 1.6 ML, with uniform size, high density, and spatial separation. These observations, supported by AFM imagery (Figure 6.3), confirm that SK dot formation is a strain-driven process highly sensitive to growth conditions such as indium flux and substrate temperature. Excessive deposition beyond 2.0 ML leads to coalescence and Ostwald ripening, producing larger, irregular structures and degraded uniformity, as reported by Joyce and Vvedensky (2004).

In contrast, DE QDs follow a fundamentally different growth route. Indium is first deposited at low temperature in the absence of arsenic, forming liquid droplets. These droplets are later crystallized into InAs QDs upon exposure to arsenic flux, independent of strain. AFM images (Figure 6.6) show that pre-crystallization droplets are circular

and well-dispersed. Post-crystallization, these structures transform into dome-shaped or ring-like QDs with faceted profiles, indicating solid-phase epitaxial transformation. Unlike SK dots, DE QDs do not exhibit a wetting layer, and their morphology is defined by local group III/V ratios, substrate temperature, and crystallization dynamics. Variations in the III/V ratio during arsenic exposure directly affect the efficiency and density of dot formation. A lower ratio (e.g., 0.6) results in sparse and incomplete QDs, while a higher ratio (0.8) yields dense and more uniform QD arrays. These behaviors are consistent with studies by Mano and Koguchi, which demonstrate that DE can achieve site-controlled, high-uniformity QDs without the defect risks associated with strain relaxation.

Capping layers and post-growth annealing further influence QD morphology. SK QDs capped at lower temperatures (around 515°C) retain their shape but suffer from incomplete planarization. Higher temperatures improve crystal quality but trigger indium diffusion, leading to QD dissolution. This thermal sensitivity is a major limitation for integrating SK QDs into high-temperature processing steps. In contrast, DE QDs show better stability under thermal treatments. A multi-step capping process—starting with low-temperature GaAs deposition followed by high-temperature overgrowth—preserves the QD morphology while enhancing crystallinity. This thermal resilience, as evidenced in Figure 6.7, makes DE-grown structures more adaptable for post-growth processing. However, prolonged high-temperature annealing (e.g., 750°C) can still cause degradation unless preceded by sufficiently low-temperature encapsulation.

TEM analysis further highlights the differences in crystallographic quality. SK QDs often exhibit threading dislocations due to strain relaxation, which degrade optical performance by introducing non-radiative recombination centers. In comparison, DE

QDs—particularly ring-like structures—are defect-free. Their indium distribution is more uniform, and there is no observable lattice strain or dislocations. These features are critical for maintaining photon purity, emission coherence, and reproducibility in quantum emitter applications.

Optical characterization via PL spectroscopy supports these structural insights. SK QDs with optimal coverage (~1.6–1.8 ML) exhibit strong, narrow emission peaks centered around 1.25 eV with full width at half maximum (FWHM) near 24 meV, indicating good size uniformity and minimal spectral diffusion. The emission intensity increases linearly with excitation power, confirming dominance of radiative recombination. DE QDs can achieve comparable optical quality, with the added benefit of reduced fine structure splitting and suppressed inhomogeneous broadening due to their relaxed strain profile and symmetric shape. These traits are particularly valuable for generating indistinguishable photons, as required in quantum photonic circuits.

From a fabrication standpoint, both methods benefit from in-situ Direct Laser Interference Patterning (DLIP), which enables spatial ordering of QDs without breaking vacuum. However, DE offers superior control over nucleation positioning, as indium droplets naturally form at the laser-induced low-energy nodes, whereas SK nucleation remains partially stochastic despite pre-patterning. This deterministic growth is essential for applications such as scalable quantum computing, where spatially aligned quantum dots function as coupled qubits or photon sources.

In summary, while SK QDs provide well-established pathways to high-quality optoelectronic structures, DE QDs offer key advantages including strain-free growth, enhanced defect tolerance, superior thermal stability, and improved spatial control. These attributes make droplet epitaxy an increasingly attractive approach for

integrating quantum dots into complex photonic architectures where precision and reproducibility are paramount.

6.4. SUMMARY

This chapter presents a detailed investigation into the fabrication and characterization of ordered InAs/GaAs quantum dot (QD) arrays, focusing on two distinct epitaxial growth mechanisms: Stranski–Krastanov (SK) and droplet epitaxy (DE), both enhanced by in-situ Direct Laser Interference Patterning (DLIP). The combination of these methods aims to address the ongoing challenge of achieving spatially ordered, optically uniform QD arrays suitable for integration into quantum photonic and optoelectronic devices.

A major achievement of this work is the successful implementation of DLIP within the MBE chamber, enabling in-situ, maskless surface patterning under ultra-high vacuum conditions. This innovation avoids contamination risks associated with ex-situ lithography and facilitates the deterministic placement of quantum dots. The DLIP-generated interference pattern guides adatom diffusion and localization, promoting nucleation at specific surface sites. This spatial control is crucial for applications that require deterministic QD positioning, such as single-photon emitters, quantum logic gates, and quantum dot molecules for coupled qubit systems.

For SK-grown QDs, the investigation identifies the relationship between InAs coverage and morphological evolution. AFM characterization shows that at sub-critical coverage (e.g., 1.2 ML), only a smooth wetting layer forms with no discernible dot features. As the coverage approaches 1.3–1.4 ML, nucleation of 3D islands begins, signifying the onset of the 2D-to-3D transition. Optimal quantum dot formation occurs at approximately 1.6 ML, where the dots exhibit high areal density, uniform size

distribution, and well-separated geometry. Beyond this, at 2.5 ML, dot morphology degrades due to excessive strain accumulation, resulting in coalescence and Ostwald ripening effects. These findings confirm that precise control of deposition thickness is critical to achieving high-quality QD structures using the SK mechanism.

Capping procedures further influence the structural integrity and optical performance of SK QDs. GaAs capping at lower temperatures (around 515°C) helps preserve dot morphology, though with some surface roughness. Higher capping temperatures (above 550°C) result in significant intermixing between InAs and GaAs, leading to flattening or dissolution of QD features. This thermal sensitivity limits the thermal processing window for SK-based QDs and poses challenges for device fabrication requiring subsequent high-temperature steps.

In contrast, QDs grown via droplet epitaxy offer enhanced morphological control and greater resilience to thermal treatments. This method involves forming indium droplets at low temperatures in the absence of arsenic, followed by crystallization into InAs nanostructures upon exposure to an arsenic flux. The absence of lattice strain in this process eliminates the formation of dislocations commonly observed in SK QDs. AFM images confirm the transformation of metallic droplets into well-defined dome-shaped QDs. The morphology of DE QDs is shown to be tunable through the group III/V ratio, with an optimal value of 0.8 yielding dense and uniform QD arrays. Lower ratios result in incomplete crystallization and reduced dot density. Importantly, the DE process avoids the formation of a wetting layer, offering a more abrupt interface and potentially superior carrier confinement.

Post-growth thermal processing studies on DE QDs demonstrate that a well-designed capping sequence can preserve QD integrity even at elevated temperatures. Initial low-temperature capping at 200–400°C followed by high-temperature

overgrowth at 600–750°C enables the formation of stable QDs with preserved morphology. TEM analysis further supports these findings, revealing that DE-grown QDs are often free of threading dislocations. Some ring-like structures show symmetrical profiles and uniform elemental distributions, which are favorable for reducing spectral diffusion and improving photon indistinguishability in quantum optical applications.

Optical characterization, particularly for SK QDs, confirms the structural observations. Photoluminescence spectra collected from samples with 1.8 ML InAs coverage exhibit strong emission near 1.25 eV, with a narrow linewidth (~ 24 meV) and a power-law slope near unity. These results confirm that the emission originates predominantly from radiative recombination of single excitons, with minimal influence from non-radiative centers or multiexciton processes. The spectral symmetry and narrow linewidths indicate good structural uniformity and compositional homogeneity, consistent with the observed AFM morphology. Although the PL properties of DE QDs were not explored in the same depth in this chapter, previous studies suggest they are capable of achieving comparable or even superior optical performance due to their strain-free nature and defect-free crystallinity.

Despite these promising results, several limitations remain. For SK QDs, the dependence on strain-driven nucleation and the sensitivity to capping temperature pose significant challenges. The degradation of dot morphology during post-growth annealing restricts their use in applications requiring high-temperature processing. Additionally, while DLIP improves positional control, the inherent stochasticity of SK islanding can still result in non-uniform nucleation, limiting device yield and reproducibility.

For DE QDs, although they exhibit superior thermal and structural stability, comprehensive optical characterization is still lacking in this work. Direct comparisons with SK QDs, particularly regarding coherence time, spectral diffusion, and entanglement generation, are necessary to fully validate their applicability in quantum information systems. Moreover, scaling DLIP-assisted DE processes to wafer-level uniformity while maintaining precise control over nucleation remains a technical challenge.

In summary, this chapter demonstrates the viability of both SK and DE methods for producing high-quality, ordered InAs/GaAs QD arrays, each with distinct advantages. The integration of in-situ DLIP offers a scalable route for deterministic patterning. SK QDs show excellent optical properties under optimized conditions but are limited by thermal sensitivity and defect risks. DE QDs provide superior structural control and robustness, making them highly promising candidates for next-generation quantum devices. However, further work is required to refine growth uniformity, expand optical data, and address scalability for commercial integration.

7. CONCLUSION AND FUTURE WORK

7.1. CONCLUSION

This thesis presents a detailed investigation into the deterministic fabrication and optical characterization of ordered III-V quantum dot (QD) arrays through the integration of direct laser interference patterning (DLIP) within molecular beam epitaxy (MBE). By successfully implementing a four-beam DLIP setup directly inside an ultra-high vacuum MBE chamber, this research introduces a scalable, lithography-free method for site-controlled nanostructure growth. The approach achieves precise spatial control over QD nucleation while maintaining high crystalline quality, a critical requirement for advanced quantum photonic and optoelectronic applications.

The study begins by establishing a theoretical and experimental basis for quantum confinement effects and the behavior of spatially ordered QD arrays. The relationship between spatial periodicity, inter-dot coupling, and miniband formation is shown to strongly influence carrier localization, energy level hybridization, and radiative recombination dynamics. These effects are systematically investigated through modelling and verified by experimental observation.

Two material systems are explored in depth: InGaAs/AlGaAs/GaAs QDs formed via droplet epitaxy, and InAs/GaAs QDs synthesized using both the Stranski–Krastanov and droplet epitaxy modes. The formation dynamics of these QDs are found to be highly sensitive to epitaxial growth conditions and DLIP-induced surface modulation. Parameters such as laser fluence, interference pattern pitch, and thermal

annealing directly affect QD morphology, density, and uniformity, providing a versatile means to engineer the emission properties of the quantum dots.

A major technical advancement of this work is the successful in-situ integration of the DLIP system into the MBE environment. This setup enables spatially periodic surface modulation during growth, promoting site-selective nucleation without the need for post-growth lithography or etching. The in-situ nature of this approach eliminates contamination risks and preserves surface integrity, allowing direct fabrication of high-purity nanostructures compatible with epitaxial growth protocols.

To support the fabrication process, a custom-designed automated photoluminescence (PL) mapping system is developed. This system allows high-resolution spatial and spectral characterization over large areas, offering real-time feedback on emission properties. Quantum dots produced using this method exhibit narrow emission linewidths down to 17 meV, confirming their high optical quality and consistency. Spatial mapping reveals strong uniformity across the sample surface, indicating effective control over QD nucleation and growth.

Experimental data aligns closely with theoretical predictions, including confinement energies, spectral linewidths, and coupling behavior. These results validate the underlying physical models and confirm the reliability of the DLIP-MBE technique for producing engineered QD arrays. The systematic correlation between growth parameters and optical characteristics establishes a reproducible framework for deterministic quantum dot fabrication across various material platforms.

Beyond fabrication, the thesis contributes to the understanding of ordered quantum systems by demonstrating control over inter-dot coupling, oscillator strength, and coherence properties. These capabilities are foundational for integrating QDs into quantum photonic circuits and logic devices. The ability to produce high-purity

emission with nanoscale positional accuracy supports key quantum information technologies, including secure communication, entanglement generation, and scalable quantum computing architectures.

This work positions DLIP-integrated MBE growth as a transformative method in the field of quantum nanophotonics. It overcomes the limitations of spontaneous self-assembly and conventional lithography, offering a direct, scalable route to fabricate functional nanostructures with precisely tailored optical properties. The insights developed here establish a foundation for future applications in quantum light sources, chip-based photonic integration, and quantum information processing. By demonstrating both technical feasibility and scientific relevance, this research advances the state of the art in site-controlled nanostructure engineering and provides a viable path toward manufacturable quantum photonic systems.

7.2. OUTLOOK

The follow-up work of this thesis would mainly focus on following applications: the fabrication of surface plasmonic solar cell with DLIP induced InGaAs quantum dots array, the optical characteristics of single QDs towards single photon emitter including indistinguishability, photon purity and brightness and the potential for photonic system-on-chip integration.

7.2.1. SURFACE PLASMONIC SOLAR CELL

The integration of surface plasmon polaritons (SPPs) with semiconductor quantum dots (QDs) represents a transformative approach in optoelectronic device engineering. SPPs—coherent oscillations of electrons coupled with electromagnetic waves at metal-dielectric interfaces—can significantly enhance the optical field intensity proximal to

quantum dots, thereby amplifying light absorption, carrier generation, and quantum efficiency.

This enhancement mechanism addresses a fundamental limitation in quantum dot-based devices: their inherently inefficient light absorption and charge carrier recombination characteristics, particularly when arranged in large-scale arrays. Direct laser interference patterning (DLIP) emerges as an innovative fabrication methodology that enables the controlled excitation of SPPs through periodic metallic nanostructures. Unlike conventional techniques such as electron beam lithography or focused ion beam milling, which are precise but prohibitively expensive and time-consuming for large-scale applications, DLIP offers a maskless, high-throughput approach capable of generating nanoscale patterns across substantial surface areas with sub-wavelength precision. The integration of DLIP-fabricated plasmonic structures with semiconductor quantum dots remains relatively unexplored, presenting a significant research opportunity.

The proposed research will investigate the fundamental mechanisms governing SPP-enhanced light-matter interactions in DLIP-fabricated quantum dot arrays. Through systematic optimization of geometric parameters and material compositions, this work aims to maximize the optical and electronic properties of these integrated structures. The fabrication process will employ multi-beam laser interference to create periodic plasmonic nanostructures on transparent conductive substrates, followed by the deposition of colloidal quantum dots synthesized via wet-chemical methods.

This research builds upon several key studies in the field. Polman and Atwater (2012) demonstrated that plasmonic structures could substantially improve light absorption in thin-film devices through guided mode coupling [270]. Koenderink et al. (2016) explored the interaction between quantum dots and plasmonic antennas,

observing enhanced radiative rates [271]. However, these investigations typically focused on isolated systems lacking scalability. The present work aims to bridge this gap by developing a scalable approach for integrating SPP-enhancing plasmonic nanostructures with quantum dot arrays using DLIP.

The anticipated outcomes include enhanced light absorption and improved quantum efficiency through SPP-mediated local field enhancement, as well as the development of a scalable fabrication methodology for large-area SPP-enhanced quantum dot arrays. This research has significant implications for next-generation optoelectronic devices, potentially revolutionizing applications in high-efficiency photovoltaics, photodetectors, and quantum information technologies through the synergistic combination of SPPs and quantum dots in a scalable manufacturing paradigm.

7.2.2. SINGLE PHOTON EMITTER TOWARDS QUANTUM TELE-COMMUNICATION

The development of scalable quantum photonic technologies necessitates dependable single-photon sources that can be seamlessly integrated into existing photonic infrastructures. Among various solid-state quantum emitters, Indium Gallium Arsenide (InGaAs) quantum dots (QDs) have emerged as exceptionally promising candidates for deterministic single-photon generation within Photonic Integrated Circuits (PICs). The telecom-band emission properties of InGaAs QDs constitute a significant advantage for quantum communication networks. These nanostructures naturally emit photons within the C-band (1.3–1.55 μm) wavelength range, corresponding to the minimal attenuation windows in silica fibres. This inherent compatibility with established fiber-optic infrastructures eliminates the need for frequency conversion, which typically introduces

additional noise and reduces overall efficiency. As demonstrated by MB Ward et al. (2008)[272], the intrinsic telecom emission facilitates long-distance quantum key distribution protocols with significantly reduced transmission losses compared to visible-wavelength alternatives.

The capacity for site-controlled fabrication represents another crucial advantage of InGaAs quantum dot technology. Unlike self-assembled quantum dots that form at random locations during epitaxial growth, site-controlled InGaAs QDs can be deterministically positioned within photonic structures through advanced lithographic techniques. XD Wang et al. (2022) [273] reported coupling efficiencies exceeding 85% when precisely positioning QDs within photonic crystal waveguides. This deterministic integration facilitates reproducible device characteristics and enables scalable manufacturing processes essential for commercial quantum photonic technologies.

The quantum optical properties of InGaAs QDs further underscore their suitability for quantum information applications. Under resonant excitation conditions, these nanostructures demonstrate single-photon purity (characterized by second-order correlation function $g^{(2)}(0)$) exceeding 99% and photon indistinguishability values surpassing 90% [274]. These metrics, documented in the comprehensive review by T Heindel et al. (2023) [121], confirm that InGaAs QDs satisfy the stringent requirements for quantum interference and entanglement generation—fundamental operations in photonic quantum computing and quantum network protocols. When integrated with on-chip optical resonators, InGaAs QDs exhibit enhanced light-matter interactions through the Purcell effect [275]. This enhancement not only increases the operational speed of single-photon sources but also improves their quantum coherence properties.

The compatibility of InGaAs QDs with electrical excitation mechanisms represents a significant practical advantage for integrated quantum photonic systems.

Electrically driven InGaAs QD devices eliminate the need for external pump lasers, substantially reducing system complexity and power requirements. For the integration potential of InGaAs QDs, it extends beyond passive photonic circuits to encompass active photonic functionalities [276]. The study by Huang (2024) [277] on exciton-polariton complexes established that InGaAs QDs can form localized single-photon sources embedded within engineered photonic lattices. This work demonstrated that quantum emitter properties could be tailored at the chip scale through precise control of the surrounding photonic environment, enabling novel quantum optical phenomena such as topologically protected photon transport.

In conclusion, site-controlled InGaAs quantum dot arrays represent a technologically mature platform for deterministic single-photon emission in photonic integrated circuits. Their natural telecom wavelength emission, compatibility with site-controlled fabrication methods, exceptional quantum optical properties, resonator-enhanced performance, and electrical operation capabilities collectively position them as leading candidates for scalable quantum photonic technologies. As quantum communication networks and photonic quantum computing architectures continue to evolve, InGaAs QD-based single-photon sources will likely play an increasingly pivotal role in their practical implementation.

7.2.3. OTHER APPLICATIONS

The integration of InGaAs quantum dot arrays within photonic systems-on-chip represents a transformative advancement in semiconductor quantum photonics. These nanostructures, typically ranging from 3-8 nm in height, exhibit exceptional optoelectronic properties governed by three-dimensional quantum confinement effects. The unique bandgap engineering capabilities of InGaAs quantum dots enable precise

emission wavelength tuning within the 1.3-1.55 μm telecom bands, making them ideally suited for integration with existing fiber-optic communication infrastructure.

Recent advancements in site-controlled epitaxial growth techniques have enabled the fabrication of deterministically positioned InGaAs quantum dot arrays with positional accuracy exceeding 50 nm, as demonstrated by NV Hauff et al. (2023) [278]. This precision positioning allows for optimal coupling between individual quantum emitters and photonic waveguide structures. I Limame and colleagues (2024) reported coupling efficiencies approaching 92% when integrating site-controlled InGaAs quantum dot arrays with silicon nitride waveguides through wafer bonding technique [279].

The compatibility of InGaAs quantum dots with complementary metal-oxide-semiconductor (CMOS) fabrication processes further enhances their suitability for large-scale integration. Their capacity to function both as single-photon sources and as nonlinear optical elements enables the realization of complex quantum photonic functionalities within a monolithic platform. Zhang et al. (2024) demonstrated quantum interference between photons emitted from distinct quantum dots within the same integrated circuit, achieving indistinguishability values exceeding 93% after on-chip filtering through cascaded ring resonators [280].

BIBLIOGRAPHY

1. DiVincenzo, D.P., et al., *Universal quantum computation with the exchange interaction*. nature, 2000. **408**(6810): p. 339-342.
2. Steane, A., *Quantum computing*. Reports on Progress in Physics, 1998. **61**(2): p. 117.
3. Kok, P., et al., *Linear optical quantum computing with photonic qubits*. Reviews of modern physics, 2007. **79**(1): p. 135-174.
4. Knill, E., R. Laflamme, and G.J. Milburn, *A scheme for efficient quantum computation with linear optics*. nature, 2001. **409**(6816): p. 46-52.
5. Carr, L., *Understanding quantum phase transitions*. 2010: CRC press.
6. Laing, A., et al., *High-fidelity operation of quantum photonic circuits*. Applied Physics Letters, 2010. **97**(21).
7. Milburn, G., *Photons as qubits*. Physica Scripta, 2009. **2009**(T137): p. 014003.
8. Buckley, S., K. Rivoire, and J. Vučković, *Engineered quantum dot single-photon sources*. Reports on Progress in Physics, 2012. **75**(12): p. 126503.
9. Xia, T., et al., *Randomized benchmarking of single-qubit gates in a 2D array of neutral-atom qubits*. Physical review letters, 2015. **114**(10): p. 100503.
10. Spring, J.B., et al., *Chip-based array of near-identical, pure, heralded single-photon sources*. Optica, 2017. **4**(1): p. 90-96.
11. Hepp, S., et al., *Purcell-enhanced single-photon emission from a strain-tunable quantum dot in a cavity-waveguide device*. Applied Physics Letters, 2020. **117**(25).
12. Pelton, M., *Modified spontaneous emission in nanophotonic structures*. Nature Photonics, 2015. **9**(7): p. 427-435.
13. Lohrmann, A., et al., *Single-photon emitting diode in silicon carbide*. Nature communications, 2015. **6**(1): p. 7783.
14. Russo, E., *Growth mechanisms of III-V semiconductor nanostructures on silicon*. 2015, EPFL.
15. Tütüncüoğlu, G., *The growth and optical properties of III-V nanostructures grown by Molecular Beam Epitaxy*. 2017, EPFL.
16. Bandyopadhyay, S., *Quantum Information Science from the Perspective of a Device and Materials Engineer*, in *Advanced Semiconductor and Organic Nano-Techniques*. 2003, Elsevier. p. 441-502.
17. Arora, B. and S. Ghosh, *Quantum structures OF III-V compound semiconductors*. Bulletin of Indian Physics Association, 2011. **41**(1).
18. Luo, W., et al., *Recent progress in quantum photonic chips for quantum communication and internet*. Light: Science & Applications, 2023. **12**(1): p. 175.
19. Ashrafi, A., *Quantum Confinement: An Ultimate Physics of Nanostructures*. Encyclopedia of Semiconductor Nanotechnology, 2011. **1**(10): p. 1-67.
20. Bastard, G., *Wave mechanics applied to semiconductor heterostructures*. 1990.
21. Efros, A.L. and M. Rosen, *The electronic structure of semiconductor nanocrystals*. Annual Review of Materials Science, 2000. **30**(1): p. 475-521.
22. Reimann, S.M. and M. Manninen, *Electronic structure of quantum dots*. Reviews of modern physics, 2002. **74**(4): p. 1283.

23. Haffouz, S., et al., *Bright single InAsP quantum dots at telecom wavelengths in position-controlled InP nanowires: the role of the photonic waveguide*. Nano letters, 2018. **18**(5): p. 3047-3052.
24. Weisbuch, C. and B. Vinter, *Quantum semiconductor structures: fundamentals and applications*. 2014: Elsevier.
25. Harrison, P. and A. Valavanis, *Quantum wells, wires and dots: theoretical and computational physics of semiconductor nanostructures*. 2016: John Wiley & Sons.
26. Norris, D.J. and M. Bawendi, *Measurement and assignment of the size-dependent optical spectrum in CdSe quantum dots*. Physical Review B, 1996. **53**(24): p. 16338.
27. Klimov, V.I., *Spectral and dynamical properties of multiexcitons in semiconductor nanocrystals*. Annu. Rev. Phys. Chem., 2007. **58**(1): p. 635-673.
28. Král, K. and Z. Khás, *Electron self-energy in quantum dots*. Physical Review B, 1998. **57**(4): p. R2061.
29. Kagan, C.R. and C.B. Murray, *Charge transport in strongly coupled quantum dot solids*. Nature nanotechnology, 2015. **10**(12): p. 1013-1026.
30. Liu, M., et al., *Colloidal quantum dot electronics*. Nature Electronics, 2021. **4**(8): p. 548-558.
31. Hulcius, E., A. Hospodková, and M. Zíková, *Quantum Dots*. Metalorganic Vapor Phase Epitaxy (MOVPE) Growth, Materials Properties, and Applications, 2019: p. 175-215.
32. Lazarenkova, O.L. and A.A. Balandin, *Miniband formation in a quantum dot crystal*. Journal of Applied Physics, 2001. **89**(10): p. 5509-5515.
33. Talapin, D.V. and C.B. Murray, *PbSe nanocrystal solids for n- and p-channel thin film field-effect transistors*. Science, 2005. **310**(5745): p. 86-89.
34. Guo, H.W., et al., *Stacking of 2D materials*. Advanced Functional Materials, 2021. **31**(4): p. 2007810.
35. Fu, M., et al., *Resonantly enhanced optical nonlinearity in hybrid semiconductor quantum dot-metal nanoparticle structures*. Applied Physics Letters, 2012. **100**(6).
36. Kalesaki, E., et al., *Dirac cones, topological edge states, and nontrivial flat bands in two-dimensional semiconductors with a honeycomb nanogeometry*. Physical review x, 2014. **4**(1): p. 011010.
37. Reithmaier, J.P., et al., *Strong coupling in a single quantum dot-semiconductor microcavity system*. Nature, 2004. **432**(7014): p. 197-200.
38. Neuberger, M., *III-V semiconducting compounds*. 2013: Springer Science & Business Media.
39. Li, S.S. and S.S. Li, *High-speed III-V semiconductor devices*. Semiconductor Physical Electronics, 1993: p. 455-502.
40. Stillman, G.E., V.M. Robbins, and N. Tabatabaie, *III-V compound semiconductor devices: Optical detectors*. IEEE Transactions on Electron Devices, 1984. **31**(11): p. 1643-1655.
41. Nakamura, S., *III-V nitride based light-emitting devices*. Solid State Communications, 1997. **102**(2-3): p. 237-248.
42. Wieder, H., *A review of the electrical and optical properties of III-V compound semiconductor films*. Journal of Vacuum Science and Technology, 1971. **8**(1): p. 210-223.

43. Alexiev, D., et al., *A Review of liquid phase epitaxial grown gallium arsenide*. arXiv preprint cond-mat/0408653, 2004.
44. Kroemer, H., *A proposed class of hetero-junction injection lasers*. Proceedings of the IEEE, 1963. **51**(12): p. 1782-1783.
45. Kroemer, H., *Heterostructure bipolar transistors and integrated circuits*. Proceedings of the IEEE, 1982. **70**(1): p. 13-25.
46. Vaya, P. and K. Ponnuraju, *Molecular Beam Epitaxy*. Solid State Materials, 1991: p. 249-263.
47. Dingle, R., W. Wiegmann, and C.H. Henry, *Quantum states of confined carriers in very thin Al_xGa_{1-x}As-GaAs-Al_xGa_{1-x}As heterostructures*. Physical Review Letters, 1974. **33**(14): p. 827.
48. Foxon, C., *Molecular beam epitaxy*, in *Interfaces, Quantum Wells, and Superlattices*. 1988, Springer. p. 11-41.
49. Ploog, K., *Molecular Beam Epitaxial Growth and Properties of Layered Semiconductor Structures for Advanced Photonic and Electronic Devices*, in *Physicochemical Hydrodynamics: Interfacial Phenomena*. 1988, Springer. p. 619-638.
50. Dupuis, R.D., *III-V semiconductor quantum-well devices grown by metalorganic chemical vapor deposition*. Proceedings of the IEEE, 2013. **101**(10): p. 2188-2199.
51. Manasevit, H., *The use of metalorganics in the preparation of semiconductor materials: Growth on insulating substrates*. Journal of Crystal Growth, 1972. **13**: p. 306-314.
52. Davies, G., et al., *Surface Reaction Mechanisms Governing the Selective Area Growth of III-V Compound Semiconductors by Chemical Beam Epitaxy*. MRS Online Proceedings Library (OPL), 1992. **282**: p. 3.
53. Coleman, J., et al., *Disorder of an AlAs-GaAs superlattice by silicon implantation*. Applied Physics Letters, 1982. **40**(10): p. 904-906.
54. Vurgaftman, I., J. Meyer, and L.R. Ram-Mohan, *Band parameters for III-V compound semiconductors and their alloys*. Journal of applied physics, 2001. **89**(11): p. 5815-5875.
55. Asai, T. and D.S. Dandy, *Thermodynamic analysis of III-V semiconductor alloys grown by metalorganic vapor phase epitaxy*. Journal of Applied Physics, 2000. **88**(7): p. 4407-4416.
56. Stringfellow, G., H. Hall Jr, and R. Burmeister, *Electrical properties of nitrogen-doped GaP*. Journal of Applied Physics, 1975. **46**(7): p. 3006-3011.
57. Quillec, M., *Optoelectronic Materials*, in *Crucial Issues in Semiconductor Materials and Processing Technologies*. 1992, Springer. p. 83-101.
58. Guha, S. and J. Yang. *Amorphous silicon alloy materials, cells, and modules*. in *Conference Record of the Twenty-Ninth IEEE Photovoltaic Specialists Conference, 2002*. 2002. IEEE.
59. Bett, A.W., et al., *III-V compounds for solar cell applications*. Applied Physics A, 1999. **69**: p. 119-129.
60. Matthews, J. and A. Blakeslee, *Defects in epitaxial multilayers: I. Misfit dislocations*. Journal of Crystal growth, 1974. **27**: p. 118-125.

61. Brantley, W., et al., *Effect of dislocations on green electroluminescence efficiency in GaP grown by liquid phase epitaxy*. Journal of Applied Physics, 1975. **46**(6): p. 2629-2637.
62. Gourley, P., T. Drummond, and B. Doyle, *Dislocation filtering in semiconductor superlattices with lattice-matched and lattice-mismatched layer materials*. Applied physics letters, 1986. **49**(17): p. 1101-1103.
63. Böhme, O., C. Ziegler, and W. Göpel, *Oriented growth of quinquethiophene on SiO₂—An atomic force microscopy study*. Advanced Materials, 1994. **6**(7-8): p. 587-589.
64. Zucca, R., et al., *Semi-Insulating GaAs — a User's View*, in *Semi-Insulating III-V Materials: Nottingham 1980*, G.J. Rees, Editor. 1980, Birkhäuser Boston: Boston, MA. p. 335-345.
65. Wang, C., et al. *Lattice-matched epitaxial GaInAsSb/GaSb thermophotovoltaic devices*. in *AIP Conference Proceedings*. 1997. American Institute of Physics.
66. Fitzgerald, E., *Dislocations in strained-layer epitaxy: theory, experiment, and applications*. Materials science reports, 1991. **7**(3): p. 87-142.
67. Fitzgerald, E., et al., *Totally relaxed Ge_xSi_{1-x} layers with low threading dislocation densities grown on Si substrates*. Applied physics letters, 1991. **59**(7): p. 811-813.
68. Yang, W., et al., *III-V compound materials and lasers on silicon*. Journal of Semiconductors, 2019. **40**(10): p. 101305.
69. Runton, D.W., et al., *History of GaN: High-power RF gallium nitride (GaN) from infancy to manufacturable process and beyond*. IEEE Microwave Magazine, 2013. **14**(3): p. 82-93.
70. Nakamura, S., *Zn-doped InGaN growth and InGaN/AlGaN double-heterostructure blue-light-emitting diodes*. Journal of Crystal Growth, 1994. **145**(1-4): p. 911-917.
71. Samuelson, L., et al., *Semiconductor nanowires for novel one-dimensional devices*. Physica E: Low-dimensional Systems and Nanostructures, 2004. **21**(2-4): p. 560-567.
72. Michler, P., et al., *A quantum dot single-photon turnstile device*. science, 2000. **290**(5500): p. 2282-2285.
73. Alonso-Álvarez, D., et al., *Solcore: a multi-scale, Python-based library for modelling solar cells and semiconductor materials*. Journal of Computational Electronics, 2018. **17**: p. 1099-1123.
74. Sze, S.M., Y. Li, and K.K. Ng, *Physics of semiconductor devices*. 2021: John wiley & sons. Chapter 12.
75. Liang, D. and J.E. Bowers, *Recent progress in heterogeneous III-V-on-silicon photonic integration*. Light: Advanced Manufacturing, 2021. **2**(1): p. 59-83.
76. Woude, D.v.d., et al., *A review on epitaxial lift-off for III-V solar cells*. 2024.
77. Roelkens, G., et al., *III-V/Si photonics by die-to-wafer bonding*. Materials Today, 2007. **10**(7-8): p. 36-43.
78. Schiavon, D., *Analysis of the green gap problem in III-nitride LEDs*. 2016.
79. Xie, Q., et al., *Vertically self-organized InAs quantum box islands on GaAs (100)*. Physical review letters, 1995. **75**(13): p. 2542.

80. Tersoff, J., C. Teichert, and M. Lagally, *Self-organization in growth of quantum dot superlattices*. Physical Review Letters, 1996. **76**(10): p. 1675.
81. Grigoriev, D., et al., *Three-dimensional self-ordering in an InGaAs/GaAs multilayered quantum dot structure investigated by x-ray diffuse scattering*. Journal of Physics D: Applied Physics, 2005. **38**(10A): p. A154.
82. Wang, Z.M., et al., *Nanoholes fabricated by self-assembled gallium nanodrive on GaAs (100)*. Applied physics letters, 2007. **90**(11).
83. Liu, N., et al., *Nonuniform composition profile in In 0.5 Ga 0.5 As alloy quantum dots*. Physical Review Letters, 2000. **84**(2): p. 334.
84. Schmidt, O. and K. Eberl, *Multiple layers of self-assembled Ge/Si islands: Photoluminescence, strain fields, material interdiffusion, and island formation*. Physical Review B, 2000. **61**(20): p. 13721.
85. Li, X., Y. Cao, and G. Yang, *Thermodynamic theory of two-dimensional to three-dimensional growth transition in quantum dots self-assembly*. Physical Chemistry Chemical Physics, 2010. **12**(18): p. 4768-4772.
86. Panda, D., et al., *Optimization of dot layer periodicity through analysis of strain and electronic profile in vertically stacked InAs/GaAs Quantum dot heterostructure*. Journal of Alloys and Compounds, 2018. **736**: p. 216-224.
87. Biasiol, G. and E. Kapon, *Mechanisms of self-ordering of quantum nanostructures grown on nonplanar surfaces*. Physical review letters, 1998. **81**(14): p. 2962.
88. Springholz, G., *Three-dimensional stacking of self-assembled quantum dots in multilayer structures*. Comptes Rendus Physique, 2005. **6**(1): p. 89-103.
89. Mano, T., et al., *Direct imaging of self-organized anisotropic strain engineering for improved one-dimensional ordering of (In, Ga) As quantum dot arrays*. Journal of applied physics, 2004. **95**(1): p. 109-114.
90. Mano, T., et al., *Formation of InAs quantum dot arrays on GaAs (100) by self-organized anisotropic strain engineering of a (In, Ga) As superlattice template*. Applied physics letters, 2002. **81**(9): p. 1705-1707.
91. Wang, Z.M., et al., *Fabrication of (In,Ga)As quantum-dot chains on GaAs(100)*. Applied Physics Letters, 2004. **84**(11): p. 1931-1933.
92. Ledentsov, N., et al., *Direct formation of vertically coupled quantum dots in Stranski-Krastanow growth*. Physical Review B, 1996. **54**(12): p. 8743.
93. Selçuk, E., A.Y. Silov, and R. Nötzel, *Single InAs quantum dot arrays and directed self-organization on patterned GaAs (311) B substrates*. Applied Physics Letters, 2009. **94**(26).
94. Strel'chuk, V., et al., *Lateral ordering of quantum dots and wires in the (In, Ga) As/GaAs (100) multilayer structures*. Semiconductors, 2007. **41**: p. 73-80.
95. Kim, J.M., et al., *Strain engineering of low-dimensional materials for emerging quantum phenomena and functionalities*. Advanced Materials, 2023. **35**(27): p. 2107362.
96. Tejedor, P., et al., *Linear arrays of InGaAs quantum dots on nanostructured GaAs-on-Si substrates*. Applied Surface Science, 2023. **616**: p. 156518.
97. Schmidt, O., K. Eberl, and Y. Rau, *Strain and band-edge alignment in single and multiple layers of self-assembled Ge/Si and GeSi/Si islands*. Physical Review B, 2000. **62**(24): p. 16715.

98. Ishikawa, T., et al., *Site-controlled InAs single quantum-dot structures on GaAs surfaces patterned by in situ electron-beam lithography*. Applied Physics Letters, 2000. **76**(2): p. 167-169.
99. Lee, J.Y., et al., *Filling of hole arrays with InAs quantum dots*. Nanotechnology, 2009. **20**(28): p. 285305.
100. Jons, K., et al., *Triggered indistinguishable single photons with narrow line widths from site-controlled quantum dots*. Nano Letters, 2013. **13**(1): p. 126-130.
101. Yakes, M.K., et al., *Leveraging crystal anisotropy for deterministic growth of InAs quantum dots with narrow optical linewidths*. Nano letters, 2013. **13**(10): p. 4870-4875.
102. Heidemeyer, H., C. Müller, and O. Schmidt, *Highly ordered arrays of In (Ga) As quantum dots on patterned GaAs (0 0 1) substrates*. Journal of crystal growth, 2004. **261**(4): p. 444-449.
103. Tommila, J., et al., *Nanoimprint lithography patterned GaAs templates for site-controlled InAs quantum dots*. Journal of Crystal Growth, 2011. **323**(1): p. 183-186.
104. Herranz, J., et al., *Study of growth parameters for single InAs QD formation on GaAs (001) patterned substrates by local oxidation lithography*. Crystal Growth & Design, 2015. **15**(2): p. 666-672.
105. Skiba-Szymanska, J., et al., *Universal growth scheme for quantum dots with low fine-structure splitting at various emission wavelengths*. Physical Review Applied, 2017. **8**(1): p. 014013.
106. Albert, F., et al., *Quantum efficiency and oscillator strength of site-controlled InAs quantum dots*. Applied Physics Letters, 2010. **96**(15).
107. Atkinson, P., et al., *Molecular beam epitaxial growth of site-controlled InAs quantum dots on pre-patterned GaAs substrates*. Microelectronics journal, 2006. **37**(12): p. 1436-1439.
108. Wang, Y.-R., et al., *Formation of laterally ordered quantum dot molecules by in situ nanosecond laser interference*. Applied Physics Letters, 2020. **116**(20).
109. Clegg, C.M. and H. Yang, *Guided assembly of quantum dots through selective laser heating*. Solar Energy Materials and Solar Cells, 2013. **108**: p. 252-255.
110. Zhang, W., et al., *In-situ laser nano-patterning for ordered InAs/GaAs (001) quantum dot growth*. Applied Physics Letters, 2018. **112**(15).
111. Wang, Y.R., et al., *Precise arrays of epitaxial quantum dots nucleated by in situ laser interference for quantum information technology applications*. ACS applied nano materials, 2020. **3**(5): p. 4739-4746.
112. Han, I.S., Y.-R. Wang, and M. Hopkinson, *Ordered GaAs quantum dots by droplet epitaxy using in situ direct laser interference patterning*. Applied Physics Letters, 2021. **118**(14).
113. Wang, Y.R., et al., *Thermodynamic processes on a semiconductor surface during in-situ multi-beam laser interference patterning*. IET Optoelectronics, 2019. **13**(1): p. 7-11.
114. Wang, Y.-R., I.S. Han, and M. Hopkinson, *Fabrication of quantum dot and ring arrays by direct laser interference patterning for nanophotonics*. Nanophotonics, 2023. **12**(8): p. 1469-1479.

115. Senellart, P., G. Solomon, and A. White, *High-performance semiconductor quantum-dot single-photon sources*. Nature nanotechnology, 2017. **12**(11): p. 1026-1039.
116. Huber, D., et al., *Highly indistinguishable and strongly entangled photons from symmetric GaAs quantum dots*. Nature communications, 2017. **8**(1): p. 15506.
117. Ferry, D., J. Bird, and R. Akis, *Quantum dots: applications in technology and in quantum physics*. Physica E: Low-dimensional Systems and Nanostructures, 2004. **25**(2-3): p. 298-302.
118. Michler, P., *Quantum dots for quantum information technologies*. Vol. 237. 2017: Springer.
119. Liu, J., et al., *A solid-state source of strongly entangled photon pairs with high brightness and indistinguishability*. Nature nanotechnology, 2019. **14**(6): p. 586-593.
120. Dalacu, D., P.J. Poole, and R.L. Williams, *Nanowire-based sources of non-classical light*. Nanotechnology, 2019. **30**(23): p. 232001.
121. Heindel, T., et al., *Quantum dots for photonic quantum information technology*. Advances in Optics and Photonics, 2023. **15**(3): p. 613-738.
122. Lodahl, P., *Quantum-dot based photonic quantum networks*. Quantum Science and Technology, 2017. **3**(1): p. 013001.
123. Wang, Y.R., et al., *Thermodynamic processes on a semiconductor surface during in-situ multi-beam laser interference patterning*. 2019. **13**(1): p. 7-11.
124. Wang, L.-F., et al., *Theoretical modelling of single-mode lasing in microcavity lasers via optical interference injection*. 2020. **28**(11): p. 16486-16496.
125. Cho, A.Y. and J. Arthur, *Molecular beam epitaxy*. Progress in solid state chemistry, 1975. **10**: p. 157-191.
126. Tsang, W., *Chemical beam epitaxy of InP and GaAs*. Applied Physics Letters, 1984. **45**(11): p. 1234-1236.
127. Henini, M., *Molecular beam epitaxy: from research to mass production*. 2012: Newnes.
128. Joyce, B., *Molecular beam epitaxy*. Reports on Progress in Physics, 1985. **48**(12): p. 1637.
129. Foxon, C., *Three decades of molecular beam epitaxy*. Journal of Crystal Growth, 2003. **251**(1-4): p. 1-8.
130. Arthur, J.R., *Molecular beam epitaxy*. Surface science, 2002. **500**(1-3): p. 189-217.
131. Neave, J., et al., *Dynamics of film growth of GaAs by MBE from RHEED observations*. Applied Physics A, 1983. **31**: p. 1-8.
132. Arthur Jr, J., *Interaction of Ga and As₂ molecular beams with GaAs surfaces*. Journal of Applied Physics, 1968. **39**(8): p. 4032-4034.
133. Venables, J., *Introduction to surface and thin film processes*. 2000: Cambridge university press.
134. Von Wenckstern, H., *Group-III sesquioxides: growth, physical properties and devices*. Advanced Electronic Materials, 2017. **3**(9): p. 1600350.
135. Tersoff, J., A.D. Van Der Gon, and R. Tromp, *Critical island size for layer-by-layer growth*. Physical review letters, 1994. **72**(2): p. 266.
136. Pimpinelli, A. and J. Villain, *Physics of crystal growth*. 1999.

137. Foxon, C. and B. Joyce, *Interaction kinetics of As₂ and Ga on {100} GaAs surfaces*. Surface Science, 1977. **64**(1): p. 293-304.
138. Foxon, C., et al., *Kinetics in Molecular Beam Epitaxy—Modulated Beam Studies*. Kinetics of Ordering and Growth at Surfaces, 1990: p. 253-262.
139. Koenraad, P.M. and M.E. Flatté, *Single dopants in semiconductors*. Nature materials, 2011. **10**(2): p. 91-100.
140. Michely, T. and J. Krug, *Islands, mounds and atoms*. Vol. 42. 2012: Springer Science & Business Media.
141. Koudinov, A., et al., *Ultranarrow lines in Raman spectra of quantum wells due to effective acoustic phonon selection by in-plane wave vector*. Physical Review B, 2022. **105**(12): p. L121301.
142. Shen, C., et al., *Machine-learning-assisted and real-time-feedback-controlled growth of InAs/GaAs quantum dots*. Nature Communications, 2024. **15**(1): p. 2724.
143. Leonard, D., K. Pond, and P. Petroff, *Critical layer thickness for self-assembled InAs islands on GaAs*. Physical Review B, 1994. **50**(16): p. 11687.
144. Joyce, B., et al., *Nucleation and growth mechanisms during MBE of III–V compounds*. Materials Science and Engineering: B, 1999. **67**(1-2): p. 7-16.
145. Bauer, S., *Energetics of the Boranes. V. Prediction of Heats of Formation. Interconversion of the Hydrides of Boron*. Journal of the American Chemical Society, 1958. **80**(2): p. 294-298.
146. Prieto, J.E. and I. Markov, *Some thermodynamic aspects of self-assembly of arrays of quantum dots*. arXiv preprint cond-mat/0307275, 2003.
147. Matthews, J.W. and A.E. Blakeslee, *Defects in epitaxial multilayers: I. Misfit dislocations*. Journal of Crystal growth, 1974. **27**: p. 118-125.
148. Grundmann, M., et al., *Ultranarrow luminescence lines from single quantum dots*. Physical Review Letters, 1995. **74**(20): p. 4043.
149. Foxon, C. and B. Joyce, *Surface processes controlling the growth of GaIn_{1-x}As and GaIn_{1-x}P alloy films by MBE*. Journal of Crystal Growth, 1978. **44**(1): p. 75-83.
150. Shin, B., et al., *Comparison of morphology evolution of Ge (001) homoepitaxial films grown by pulsed laser deposition and molecular-beam epitaxy*. Applied Physics Letters, 2005. **87**(18).
151. Bimberg, D., M. Grundmann, and N.N. Ledentsov, *Quantum dot heterostructures*. 1999: John Wiley & Sons.
152. Martín-Sánchez, J., et al., *Ordered InAs quantum dots on pre-patterned GaAs (001) by local oxidation nanolithography*. Journal of crystal growth, 2005. **284**(3-4): p. 313-318.
153. Leon, R., et al., *Effects of interdiffusion on the luminescence of InGaAs/GaAs quantum dots*. Applied physics letters, 1996. **69**(13): p. 1888-1890.
154. Costantini, G., et al., *Interplay between Thermodynamics and Kinetics in the Capping of InAs/GaAs (001) Quantum Dots*. Physical review letters, 2006. **96**(22): p. 226106.
155. Koguchi, N.K.N. and K.I.K. Ishige, *Growth of GaAs epitaxial microcrystals on an S-terminated GaAs substrate by successive irradiation of Ga and As molecular beams*. Japanese journal of applied physics, 1993. **32**(5R): p. 2052.

156. Mano, T. and N. Koguchi, *Nanometer-scale GaAs ring structure grown by droplet epitaxy*. Journal of crystal growth, 2005. **278**(1-4): p. 108-112.
157. Lai, N.D., et al., *Precisely introducing defects into periodic structures by using a double-step laser scanning technique*. Applied optics, 2006. **45**(22): p. 5777-5782.
158. Jo, M., T. Mano, and K. Sakoda, *Two-step formation of gallium droplets with high controllability of size and density*. Crystal growth & design, 2011. **11**(10): p. 4647-4651.
159. Abbarchi, M., *Spectroscopy of single GaAs nanoemitters towards quantum communication*. 2009.
160. Liu, X., et al., *Vanishing fine-structure splittings in telecommunication-wavelength quantum dots grown on (111) A surfaces by droplet epitaxy*. Physical Review B, 2014. **90**(8): p. 081301.
161. Kiravittaya, S., A. Rastelli, and O.G. Schmidt, *Advanced quantum dot configurations*. Reports on Progress in Physics, 2009. **72**(4): p. 046502.
162. Atkinson, P., E. Zallo, and O. Schmidt, *Independent wavelength and density control of uniform GaAs/AlGaAs quantum dots grown by infilling self-assembled nanoholes*. Journal of applied Physics, 2012. **112**(5).
163. Voisiat, B., et al., *Improving the homogeneity of diffraction based colours by fabricating periodic patterns with gradient spatial period using Direct Laser Interference Patterning*. Scientific reports, 2019. **9**(1): p. 7801.
164. Henriques, B., et al., *Direct Laser Interference Patterning of Zirconia Using Infra-Red Picosecond Pulsed Laser: Effect of Laser Processing Parameters on the Surface Topography and Microstructure*. Advanced Functional Materials, 2024. **34**(2): p. 2307894.
165. Pandey, S., et al., *Designing a square periodic racemic helix photonic metamaterial using phase-controlled interference lithography for tailored chiral response*. Optics & Laser Technology, 2024. **172**: p. 110489.
166. Martín-Sánchez, J., et al., *Single photon emission from site-controlled InAs quantum dots grown on GaAs (001) patterned substrates*. Acs Nano, 2009. **3**(6): p. 1513-1517.
167. Ready, J., *Effects of high-power laser radiation*. 2012: Elsevier.
168. Bulgakova, N. and A. Bulgakov, *Pulsed laser ablation of solids: transition from normal vaporization to phase explosion*. Applied Physics A, 2001. **73**: p. 199-208.
169. Dimitrovski, D., et al., *Ionization of oriented carbonyl sulfide molecules by intense circularly polarized laser pulses*. Physical Review A—Atomic, Molecular, and Optical Physics, 2011. **83**(2): p. 023405.
170. Bäuerle, D. and D. Bäuerle, *Laser-CVD of microstructures*. Laser Processing and Chemistry, 2011: p. 369-392.
171. Zhang, W., et al., *Laser induced nano-patterning with atomic-scale thickness on an InAs/GaAs surface*. Semiconductor Science and Technology, 2018. **33**(11): p. 115021.
172. Mei, D., et al., *Three-dimensional ordered patterns by light interference*. Optics letters, 1995. **20**(5): p. 429-431.
173. Cai, L., X. Yang, and Y. Wang, *Formation of three-dimensional periodic microstructures by interference of four noncoplanar beams*. Journal of the Optical Society of America A, 2002. **19**(11): p. 2238-2244.

174. Wang, X., et al., *Three-dimensional laser-induced photoacoustic tomography of mouse brain with the skin and skull intact*. Optics letters, 2003. **28**(19): p. 1739-1741.
175. Burrow, G.M. and T.K. Gaylord, *Multi-beam interference advances and applications: nano-electronics, photonic crystals, metamaterials, subwavelength structures, optical trapping, and biomedical structures*. Micromachines, 2011. **2**(2): p. 221-257.
176. Deng, X., et al. *Five-beam interference pattern model for laser interference lithography*. in *The 2010 IEEE international conference on information and automation*. 2010. IEEE.
177. Yang, S.T., et al., *Thermal transport in CO₂ laser irradiated fused silica: In situ measurements and analysis*. Journal of Applied Physics, 2009. **106**(10).
178. Liu, C., et al., *Large-area micro/nanostructures fabrication in quartz by laser interference lithography and dry etching*. Applied Physics A, 2010. **101**: p. 237-241.
179. Moon, J.H., J. Ford, and S. Yang, *Fabricating three-dimensional polymeric photonic structures by multi-beam interference lithography*. Polymers for Advanced Technologies, 2006. **17**(2): p. 83-93.
180. Wang, D., et al., *Effects of polarization on four-beam laser interference lithography*. Applied physics letters, 2013. **102**(8).
181. Herman, M.A. and H. Sitter, *Molecular beam epitaxy: fundamentals and current status*. Vol. 7. 2012: Springer Science & Business Media.
182. Foxon, C. *Dynamic Aspects of Growth by MBE*. in *Heterojunctions and Semiconductor Superlattices: Proceedings of the Winter School Les Houches, France, March 12–21, 1985*. 1986. Springer.
183. Joyce, B., et al., *The determination of mbe growth mechanisms using dynamic rheed techniques*. Surface Science, 1986. **174**(1-3): p. 1-9.
184. Tsang, W., *Progress in chemical beam epitaxy*. Journal of crystal growth, 1990. **105**(1-4): p. 1-29.
185. Stringfellow, G.B., *Organometallic vapor-phase epitaxy: theory and practice*. 1999: Elsevier.
186. Panish, M., *Molecular beam epitaxy of GaAs and InP with gas sources for As and P*. Journal of The Electrochemical Society, 1980. **127**(12): p. 2729.
187. Zhang, Z. and M.G. Lagally, *Atomistic processes in the early stages of thin-film growth*. Science, 1997. **276**(5311): p. 377-383.
188. Van Hove, J., et al., *Damped oscillations in reflection high energy electron diffraction during GaAs MBE*. Journal of Vacuum Science & Technology B: Microelectronics Processing and Phenomena, 1983. **1**(3): p. 741-746.
189. Nobis, T. and M. Grundmann, *Low-order optical whispering-gallery modes in hexagonal nanocavities*. Physical Review A—Atomic, Molecular, and Optical Physics, 2005. **72**(6): p. 063806.
190. Grundmann, M., et al., *Electrical properties of ZnO thin films and optical properties of ZnO-based nanostructures*. Superlattices and Microstructures, 2005. **38**(4-6): p. 317-328.
191. Santori, C., et al., *Indistinguishable photons from a single-photon device*. nature, 2002. **419**(6907): p. 594-597.

192. Empedocles, S.A. and M.G. Bawendi, *Quantum-confined stark effect in single CdSe nanocrystallite quantum dots*. Science, 1997. **278**(5346): p. 2114-2117.
193. Bansal, B., *A model for the temperature dependence of photoluminescence from self-assembled quantum dots*. Journal of applied physics, 2006. **100**(9).
194. Le Ru, E., et al., *Strain-engineered InAs/GaAs quantum dots for long-wavelength emission*. Physical Review B, 2003. **67**(16): p. 165303.
195. Sanguinetti, S., et al., *Effective phonon bottleneck in the carrier thermalization of InAs/GaAs quantum dots*. Physical Review B—Condensed Matter and Materials Physics, 2008. **78**(8): p. 085313.
196. Halilov, S. and S. Mil'shtein, *Effective mass discontinuity and current oscillations in stratified systems*. Journal of Physics D: Applied Physics, 2015. **48**(46): p. 465102.
197. Brunner, K., et al., *Sharp-line photoluminescence and two-photon absorption of zero-dimensional biexcitons in a GaAs/AlGaAs structure*. Physical review letters, 1994. **73**(8): p. 1138.
198. Warming, T., et al., *Hole-hole and electron-hole exchange interactions in single InAs/GaAs quantum dots*. Physical Review B—Condensed Matter and Materials Physics, 2009. **79**(12): p. 125316.
199. Shah, J., *Ultrafast spectroscopy of semiconductors and semiconductor nanostructures*. Vol. 115. 2013: Springer Science & Business Media.
200. Lakowicz, J.R., *Principles of fluorescence spectroscopy*. 2006: Springer.
201. Dalgarno, P.A., et al., *Coulomb interactions in single charged self-assembled quantum dots: Radiative lifetime and recombination energy*. Physical Review B—Condensed Matter and Materials Physics, 2008. **77**(24): p. 245311.
202. Ohnesorge, B., et al., *Rapid carrier relaxation in self-assembled In_xGa_{1-x}As/GaAs quantum dots*. Physical Review B, 1996. **54**(16): p. 11532.
203. Yang, X., et al., *Multiple-defect management for efficient perovskite photovoltaics*. ACS Energy Letters, 2021. **6**(7): p. 2404-2412.
204. Hulik, R., et al., *Continuous plane detection in point-cloud data based on 3D Hough Transform*. Journal of visual communication and image representation, 2014. **25**(1): p. 86-97.
205. Davanco, M., et al., *Heterogeneous integration for on-chip quantum photonic circuits with single quantum dot devices*. Nature communications, 2017. **8**(1): p. 889.
206. Hennessy, K., et al., *Quantum nature of a strongly coupled single quantum dot-cavity system*. Nature, 2007. **445**(7130): p. 896-899.
207. Lu, C.-Y. and J.-W. Pan, *Quantum-dot single-photon sources for the quantum internet*. Nature Nanotechnology, 2021. **16**(12): p. 1294-1296.
208. Shields, A.J., *Semiconductor quantum light sources*. Nature photonics, 2007. **1**(4): p. 215-223.
209. Liu, Y., et al., *Efficient blue light-emitting diodes based on quantum-confined bromide perovskite nanostructures*. Nature Photonics, 2019. **13**(11): p. 760-764.
210. Heyn, C., *Critical coverage for strain-induced formation of InAs quantum dots*. Physical Review B, 2001. **64**(16): p. 165306.
211. Ledentsov, N., et al., *Reversibility of the island shape, volume and density in Stranski-Krastanow growth*. Semiconductor science and technology, 2001. **16**(6): p. 502.

212. Lodahl, P., S. Mahmoodian, and S. Stobbe, *Interfacing single photons and single quantum dots with photonic nanostructures*. Reviews of Modern Physics, 2015. **87**(2): p. 347-400.
213. Mano, T., et al., *Fabrication of InGaAs quantum dots on GaAs (0 0 1) by droplet epitaxy*. Journal of Crystal Growth, 2000. **209**(2-3): p. 504-508.
214. Liang, B.-L., et al., *Energy transfer within ultralow density twin InAs quantum dots grown by droplet epitaxy*. ACS nano, 2008. **2**(11): p. 2219-2224.
215. Tatebayashi, J., M. Nishioka, and Y. Arakawa, *Over 1.5 μm light emission from InAs quantum dots embedded in InGaAs strain-reducing layer grown by metalorganic chemical vapor deposition*. Applied Physics Letters, 2001. **78**(22): p. 3469-3471.
216. Jiang, L., et al., *In 0.6 Ga 0.4 As/GaAs quantum-dot infrared photodetector with operating temperature up to 260 K*. Applied physics letters, 2003. **82**(12): p. 1986-1988.
217. Sanguinetti, S., et al., *Effects of post-growth annealing on the optical properties of self-assembled GaAs/AlGaAs quantum dots*. Journal of crystal growth, 2002. **242**(3-4): p. 321-331.
218. Sanguinetti, S., et al., *Rapid thermal annealing effects on self-assembled quantum dot and quantum ring structures*. Journal of Applied Physics, 2008. **104**(11).
219. Eaglesham, D. and M. Cerullo, *Dislocation-free stranski-krastanow growth of Ge on Si (100)*. Physical review letters, 1990. **64**(16): p. 1943.
220. Mano, T., et al., *Self-assembly of concentric quantum double rings*. Nano letters, 2005. **5**(3): p. 425-428.
221. Kuruma, K., et al., *Controlling interactions between high-frequency phonons and single quantum systems using phononic crystals*. Nature Physics, 2024: p. 1-6.
222. Laferriere, P., et al., *Systematic study of the emission spectra of nanowire quantum dots*. Applied Physics Letters, 2021. **118**(16).
223. Koguchi, N., S. Takahashi, and T. Chikyow, *New MBE growth method for InSb quantum well boxes*. Journal of crystal growth, 1991. **111**(1-4): p. 688-692.
224. Lifshitz, I.M. and V.V. Slyozov, *The kinetics of precipitation from supersaturated solid solutions*. Journal of physics and chemistry of solids, 1961. **19**(1-2): p. 35-50.
225. Braun, P., et al., *Nanoscale patterning of metallic surfaces with laser patterned tools using a nanoimprinting approach*. Applied Surface Science, 2023. **613**: p. 155786.
226. Lu, Y., S. Theppakuttai, and S. Chen, *Marangoni effect in nanosphere-enhanced laser nanopatterning of silicon*. Applied Physics Letters, 2003. **82**(23): p. 4143-4145.
227. Pang, J.S., et al., *Tunable three-dimensional plasmonic arrays for large near-infrared fluorescence enhancement*. ACS Applied Materials & Interfaces, 2019. **11**(26): p. 23083-23092.
228. Daudin, B., et al., *Epitaxial growth of GaN, AlN and InN: 2D/3D transition and surfactant effects*. physica status solidi (a), 1999. **176**(1): p. 621-627.
229. Mano, T., et al., *New self-organized growth method for InGaAs quantum dots on GaAs (001) using droplet epitaxy*. Japanese journal of applied physics, 1999. **38**(9A): p. L1009.

230. Venables, J.A., *Atomic processes in crystal growth*. Surface Science, 1994. **299**: p. 798-817.
231. Wang, Y.-R., et al., *Direct patterning of periodic semiconductor nanostructures using single-pulse nanosecond laser interference*. Optics Express, 2020. **28**(22): p. 32529-32539.
232. Subrahmanyam, A., *Nucleation of Nano-Matter and Nano-Thermodynamics*, in *Cold Plasma in Nano-Matter Synthesis*. 2024, Springer. p. 303-328.
233. Tomasulo, S., et al., *Morphological characterization of GaAs islands grown on InGaAs by droplet epitaxy*. Journal of Crystal Growth, 2022. **595**: p. 126803.
234. Ledentsov, N., et al., *Ordered arrays of quantum dots: Formation, electronic spectra, relaxation phenomena, lasing*. Solid-State Electronics, 1996. **40**(1-8): p. 785-798.
235. Heger, J.E., et al., *Superlattice deformation in quantum dot films on flexible substrates via uniaxial strain*. Nanoscale horizons, 2023. **8**(3): p. 383-395.
236. Wang, Y.-R., et al., *In-Situ Pulsed Laser Interference Nanostructuring of Semiconductor Surfaces*. Journal of Laser Micro Nanoengineering, 2020. **15**(2): p. 139-142.
237. Le Ru, E., J. Fack, and R. Murray, *Temperature and excitation density dependence of the photoluminescence from annealed InAs/GaAs quantum dots*. Physical Review B, 2003. **67**(24): p. 245318.
238. Moison, J., et al., *Self-organized growth of regular nanometer-scale InAs dots on GaAs*. Applied Physics Letters, 1994. **64**(2): p. 196-198.
239. Zhang, J.L., et al., *Epitaxial growth of single layer blue phosphorus: a new phase of two-dimensional phosphorus*. Nano letters, 2016. **16**(8): p. 4903-4908.
240. Heyn, C., *Kinetic model of local droplet etching*. Physical Review B—Condensed Matter and Materials Physics, 2011. **83**(16): p. 165302.
241. Montalenti, F., et al., *Vertical and lateral ordering of Ge islands grown on Si (001): theory and experiments*. Journal of Physics: Condensed Matter, 2007. **19**(22): p. 225001.
242. Antolín, E., et al., *Reducing carrier escape in the InAs/GaAs quantum dot intermediate band solar cell*. Journal of Applied Physics, 2010. **108**(6).
243. Bayer, M., et al., *Coupling and entangling of quantum states in quantum dot molecules*. Science, 2001. **291**(5503): p. 451-453.
244. Englund, D., et al., *Controlling the Spontaneous Emission Rate of Single Quantum Dots in a Two-Dimensional Photonic Crystal*. Physical review letters, 2005. **95**(1): p. 013904.
245. Leonard, D., et al., *Direct formation of quantum-sized dots from uniform coherent islands of InGaAs on GaAs surfaces*. Applied Physics Letters, 1993. **63**(23): p. 3203-3205.
246. Schmidt, O.G., *Lateral alignment of epitaxial quantum dots*. 2007: Springer Science & Business Media.
247. Warburton, R.J., *Single spins in self-assembled quantum dots*. Nature materials, 2013. **12**(6): p. 483-493.
248. Heitz, R., et al., *Energy relaxation by multiphonon processes in InAs/GaAs quantum dots*. Physical Review B, 1997. **56**(16): p. 10435.

249. Sanguinetti, S., et al., *Carrier thermal escape and retrapping in self-assembled quantum dots*. Physical Review B, 1999. **60**(11): p. 8276.
250. Bayer, M., et al., *Fine structure of neutral and charged excitons in self-assembled In(Ga)As/(Al)GaAs quantum dots*. Physical Review B, 2002. **65**(19): p. 195315.
251. Kuhlmann, A.V., et al., *Charge noise and spin noise in a semiconductor quantum device*. Nature Physics, 2013. **9**(9): p. 570-575.
252. Tersoff, J. and F. LeGoues, *Competing relaxation mechanisms in strained layers*. Physical review letters, 1994. **72**(22): p. 3570.
253. Petroff, P. and S. DenBaars, *MBE and MOCVD growth and properties of self-assembling quantum dot arrays in III-V semiconductor structures*. Superlattices and microstructures, 1994. **15**(1): p. 15.
254. Bimberg, D., et al., *Formation of self-organized quantum dots at semiconductor surfaces*. Applied surface science, 1998. **130**: p. 713-718.
255. Gurioli, M., et al., *Droplet epitaxy of semiconductor nanostructures for quantum photonic devices*. Nature materials, 2019. **18**(8): p. 799-810.
256. Perret, N., et al., *Origin of the inhomogeneous broadening and alloy intermixing in InAs/GaAs self-assembled quantum dots*. Physical Review B, 2000. **62**(8): p. 5092.
257. Atkinson, P., et al., *Formation and ordering of epitaxial quantum dots*. Comptes Rendus Physique, 2008. **9**(8): p. 788-803.
258. Michler, P., et al., *Quantum correlation among photons from a single quantum dot at room temperature*. Nature, 2000. **406**(6799): p. 968-970.
259. Köhler, A., et al., *The axial channel of the proteasome core particle is gated by the Rpt2 ATPase and controls both substrate entry and product release*. Molecular cell, 2001. **7**(6): p. 1143-1152.
260. Sanguinetti, S., S. Bietti, and N. Koguchi, *Droplet epitaxy of nanostructures*, in *Molecular Beam Epitaxy*. 2018, Elsevier. p. 293-314.
261. Kajikawa, K., H.T.H. Takezoe, and A.F.A. Fukuda, *Noncentrosymmetric structure of merocyanine J-aggregate assembly studied by second-harmonic generation*. Japanese journal of applied physics, 1991. **30**(8B): p. L1525.
262. Reyes, K., et al., *Unified model of droplet epitaxy for compound semiconductor nanostructures: experiments and theory*. Physical Review B—Condensed Matter and Materials Physics, 2013. **87**(16): p. 165406.
263. Holewa, P., et al., *Droplet epitaxy symmetric InAs/InP quantum dots for quantum emission in the third telecom window: morphology, optical and electronic properties*. Nanophotonics, 2022. **11**(8): p. 1515-1526.
264. 박석인, *Growth and Characterization of Position Controlled Droplet Epitaxy Quantum Dots*. 2018, 서울대학교 대학원.
265. Tuktamyshev, A., *Droplet Epitaxy Quantum Dots on GaAs (111) A substrates for Quantum Information Applications*. 2021.
266. Lita, B., et al., *Interdiffusion and surface segregation in stacked self-assembled InAs/GaAs quantum dots*. Applied Physics Letters, 1999. **75**(18): p. 2797-2799.
267. Joyce, B.A. and D.D. Vvedensky, *Self-organized growth on GaAs surfaces*. Materials Science and Engineering: R: Reports, 2004. **46**(6): p. 127-176.
268. Somaschi, N., et al., *Near-optimal single-photon sources in the solid state*. Nature Photonics, 2016. **10**(5): p. 340-345.

269. Huber, D., et al., *Strain-tunable GaAs quantum dot: a nearly dephasing-free source of entangled photon pairs on demand*. Physical review letters, 2018. **121**(3): p. 033902.
270. van de Groep, J., et al., *Thermodynamic theory of the plasmoelectric effect*. Scientific reports, 2016. **6**(1): p. 23283.
271. Koenderink, A.F. *Antenna ideas at the nanoscale: Single quantum emitters at visible wavelengths controlled using plasmonics and metamaterials*. in *2013 7th European Conference on Antennas and Propagation (EuCAP)*. 2013. IEEE.
272. Ward, M.B., et al., *Telecom-wavelength single-photon sources based on single quantum dots*, in *Semiconductor Quantum Bits*. 2008, Pan Stanford Publishing. p. 389-421.
273. Wang, X.-D., et al., *Waveguide-coupled deterministic quantum light sources and post-growth engineering methods for integrated quantum photonics*. Chip, 2022. **1**(3): p. 100018.
274. Esmann, M., S.C. Wein, and C. Antón-Solanas, *Solid-State Single-Photon Sources: Recent Advances for Novel Quantum Materials*. Advanced Functional Materials, 2024. **34**(30): p. 2315936.
275. Shih, C.-W., *Quantum light sources based on semiconductor quantum dots and the collective effects*. 2024.
276. Baboux, F., G. Moody, and S. Ducci, *Nonlinear integrated quantum photonics with AlGaAs*. Optica, 2023. **10**(7): p. 917-931.
277. Huang, J., *Exciton-Polariton Complexes in Chip-Scale Cavity Quantum Electrodynamics: Localized Single-Site Arrays and Color Centers*. 2024: University of California, Los Angeles.
278. Hauff, N.V., *Topological Waveguides and Symmetrical Droplet Quantum Dots for Scalable Photonic Quantum Technology*. 2023.
279. Limame, I., *Development of scalable quantum nanophotonic devices based on InGaAs quantum dots*. 2024, Technische Universität Berlin.
280. Zhang, J. and Y. Kivshar, *Quantum metaphotonics: Recent advances and perspective*. APL Quantum, 2024. **1**(2).